Engineering nonlinearities in nanoscale optical systems: physics and applications in dispersion-engineered silicon nanophotonic wires

R. M. Osgood, Jr.,[1] N. C. Panoiu,[2] J. I. Dadap,[1] Xiaoping Liu,[1] Xiaogang Chen,[1] I-Wei Hsieh,[1] E. Dulkeith,[3,4] W. M. J. Green,[3] and Y. A. Vlasov[3]

[1]Microelectronics Sciences Laboratories, Columbia University, New York, New York 10027, USA

[2]Department of Electronic and Electrical Engineering, University College London, Torrington Place, London WC1E 7JE, UK

[3]IBM T. J. Watson Research Center, Yorktown Heights, New York 10598, USA

[4]Present address, Detecon, Inc., Strategy and Innovation Engineering Group, San Mateo, California 94402, USA

Received October 7, 2008; revised November 24, 2008; accepted November 25, 2008; posted November 25, 2008 (Doc. ID 102501); published January 30, 2009

The nonlinear optics of Si photonic wires is discussed. The distinctive features of these waveguides are that they have extremely large third-order susceptibility $\chi^{(3)}$ and dispersive properties. The strong dispersion and large third-order nonlinearity in Si photonic wires cause the linear and nonlinear optical physics in these guides to be intimately linked. By carefully choosing the waveguide dimensions, both linear and nonlinear optical properties of Si wires can be engineered. We review the fundamental optical physics and emerging applications for these Si wires. In many cases, the relatively low threshold powers for nonlinear optical effects in these wires make them potential candidates for functional on-chip nonlinear optical devices of just a few millimeters in length; conversely, the absence of nonlinear optical impairment is important for the use of Si wires in on-chip interconnects. In addition, the characteristic length scales of linear and nonlinear optical effects in Si wires are markedly different from those in commonly used optical guiding systems, such as optical fibers or photonic crystal fibers, and therefore guiding structures based on Si wires represent ideal optical media for investigating new and intriguing physical phenomena.

OCIS codes: 190.4390, 130.4310, 190.7110, 060.5060, 130.2790, 230.3990, 230.7370.

Engineering nonlinearities in nanoscale optical systems: physics and applications in dispersion-engineered silicon nanophotonic wires

R. M. Osgood, Jr., N. C. Panoiu, J. I. Dadap, Xiaoping Liu, Xiaogang Chen, I-Wei Hsieh, E. Dulkeith, W. M. J. Green, and Y. A. Vlasov

1. Introduction

1.1. Introductory Remarks

Nonlinear optics is one of the major successes of modern optics. Practical utilization of nonlinear optical processes and in most cases even the simple observation of the phenomena relies on high-intensity near-monochromatic light sources and control of phase and coherence in the optical system; both of these capabilities are now available thanks to laser sources. Nonlinear optics is also eminently practical, with hundreds of applications being pursued in the commercial arena, including wavelength converters for telecommunications, optical signal processing, and optical switching.

In the past decade, major advances in our ability to pattern and fabricate a variety of materials have led to the focusing of research in nonlinear optics on the topic of nanoscale nonlinear optic methods. However, despite its contemporary name, nanoscale nonlinear optics has a long and distinguished past! This is well illustrated by the early use of optical frequency mixing at the ångstrom-dimension tip of point contact diodes [1]. In fact this approach has recently been revived in the use of the surfaces of scanning tunneling microscope tips to enhance nonlinear optics for local generation of optical higher harmonics [2]. In addition the need to make integrated optical structures, which enable efficient phase matching by using artificial periodic media, is clearly a micrometer-scale precursor to today's nanoscale nonlinear optics. The best example of this approach is the progress in making periodic-domain poled $LiNbO_3$ (PPLN) structures [3]. In fact, these structures have recently been pushed to nanoscale dimensions by using two-dimensional poling methods [4].

More recently, research in nonlinear nano-optical phenomena has taken two very different directions. The first has used the excitement in metamaterials to develop a new, generally metal-film-based approach to driving strong nonlinearities in metals and metallodielectric materials [5–8]. Typically this metamaterials approach uses a surface normal configuration. These metallodielectric nanostructures can make nonlinear optical conversion at a smaller scale and broader band, with a lower optical loss. Metamaterials can also

give more flexibility in wavelength range via the choice of the dimensions of the nanostructure metal array and its selection of materials. This approach has been examined for important potential applications in optical signal processing; however the focus has generally been on investigating new optical physics. The second direction has examined in-plane optical nonlinearities in dielectric structures with nanometer-scale cross sections. In this case, the usual guided-wave nonlinearities are generated in a structure, which also controls to all orders the optical dispersion of the guiding structure. The nonlinearities are sufficiently large that the waveguides act in the same manner as they do in optical fibers—but since the structures are of chip scale, their subwavelength characteristics strongly affect their optical properties. Consequently, both new physical and new optical phenomena are present, and nearer-term applications are apparent. These high-confinement Si devices are a natural complement to fiber optic guided-wave interconnect systems.

This second nano-optical approach, which is the subject of this review, is based on the recent advances in developing the area of active Si photonics devices and understanding their underlying physics. This area of research began more than two decades ago by using clearly nonnanoscale devices based on the ideas of Soref and Lorenzo, in which the first Si waveguide was demonstrated [9]. Soon after, work in active Si photonics focused on realizing electro-optical modulators, through the use of free carriers, e.g., by carrier injection, [10–14], and thermo-optic modulators, by using the favorable thermo-optic coefficient of Si [15–19]. An important goal for these modulators, as well as for other Si optical passive and active devices, is scaling down the device footprint and power consumption and increasing the frequency response so as to allow for full integration with Si electronics. In fact, because of the favorable electronic, optical, and physical properties of Si and the mature complementary metal-oxide-semiconductor (CMOS) fabrication processing technology, large-scale integration of functional optical devices has become possible, including integration with relatively complex electronic components. The use of CMOS manufacturing [20] also facilitates its precise patterning to be applied to integrated optical circuits; this enables, for example, greatly reduced sidewall roughness and, hence, very low loss even in the small waveguides mentioned here. The rapid growth of Si photonics has already generated several excellent review articles and books [21–39].

This work in active devices has led to increasing interest in nonlinear Si photonics. Generally speaking this interest stems from two separate but related research goals: the development of all-optical control of dramatically scaled-down optical devices and the interest in small-dimension waveguides as on-chip transport light guides. In the latter case, one of course primarily wishes to minimize nonlinear effects, although they could have an important functionality in applications such as light amplification or on-chip optical sources. Again, progress in this area of Si photonics has been rapid. For example, soon after observation of spontaneous Raman emission in Si waveguides, [40,41], Raman amplification in Si waveguides was first demonstrated by Claps *et al.* in 2003 [42] and later by other groups [43–50]. Raman lasing was then demonstrated in Si waveguides [51–55], SiGe waveguides [48], Si rings [56], and in hybrid AlGaInAs–Si waveguides [57]. In addition, other nonlinear optical effects or functionalities such as wavelength conversion via coherent anti-Stokes Raman scattering (CARS) [58,59] and four-wave mixing (FWM), [60,62–66], self-phase modulation (SPM) [67–73], cross-phase modulation

(XPM) and cross-absorption modulation [74–77], switching via two-photon absorption (TPA) [78,79], and supercontinuum generation [80] have been demonstrated experimentally or studied theoretically. These effects can lead to important functionalities such as pulse shaping or optical switching. From the point of view of optical transport, these effects can introduce impairments to a Si-based optical data system via such effects as SPM-induced spectral broadening or interchannel cross talk due to XPM.

The linear and nonlinear optical properties of crystalline Si make it an ideal medium for nanoscale integrated photonic devices. First, Si's large refractive index ($n \sim 3.5$), in conjunction with a low-index cladding ($n_{\text{cladding}} \sim 1$ for air or $n_{\text{cladding}} \sim 1.45$ for silica), results in very tight light confinement. Such strong light confinement lets Si guided-wave devices be scaled down to ultrasmall cross sections, i.e., $<0.1\ \mu\text{m}^2$. These devices are termed Si photonic wires (SPWs). This reduction to nanoscale cross section, which is possible in a medium with high refractive index contrast, leads to three distinct advantages: the capability for dispersion engineering, a high optical field density, and an intrinsically short carrier lifetime due to rapid diffusion into surface states. A second optical property of Si affects its use for nonlinear optics. In particular, while Si does not have a second-order nonlinearity, it does have an extremely large third-order nonlinear optical susceptibility in the near infrared—about 3–4 orders of magnitude larger than that of silica [81]. This large cubic nonlinearity in Si, in connection with its strong optical confinement, leads to further enhancement of the effective optical nonlinearity. This enhancement results in a low optical power requirement or threshold for achieving strong nonlinear optical effects, as well as in very short nonlinear optical devices, of the order of a few hundred micrometers to millimeters in length.

Let us return to the issue of dispersion in SPWs. Because of their nanoscale cross sections, their dispersion properties become markedly different from those of standard optical fibers, photonic crystal fibers (PCFs), or even of Si waveguides with micrometer cross-sectional dimensions. In particular, because of their ultrasmall dimensions, their dispersion is controlled by the exact geometry of their cross-sectional area. This property leads to the possibility of tailoring of their basic dispersion characteristics such as the group-velocity dispersion (GVD). Note that this same concept has been discussed extensively in conjunction with high-index-contrast fibers; in that case dimensional changes in dispersion are not as pronounced as in the case of SPWs, but their longer propagation length makes them important nonetheless. In general, this capability of engineering the optical dispersion in SPWs is important for tailoring the phase index, as it enables control of phase matching of nonlinear optical processes such as FWM, broadband optical parametric gain, modulation instability (MI), and CARS. It also affects more pulse dynamics, including soliton generation and their dynamics, pulse compression and reshaping, etc. In addition, because of the large dispersion and effective optical nonlinearity of Si, it is possible to scale down the length $\times$ power product for integrated nonlinear devices more than in glass materials. In fact, at low to moderate laser pump powers of a few $\sim$100 s mW, the nonlinear lengths in Si wires are just a few millimeters.

1.2. Scope of This Review

Our review is organized as follows: first, the optical properties of SPWs are reviewed in Section 2, including methods for dispersion engineering of these tightly confined waveguides and their limitations. In Section 3, a discussion of the basic nonlinear optical response of Si is presented. This section will include a discussion of the basic phenomena and the various relevant nonlinear optical parameters for Si and Si-wire waveguides. In Section 4, a complete theoretical framework for modeling nonlinear pulse propagation in Si wires and the current state of knowledge of the nonlinear optical properties of these light guiding devices are introduced. Our model uses a fully rigorous approach based on a system of nonlinearly coupled equations describing the pump and probe field envelopes. It also incorporates the effects of optically generated free carriers and the effects of crystalline anisotropy of the optical nonlinearity. In Section 5, nonlinear optical phenomena, such as stimulated Raman scattering (SRS) and two-photon absorption (TPA), are discussed. In Section 6, the relevant nonlinear optical effects that transiently change the effective index of the guiding Si structure (waveguide), and hence the phase of light, are reviewed; in addition, this section will also discuss basic parametric processes in these waveguides, such as SPM, XPM, FWM, and MI. The effects of waveguide dispersion for each of these nonlinear optical processes will also be discussed. In the case of ultrashort laser pulses, i.e., of duration ~200 fs or less, the physics are such that the nonlinear and various dispersion lengths are all comparable; such a system yields complex, but rich information on pulse propagation and pulse distortion in Si wires and opens new avenues for research in future applications.

Finally, our review will conclude with a discussion of the emerging applications of nonlinear optics in Si wires in Section 7. Because in many cases that are relevant for important practical applications the characteristic lengths of linear and nonlinear optical effects are less than or comparable with the waveguide length, phenomena that are important in optical fibers are possible in a downscaled integrated form. In effect, these observations show clearly that SPWs have the potential to form a fiber-on-a-chip system, allowing for nonlinear optical control of on-chip functions or integrated photonic circuits. They are also important devices for on-chip optical data buses for ultrahigh-bit-rate data transport.

2. Si Photonic Wires: Optical Characterization and Dispersive Properties

In this section we discuss the main linear optical properties of SPWs, with a particular emphasis on the interrelations between the transverse size of the device and the main physical quantities that determine their guiding properties, namely, the waveguide modes and the corresponding propagation constant. In our discussion, we will focus on a property that is particularly important for subwavelength guiding devices, namely, the **frequency dispersion** of these quantities.

2.1. Si Photonic Wires and Their Optical Characterization

SPWs are typically patterned on Unibond Si-on-insulator (SOI) with a 1 μm thick oxide layer and with the wire aligned along the $[1\bar{1}0]$ crystallographic direction. Si wires make use of the superior vertical dimension control and thick optical-decoupling oxide that is possible with Unibond material. A convenient cleavage plane of Si for formation of high-quality end facets typically determines the choice of this crystal direction. Initial comparison of the optical loss in SOI technologies involved an investigation with several of the emerging SOI wafer types. As a result, Unibond material was shown to be a useful basis for extremely compact single-mode SOI-based devices [82]. Subsequent research showed that optical losses in Si wires could be made sufficiently low that chip-scale lengths were feasible. These low-loss Si-wires are described in detail in [83,84]. For our work described in this review, all waveguides were fabricated by using the CMOS fabrication line at the IBM T. J. Watson Research Center. For these and other waveguides of many of the groups referred to here, each end of a wire uses index tapering to couple the much larger optical fiber mode to that of the waveguide. The use of inverse taper coupling techniques have been developed, including polymer-clad [85] and oxide-clad mode converters [86], which allow particularly efficient incoupling and outcoupling (see Fig. 1). Single-mode SPWs typically have dimensions of ~200 to 300 nm in height and 400 to 500 nm in width. The waveguides are generally cut off for the lowest-order TM mode, although quasi-single-mode guides, that is, slightly multimode guides, are sometimes used to reduce loss and dispersion sensitivity. These wires can be fabricated to be as long as many centimeters, with the longest guides using very tight radius bends for compact folding. The measured intrinsic waveguide losses are typically $\alpha_{in} \approx 3.0$ dB/cm for TE polarization near $\lambda = 1550$ nm; however, lower losses of 1.7 dB/cm have been measured [87]. The issue of loss in such high-index-contrast waveguides has been examined by using an analytic coupled-mode theory along with numerical finite-difference time-domain

Figure 1

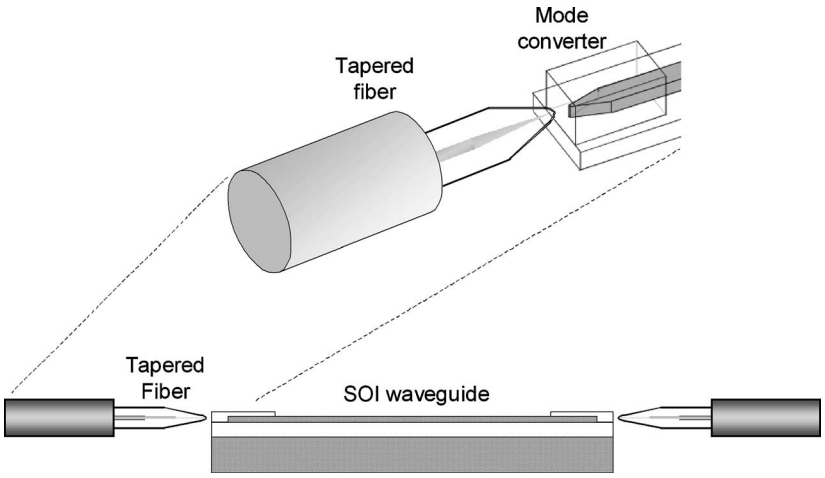

Typical experimental setup. In nonlinear optical experiments, input tapered fiber is often replaced by a microscope objective to mitigate SPM in the fiber because of the high intensity of the ultrashort pulses used.

calculations; the loss in these waveguides is entirely attributable to residual roughness on the waveguide walls, as long as the oxide substrate layer is sufficient to prevent coupling to the underlying Si wafer [88]. These calculations yield loss as a function of the correlation length of the roughness as well as its amplitude.

2.2. Dispersion Engineering in Si Photonic Wires

2.2a. Introduction

Control of dispersion in guided-wave optics is important in order to implement more efficient functions such as wavelength conversion or modulation and to control the temporal properties of short pulses as they propagate within the waveguide. Engineering of dispersion had been demonstrated earlier in PCFs [89], submicrometer waveguides [90], and multimode fibers [91]. Because of their submicrometer cross sections and high index contrast and, hence, strong optical confinement, waveguide dispersion in SPWs can be much larger than in fibers. This strong dispersion makes it possible to manipulate optical pulse properties within the scale length of a Si chip. It also means that during waveguide or waveguide device design great care needs to be taken when designing the dispersion characteristics of these Si wires so as to achieve the required behavior of optical pulses propagating in these waveguides. Calculations of the dimensional variation in dispersion in submicrometer buried Si wires, in a SiO_2 cladding, were first demonstrated by Chen *et al.* [92]. This possibility of dispersion engineering was shown for several possible wire cross-sectional dimensions, including one that exhibited zero GVD (ZGVD) at telecommunications wavelengths [92]. Subsequent measurements and calculations by Dulkeith *et al.* [93] and Turner *et al.* [94] showed clearly that such structures could be fabricated and their dispersion measured. For example, the work by Turner *et al.* demonstrated that the GVD parameter D in such waveguides could be tuned from -2000 to 1000 ps/(nm km). Later, Yin *et al.* [95] calculated the dispersive properties of larger-dimension rib waveguides by using the effective-index method approximation. Chen *et al.* also investigated the effect of third-order dispersion (TOD) in waveguides with various dimensions and its effects on pulse propagation [96]. More recently an investigation of the utility of conformal thin overlayers of Si_3N_4, with or without SiO_2, to flatten or reduce dispersion in SPWs was carried out [97,98].

2.2b. Dispersion in Si Nanophotonic Wires

The strong optical confinement in ultrasmall Si-wire waveguides causes the waveguide geometry to dominate their dispersive properties. This property can be shown clearly by comparison of the calculated dispersion coefficients of several dispersive orders for several single-mode waveguides of different dimensions. To do this, consider the strip waveguide structure shown in Fig. 2 with the optical propagation along the $[1\bar{1}0]$ direction of the single-crystal-Si layer on an SOI wafer. This comparison will consider the following waveguide dispersion orders for this structure: the effective index, n_{eff}, defined by $\beta = n_{\text{eff}}\omega/c$, where β is the mode propagation constant, the group index n_g is defined as $n_g = c/v_g = \beta_1 c$, where v_g is the group velocity of the mode, the GVD coefficient is β_2, and the TOD coefficient is β_3. The dispersion coefficient of the nth order is defined as $\beta_n = d^n\beta/d\omega^n$. Also note the relation of the frequently used GVD parameter D to β_2, i.e., $D = -2\pi c\beta_2/\lambda^2$. Such

Figure 2

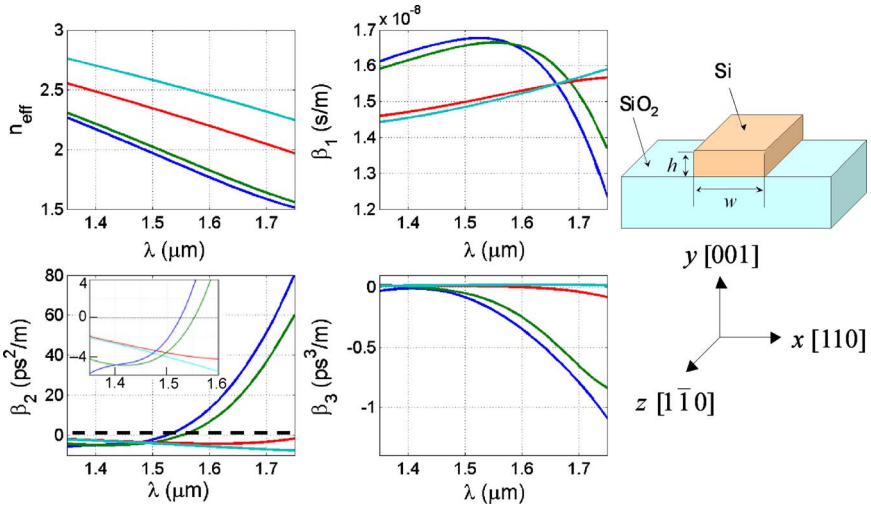

Plots of computed effective index of refraction, and first-order dispersion through TOD as a function of wavelength for four different Si-wire dimensions. Blue, 220 nm × 350 nm; green, 220 nm × 360 nm; red, 220 nm × 450 nm; light blue, 330 nm × 450 nm. Inset, expanded view of the second-order dispersion indicating the ZGVD line. Also shown is the waveguide geometry.

calculations use either the finite-element method or vectorial beam propagation method computations of the same quantities. Note that the material frequency dispersion of bulk Si is incorporated into the numerical calculations via the Sellmeier relation [99]

$$n(\lambda) = \varepsilon + \frac{A}{\lambda^2} + \frac{B\lambda_1^2}{\lambda^2 - \lambda_1^2}. \tag{1}$$

For Si, the material constants in Eq. (1) are $\lambda_1 = 1.1071\ \mu$m, $\varepsilon = 11.6858$, $A = 0.939816\ \mu\text{m}^2$, and $B = 8.10461 \times 10^{-3}$ (in what follows, unless otherwise specified, n refers to the index of refraction of Si). The results of these numerical calculations have been compared with and found to agree with experimental data [93]. Two examples illustrate the values of dispersion in these waveguides that have been both measured and calculated. In the first, for a 226 nm × 525 nm waveguide at 1550 nm the dispersion is found to be 4400 ps/(nm km), a value that is 3 orders of magnitude greater than that in standard optical fiber. The TOD of this same waveguide is found to be 0 ± 50 ps/(nm^2 km). Both values agree well with the values calculated by using finite-element methods [93]. Finally, in some cases, even higher orders of dispersion can be important! An excellent example of this point is the importance of fourth-order dispersion for nonlinear frequency mixing when operating at wavelengths near the ZGVD point of a waveguide [100]; this example is discussed below in Subsection 2.2c and subsequently in Section 7.

One of the more important goals of dispersion engineering is to minimize pulse broadening via the design of waveguides to be at the ZGVD point for a given operational wavelength. While there are limitations to the application of this technique, e.g., the presence of higher-order dispersion or inaccuracy in

patterning, it is important to minimize pulse broadening for applications involving pulse propagation in waveguide interconnects. Consider, as a generic example, the case of a Si channel waveguide surrounded by SiO_2. Figure 3 shows a contour map illustrating the ZGVD wavelength for different waveguide dimensions [37]. This ZGVD contour map is created by first calculating the dispersion coefficients of SPWs for a series of waveguide dimensions. The waveguide height h ranges from 225 to 400 nm, and the width w ranges from 375 to 800 nm, in increments of 25 nm for both dimensions. For smaller waveguide dimensions, two ZGVD wavelengths are possible. Here we present only the lower value of the two wavelengths of the ZGVD. The SPW ZGVD wavelength data reported by Turner *et al.* [94] are in general agreement with the results of our calculations. As is apparent from data such as in Fig. 3, single-mode SPW waveguides with zero dispersion can be realized in the relevant telecommunications wavelength range. In addition, this ZGVD data also provides a sense of the relative fabrication tolerances. For example, we see from Fig. 3 that for small h and large w the required fabrication tolerances would be much tighter because of the higher rate of change of the ZGVD wavelengths per unit waveguide length. Finally, the use of an almost square-shaped cross section allows the ZGVD points to be matched for the TE and TM modes in a two-mode waveguide [66].

Earlier in this review the measurement of dispersion in SPWs was alluded to. Because of the different geometry from optical fibers and the large values of dispersion in SPWs, different approaches have been adopted to measure this optical dispersion. These schemes have included Mach–Zehnder interferometric methods, modulation phase shift methods [98], and frequency mixing using high-frequency spectrum analyzers. In addition, in the case of femtosecond phenomena the role of TOD coefficient β_3 may be essential in determining the waveguide's optical properties. There are several, physics-based, approaches to determining this quantity. For example, β_3 can be determined by fitting the experimental data on the spectral output from a waveguide to numerically generated spectra, using simulations that incorporate β_3 [73]. Thus in this case simulations are done using values of β_3 in the vicinity of the estimated

Figure 3

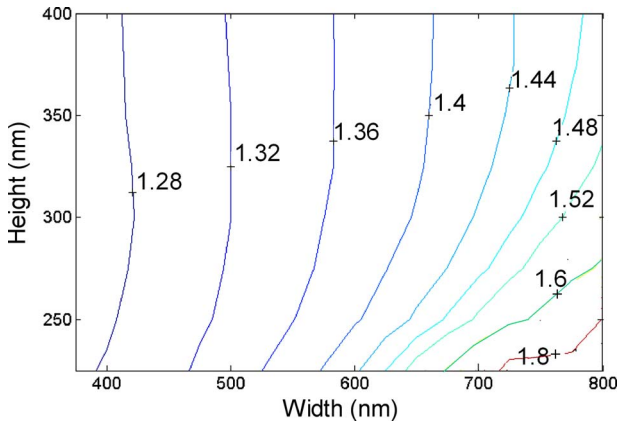

ZGVD map for SPW channel waveguides. The ZGVD wavelengths are expressed in units of micrometers.

value until the various features of the spectrum, such as the peaks and dips, are reproduced. This fitting method has been used to determine the TOD for Si wires.

2.2c. Dispersion Control for Nonlinear Waveguide Optics

The large third-order nonlinear optical susceptibility $\chi^{(3)}$ of Si makes it possible to consider a variety of chip-based nonlinear optical applications that rely on the extended interaction of optical waves at multiple wavelengths and at significant powers. The latter requirement demands that the nanophotonic wires exhibit a small but finite anomalous GVD, that is, having a GVD parameter $D > 0$ ps/(nm km) [101]. Anomalous dispersion can be achieved in SPW waveguides as a result of the strong optical confinement; for example, as we have just discussed, a large net anomalous GVD, i.e., $D \sim 4000$ ps/(nm km), occurs for air-clad wires with a cross section of 226 nm $\times$ 525 nm [93]. However, this same large GVD ($\sim$200$\times$ larger than that of single-mode fiber, SMF) can reduce the overall bandwidth of parametric processes such as FWM, since the spectral bandwidth over which efficient nonlinear optical interaction can be maintained depends on phase matching the total phase of the input, pump, and converted waves such that $\Delta k_{\text{total}} = 0$. In practice, this means that it is best to operate near the ZGVD point of the waveguide, so as to cause the nonlinearly induced change in the wave vectors of the interacting beams to cancel the residual linear phase mismatch. In addition, it is also important to reduce the wavelength dependence of the GVD so as to have similar nonlinearly induced phase changes at each wavelength.

There are several approaches to ameliorating a large, wavelength-dependent GVD. For example, as described above, a near-zero, but still anomalous, GVD can be engineered most simply via control of the geometrical dispersion through the dimensions and/or aspect ratio of the Si waveguide core [92–95]. However this approach also can increase the waveguide cross-sectional area and result in a reduction in the effective waveguide nonlinearity (see the definition below in Subsection 4.2). An alternative approach to engineering SPW wire dispersion, which flattens GVD and better retains the SPW effective nonlinearity, is to use a thin conformal layer of silicon nitride (Si_3N_4) overlayers and/or oxide [97]. This approach is conceptually similar to that used in the design of dispersion-shifted fiber [102,103]; in the case of fiber, the thickness and refractive index of thin cladding layers surrounding its core are adjusted to control the balance of geometrical and material dispersion, producing the desired net dispersion characteristics.

Accurate numerical experiments have been done using computations based on the finite-element method to determine the efficacy of this conformal thin-film method for dispersion control [97]. The geometry of this approach is shown in the inset of Fig. 4 (left-hand panel), i.e., a Si core of height h and width w etched in a buried-oxide (BOX) layer. The Si core is covered with a conformal Si_3N_4 overlayer of thickness t and then capped with a thick oxide layer. Figure 4 (left-hand panel) plots the calculated GVD versus wavelength for a 220 nm $\times$ 450 nm wire, for several Si_3N_4 overlayer thicknesses. With oxide cladding only ($t = 0$ nm, no Si_3N_4 coating), the GVD at $\lambda = 1.55$ μm has a value of 532 ps/(nm km). However, using a conformal Si_3N_4 overlayer of 60 nm significantly reduces this dispersion to 38 ps/(nm km), a value sufficiently low to achieve efficient phase-matched wavelength conversion or FWM parametric gain at low pump powers [64,66,100]. In addition, the use of thin

Figure 4

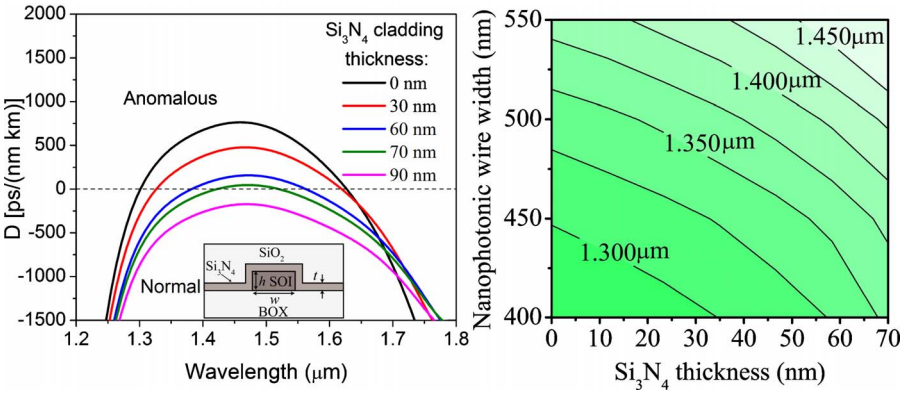

Left, plot of GVD, D, versus different Si_3N_4 overlayer thicknesses, for the fundamental TE-like mode of a Si nanophotonic wire with dimensions h=220 nm, w=450 nm, for different Si_3N_4 overlayer thicknesses. Inset, cross-section geometry. Right, ZGVD wavelength contours for lowest quasi-TE mode versus Si_3N_4 layer thickness, for several wire widths. Waveguide height is 220 nm. From [97].

overlayers also reduces fourth-order dispersion, producing wide spectral regions with small GVD curvature and facilitating broadband phase matching [66,100].

By altering the Si_3N_4 overlayer thickness, the ZGVD points can be shifted in wavelength. Figure 4 (right-hand panel) illustrates this behavior with a contour plot of the short-wavelength ZGVD point versus the wire width and Si_3N_4 thickness, for a wire height of h=220 nm. The ZGVD point shifts to longer wavelengths as the width becomes larger and/or the Si_3N_4 overlayer becomes thicker, indicating that these two parameters may be used as independent degrees of freedom in tailoring the spectral dispersion of a Si nanophotonic wire waveguide. Engineering the phase matching over a broadband wavelength range makes this approach useful for designing highly compact, broadband Si nonlinear devices. The most important aspect of using the conformal overlayer method for dispersion management is that it does not reduce the effective nonlinearity of the wire waveguide to the extent done by a simple expansion of the waveguide dimension [97].

As a final consideration in this subsection, higher-order dispersion can be important in several nonlinear optical phenomena. For example, the case of SPW TOD can lead to asymmetries in the sidelobes of the pulse; this case is discussed in Subsection 6.2. In another example, when operating near the ZGVD point, fourth-order dispersion in fact limits the bandwidth of the FWM processes and must therefore be carefully controlled, as is discussed in Subsection 6.5. As mentioned above, certain approaches such as the conformal thin films reduce these higher-order dispersion coefficients as well as the GVD. Furthermore, for accurate modeling of ultrashort optical pulses, which is important for applications that rely on the propagation or generation of ultrabroadband pulses, such as supercontinuum generation or ultrabroadband optical sources, one customarily requires using values of the dispersion coefficients beyond the tenth order [101,104,105]. In the case of SPWs,

retrieving this information from the numerically computed frequency dependence of the propagation constant, $\beta=\beta(\omega)$, can lead to large errors, and therefore in this case it is important to employ theoretical and experimental tools that would allow us to understand and control the interplay between the **global** characteristics of the waveguide dispersion and pulse dynamics.

2.2d. Active Control of Birefringence

Active control of phase mismatch in Si waveguides has been demonstrated [106]. Such an active-dispersion-control capability could be used, for example, to correct fabrication errors in the designed dispersion or changes in dispersion due to variations in the environmental conditions. In the method of [106], a thin-film piezoelectric transducer integrated on the waveguides was shown to allow adjustment of Si-waveguide dispersion. Specifically, the birefringence induced by the piezoelectric transducer was demonstrated to allow active control of phase matching for nonlinear optical mixing (specifically CARS). This device alters the dispersion for cross-polarized beams by varying the stress in the waveguide and can thus be useful for trimming its wavelength-dependent GVD values.

In the device, a bare SOI rib waveguide was first clad with oxide, to act as an optical decoupling layer, and then an overlayer of thin-film zirconate titanate was added to act as a piezoelectric capacitor. This piezoelectric transducer (PZT) consisted of a thin-film PZT layer with top and bottom platinum/titanium (Pt/Ti) electrodes. Stress generated in the structure changed the waveguide dispersion. In addition to an improvement in the efficiency that was due simply to the residual stresses of the cladding layers, an additional tunable stress was applied by biasing the PZT, which realized a further 5–6 dB enhancement of the efficiency. This tunable phase-match transducer was not enough to bring the waveguide to the zero phase-mismatch condition; however, it was sufficient to compensate for fabrication-induced error in waveguide dimensions.

3. Basic Parameters of Nonlinear Optics in Crystalline Si

Much of the impetus for considering nonlinear optical phenomena in SPWs is the tight optical confinement in these submicrometer waveguides. Because of the high index contrast and ultrasmall cross section of the waveguide, the intensity of the optical field, which is proportional to $|\mathbf{E}(\mathbf{r},t)|^2$, is, for example, orders of magnitude higher than that inside the core of the SMF, for a similar value of the optical power P. In addition, as will be discussed below, the nonlinear response of crystalline Si is extremely strong. As a result, even for an optical signal with a peak power in the range of a few tens of milliwatts, the nonlinear optical effects can be significant.

3.1. Basic Nonlinear Optical Physics in Si

To examine the nonlinear response of crystalline Si, consider the constitutive relation leading to the electric polarization $\mathbf{P}(\mathbf{r},t)$ of the medium. Using a power series for the electric field,

$$\mathbf{P} = \mathbf{D} - \varepsilon_0 \mathbf{E} = \varepsilon_0(\boldsymbol{\chi}^{(1)} \cdot \mathbf{E} + \boldsymbol{\chi}^{(2)}{:}\mathbf{EE} + \boldsymbol{\chi}^{(3)} \vdots \mathbf{EEE} + \cdots), \tag{2}$$

where $\mathbf{D}$ is the electric displacement field and $\boldsymbol{\chi}^{(i)}$ is the ith-order optical susceptibility, which is generally a $(i+1)$th-rank tensor. Susceptibilities depend on the crystal structure of the medium, and for isotopic or amorphous material, such as in a silica optical fiber, the susceptibilities are characterized by scalar quantities. In crystalline Si, whose optical nonlinearity is anisotropic, the tensor nature of the nonlinear susceptibilities has to be taken into account. Further, the polarization can be categorized into linear and nonlinear parts, $\mathbf{P}=\mathbf{P}_{\mathrm{L}}+\mathbf{P}_{\mathrm{NL}}$, according to its power dependence on the incident electric field, where

$$\mathbf{P}_{\mathrm{L}} = \varepsilon_0 \boldsymbol{\chi}^{(1)} \cdot \mathbf{E},$$

$$\mathbf{P}_{\mathrm{NL}} = \varepsilon_0 \boldsymbol{\chi}^{(2)}{:}\mathbf{EE} + \varepsilon_0 \boldsymbol{\chi}^{(3)} \vdots \mathbf{EEE} + \cdots. \tag{3}$$

Because the Si-crystal lattice is invariant to an inversion symmetry transformation, as it belongs to the point group symmetry $m3m$, the second-order susceptibility vanishes identically within the dipole approximation; that is, $\boldsymbol{\chi}^{(2)} \equiv 0$. The lowest-order optical nonlinearity in Si is then the third-order nonlinear response, which gives $\mathbf{P}_{\mathrm{NL}} \approx \varepsilon_0 \boldsymbol{\chi}^{(3)} \vdots \mathbf{EEE}$. Figure 5 summarizes a set of various third-order nonlinear optical phenomena that have been demonstrated in Si photonics.

To simplify the discussion, consider first only the electronic contribution to the nonlinear polarization; this contribution has two components, namely the Kerr and the TPA effects as shown in Fig 5(d). The Kerr effect is the result of the nonlinear electronic polarizability of Si, which has a response time of approximately tens of femtoseconds and, therefore, is effectively an instantaneous response. This same instantaneous response is characteristic of TPA as well, since it involves virtual intermediate levels. The real part of $\boldsymbol{\chi}^{(3)}$ is directly related to the nonlinear refractive index, n_2, whereas the imaginary part governs the TPA, which is quantified by the TPA coefficient β_{TPA}.

Under these circumstances, for a harmonic electric field,

$$\mathbf{E}(\mathbf{r},t) = \frac{1}{2}\mathbf{E}(\mathbf{r},\omega)e^{-i\omega t} + \text{c.c.}, \tag{4}$$

where c.c. stands for complex conjugation, the electronic nonlinear polarization at frequency ω, $\mathbf{P}_{\mathrm{NL}}(\mathbf{r},\omega)$, can be written as

$$\mathbf{P}_{\mathrm{NL}}(\mathbf{r},\omega) = \frac{3}{4}\varepsilon_0 \boldsymbol{\chi}^{(3)}(\omega;\omega,-\omega,\omega) \vdots \mathbf{E}(\mathbf{r},\omega)\mathbf{E}^{*}(\mathbf{r},\omega)\mathbf{E}(\mathbf{r},\omega), \tag{5}$$

where $\boldsymbol{\chi}^{(3)}(\omega;\omega,-\omega,\omega)$ is the electronic third-order susceptibility tensor of Si. Here we assume that sum-frequency generation processes are not phase matched, and therefore their contribution to the polarization, Eq. (5), can be neglected. The real part of this nonlinear susceptibility describes parametric processes, such as SPM, that lead to a change in the refractive index. The imaginary part corresponds to loss or gain processes, such as TPA. Because Si belongs to the crystallographic point group $m3m$ the susceptibility tensor $\boldsymbol{\chi}^{(3)}$ has 21 nonzero elements, of which only 4 are independent, namely, $\chi^{(3)}_{1111}$,

Figure 5

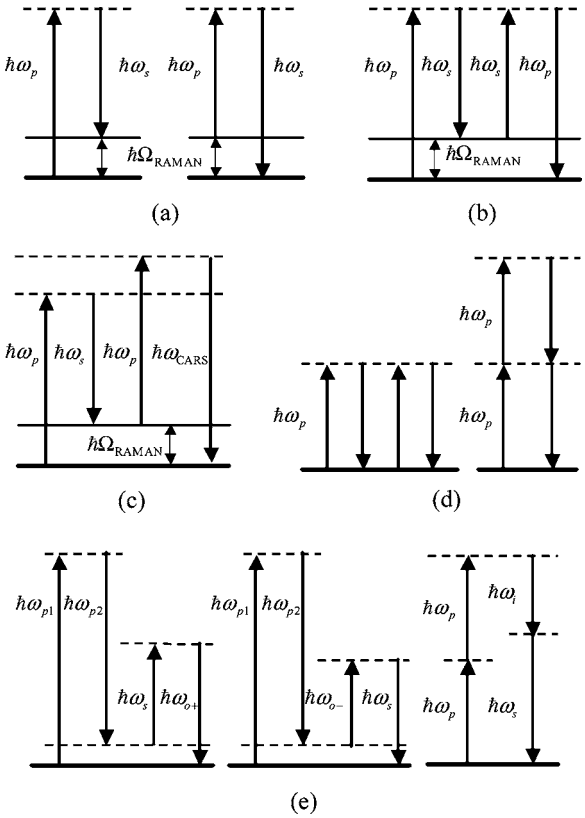

Relevant nonlinear optical processes in Si photonics: (a) spontaneous Raman (Stokes and anti-Stokes) emission, (b) stimulated Raman emission, (c) CARS, (d) Kerr effect and TPA, and (e) FWM.

$\chi^{(3)}_{1122}$, $\chi^{(3)}_{1212}$, and $\chi^{(3)}_{1221}$ [81]. Moreover, symmetry considerations lead to an additional relation, $\chi^{(3)}_{1122}=\chi^{(3)}_{1221}$. In addition, although the electronic nonlinear susceptibility shows frequency dispersion (see Subsection 4.4) in the frequency range considered here, since the corresponding photon energies $\hbar\omega$ in typical experiments are smaller than the bandgap energy E_g of Si, this nonlinear frequency dispersion is rather small. Consequently, we assume that the Kleinman symmetry relations are obeyed, which imply that $\chi^{(3)}_{1122}=\chi^{(3)}_{1212}$. Therefore, the remaining independent components of the susceptibility tensor are $\chi^{(3)}_{1111}$ and $\chi^{(3)}_{1122}$. It is important that recent experiments have demonstrated that across a broad range of wavelengths, between 1.2 and 2.4 μm, the ratio of these two components is constant, that is, $\chi^{(3)}_{1111}\approx 2.36\chi^{(3)}_{1122}$ [107]. Finally, while in much of this paper it is reasonable to assume that $\boldsymbol{\chi}^{(3)}$ is frequency independent, the possibility of its dispersion in waveguides is discussed in detail in Subsection 4.4.

Whereas it might be difficult to measure the nonlinear susceptibility $\boldsymbol{\chi}^{(3)}$ directly, its value can be easily derived from the Kerr coefficient n_2 and the TPA coefficient β_{TPA}; these quantities are related through the equation

$$\frac{\omega}{c}n_2 + \frac{i}{2}\beta_{\mathrm{TPA}} = \frac{3\omega}{4\varepsilon_0 c^2 n^2}\chi^{(3)}_{\mathrm{eff}}, \tag{6}$$

where for Si's symmetry group, the effective susceptibility $\chi^{(3)}_{\mathrm{eff}}$ is defined by

$$\chi^{(3)}_{\mathrm{eff}} = \chi^{(3)}_{1122}[(\hat{\mathbf{a}}^* \cdot \hat{\mathbf{b}})(\hat{\mathbf{c}} \cdot \hat{\mathbf{d}}) + (\hat{\mathbf{a}}^* \cdot \hat{\mathbf{c}})(\hat{\mathbf{b}} \cdot \hat{\mathbf{d}}) + (\hat{\mathbf{a}}^* \cdot \hat{\mathbf{d}})(\hat{\mathbf{b}} \cdot \hat{\mathbf{c}})]$$
$$+ (\chi^{(3)}_{1111} - 3\chi^{(3)}_{1122})\sum_{i=1}^{3} \hat{\mathbf{a}}_i^* \hat{\mathbf{b}}_i \hat{\mathbf{c}}_i \hat{\mathbf{d}}_i. \tag{7}$$

Here $\hat{\mathbf{a}}$ is a unit vector along the direction of the induced polarization, $\hat{\mathbf{b}}$, $\hat{\mathbf{c}}$, and $\hat{\mathbf{d}}$ are unit vectors along the polarization direction of the interacting fields, and $\hat{\mathbf{a}}_i$, $\hat{\mathbf{b}}_i$, $\hat{\mathbf{c}}_i$, and $\hat{\mathbf{d}}_i$ are the direction cosines of these unit vectors. For example, along the ⟨110⟩ and ⟨111⟩ directions, the effective susceptibilities are $\chi^{\langle 110\rangle}_{\mathrm{eff}} = (\chi^{(3)}_{1111} + 3\chi^{(3)}_{1122})/2$ and $\chi^{\langle 111\rangle}_{\mathrm{eff}} = (\chi^{(3)}_{1111} + 6\chi^{(3)}_{1122})/3$. The wavelength dependence of both nonlinear coefficients is discussed in Subsection 4.4.

The growth in Si photonics has recently led to several new measurements of the nonlinear optical susceptibility $\chi^{(3)}$, typically via the TPA coefficient, β_{TPA}, and the Kerr nonlinearity, n_2; the first of these measurements was obtained by Dinu *et al.* [108] in the vicinity of 1550 nm. Dinu also carried out a theoretical analysis of the dispersion curves and scaling rules for phonon-assisted third-order nonlinear optical coefficients of Si [109]. Recently, more comprehensive measurements of Si's nonlinear parameters were performed by Bristow *et al.* [110] and Lin *et al.* [111].

The wavelength dependence of β_{TPA} and n_2 have been particularly closely examined over the range from ~1100–2100 nm. The results of these measurements are shown in Fig. 6. In the case of β_{TPA}, the data, along with a recent theoretical investigation [112], show that this parameter has a broad peak at $\sim E_{ig}$, the indirect bandgap energy, and slowly decreases by a factor of

Figure 6

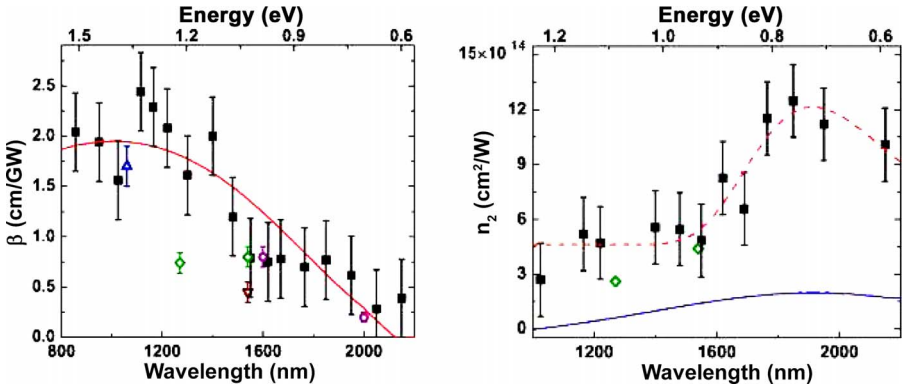

Measured value of β_{TPA} and n_2 versus wavelength as described in [110]. The solid curve in the left panel is a best fit based on the theory of Garcia and Kalyanaraman [112]. Right, n_2 (squares) versus wavelength; in this panel the dashed curve is a guide to the eye and the solid curve is based on a Kramers–Krönig transformation of the solid curve for β_{TPA} shown in the left panel. Most data shown here were taken by Bristow *et al.* [110].

$\sim 1/8$ at 2000 nm and is essentially zero at $\sim$2100 nm. The behavior of β_{TPA} shown in this plot is a sum of the contributions from three sets of indirect transitions—forbidden–forbidden, allowed–forbidden, and allowed–allowed—and the theory describing this behavior is in good agreement with the data. On the other hand, the value of the Kerr nonlinearity, also shown in Fig. 6, behaves in the opposite manner and increases with wavelength. Its value increases by a factor of $\sim$4 in going from 1550 to 1800 nm. It is possible to relate the wavelength dependence of n_2 to β_{TPA} via a Kramers–Krönig-type transformation, and this relation is shown by the solid curve in Fig. 6. While the shape of the solid curve is correct, it is obviously much lower than the measured data; this difference is attributed to the neglect of Raman and quadratic Stark contributions.

3.2. Raman Response

In Si, as in other crystalline solids, Raman scattering constitutes an additional third-order nonlinear optical process. In stimulated Raman scattering, two optical pulses, whose spectral difference is close to that of the strong Si Raman vibrational frequency, copropagate through a SPW. In this case, pulse dynamics are driven by a nonlinear process that couples light and phonons, namely, stimulated Raman scattering. If the spectral spacing of the two center frequencies does not match within a few Raman linewidths of the Raman frequency, the copropagating beams interact not via the Raman process, but, as is the case with XPM, rather only through the Kerr nonlinearity.

Consider the Raman process now in more specific detail. When a quasi-monochromatic pump wave at frequency ω_p propagates in a Raman-active solid medium such as crystalline Si, it creates a scattered Stokes signal at the frequency ω_s, which is downshifted with respect to ω_p by the Raman frequency $\omega_R=\omega_p-\omega_s$, corresponding to the frequency of optical phonons at the Brillouin-zone center. For Si, this frequency shift is $\omega_R/2\pi=15.6$ THz [113], with a spectral width of $\Delta\omega/2\pi=105$ GHz, which amounts to a response time of the Raman interaction of $\tau\sim 10$ ps. If the pulse widths of the pump and Stokes pulses are comparable with or less than the Raman response time, the interaction of the two pulses is strongly driven by the third-order nonlinear Raman susceptibility at frequency ω_R.

Now let us consider the Raman nonlinear polarization, $\mathbf{P}_R$ via the third-order Raman susceptibility $\boldsymbol{\chi}^R$, defined as [114–118]

$$\chi^R_{ijkl}(\Omega)=\frac{\pi N_v}{3\hbar}\sum_{\sigma}\frac{\omega_\sigma(\alpha_{ij,\sigma}\alpha_{kl,\sigma}+\alpha_{ik,\sigma}\alpha_{lj,\sigma})}{\omega_\sigma^2-\Omega^2+2i\Omega\Delta\omega}, \tag{8}$$

where $\Omega=\omega_1-\omega_2$, ω_1 and ω_2 are the input frequencies, N_v is the number of vibrational oscillators per unit volume, ω_σ is the vibrational resonant frequency, and the matrix elements $\alpha_{ij,\sigma}$ are given by the derivatives of the polarizability tensor $\hat{\boldsymbol{\alpha}}$ with respect to the coordinate of the normal mode σ. There are three degenerate Raman-active optical phonons in Si with $\omega_\sigma=\omega_R$ ($\sigma=1,2,3$), having the symmetry of the irreducible representation $\Gamma_{25'}$, and the corresponding Raman tensors are given by [118]

$$R_1=\begin{pmatrix}0&0&0\\0&0&1\\0&1&0\end{pmatrix},\quad R_2=\begin{pmatrix}0&0&1\\0&0&0\\1&0&0\end{pmatrix},\quad R_3=\begin{pmatrix}0&1&0\\1&0&0\\0&0&0\end{pmatrix}. \tag{9}$$

Because of this symmetry property there is only one independent component of the Raman tensor, namely, χ^R_{1122}. Furthermore, close to the Raman resonance $\Omega \approx \omega_R$, and Eq. (8) becomes

$$\chi^R_{ijkl}(\Omega) = \frac{\pi N_v}{6\hbar} \sum_\sigma \frac{\alpha_{ij,\sigma}\alpha_{kl,\sigma} + \alpha_{ik,\sigma}\alpha_{lj,\sigma}}{\omega_R - \Omega + i\Delta\omega}. \tag{10}$$

The real part of this susceptibility describes parametric processes that lead to a change in the refractive index, whereas the imaginary part of the Raman susceptibility describes the Raman amplification process. At resonance, $\Omega = \omega_R$, the Raman susceptibility is pure imaginary, its value being $\chi^R_{1212}|_{\Omega=\omega_R} \equiv -i\chi_R = -i11.2 \times 10^{-18}$ m^2 V^{-2}. Under these conditions, the Raman part of the nonlinear polarization can be written as

$$\begin{aligned}\mathbf{P}_R = \frac{3}{2}\varepsilon_0 [&\boldsymbol{\chi}^R(-\omega_R) \vdots \mathbf{E}(\mathbf{r},\omega_s)\mathbf{E}^*(\mathbf{r},\omega_s)\mathbf{E}(\mathbf{r},\omega_p)\delta(\omega-\omega_p) \\ &+ \boldsymbol{\chi}^R(\omega_R) \vdots \mathbf{E}(\mathbf{r},\omega_p)\mathbf{E}^*(\mathbf{r},\omega_p)\mathbf{E}(\mathbf{r},\omega_s)\delta(\omega-\omega_s)].\end{aligned} \tag{11}$$

Note that, since $\boldsymbol{\chi}^R(\Omega) = \boldsymbol{\chi}^{R*}(-\Omega)$, the Raman interaction leads to the amplification of the Stokes signal, whereas it acts as a loss term at the frequency of the pump. Of course the total nonlinear polarization must include both the Raman and the electronic contributions, $\mathbf{P}_{\mathrm{NL}} = \mathbf{P}_e + \mathbf{P}_R$. Manipulating these equations and using the same coupled-mode procedure as in the case of the pulse-propagation system to be described in Subsection 4.2, one may obtain the final set of coupled partial differential equations that describe the dynamics of Raman-mediated pulse propagation in a SPW [92]. Because of the overall similarity of the equations to those to be presented below, we will not examine these pulse dynamics in detail. Instead we will limit our discussion below to a more heuristic discussion of Raman amplification and its potential use in integrated optics.

3.3. Effective Nonlinear Susceptibility in Si Photonic Wires

In characterizing the nonlinear optical properties of SPW waveguides, it is essential to evaluate the nonlinear response averaged over the waveguide modes. This averaging has important results for Si photonics, since it yields a significant difference than that expected from the usual approximations in fiber optics. To carry out this evaluation we define the parameter Γ, which measures the effective nonlinear susceptibility, as the weighted integral of the corresponding tensor susceptibility $\boldsymbol{\chi}^{(3)}$ over waveguide modes of the Si wire (the origin of this definition will become apparent in Subsection 4.1, where this coefficient is rigorously derived):

$$\Gamma = \frac{A_0 \int_{A_0} \mathbf{e}^*(\mathbf{r}_\perp;\omega)\boldsymbol{\chi}^{(3)}(\mathbf{r}_\perp;-\omega,\omega,-\omega,\omega) \vdots \mathbf{e}(\mathbf{r}_\perp;\omega)\mathbf{e}^*(\mathbf{r}_\perp;\omega)\mathbf{e}(\mathbf{r}_\perp;\omega)dA}{(\int_{A_\infty} n^2(\mathbf{r}_\perp)|\mathbf{e}(\mathbf{r}_\perp,\omega)|^2 dA)^2}, \tag{12}$$

where $A_0 = h \times w$ is the area of the transverse section of the waveguide, A_∞ denotes integration over the entire transverse plane, and $\mathbf{e}(\mathbf{r}_\perp;\omega)$ is the electric field profile of the waveguide mode; for a SPW whose transverse section is

uniform along the wire the waveguide modes depend only on the transverse coordinate, $\mathbf{r}_\perp$. The specific dependence of Γ on the transverse profile of the index of refraction, $n(\mathbf{r}_\perp)$, is determined by the mode energy density, which is proportional to the dielectric constant, $\varepsilon(\mathbf{r}_\perp)=n^2(\mathbf{r}_\perp)$. Explicitly, $n(\mathbf{r}_\perp)=n$ inside the waveguide, and $n(\mathbf{r}_\perp)=n_{\text{cladding}}$ outside the waveguide, where n denotes the refractive index of Si, and n_{cladding} is the index of refraction of either air or the oxide layer. In addition, the nonlinear susceptibility tensor elements $\chi^{(3)}_{ijkl}$ of the tensor $\boldsymbol{\chi}^{(3)}$ are known in the crystal principal axes, whereas the modal fields are numerically determined in the waveguide system; thus, the susceptibility tensors must be transformed first in the waveguide system. For a SPW with dimensions $h\times w=220$ nm $\times 360$ nm at wavelength $\lambda=1550$ nm, the corresponding value of the effective susceptibility is found to be $\Gamma=\Gamma'+i\Gamma''=(1.13\times 10^{-21}+i3.45\times 10^{-22})$ m^2 V^{-2}.

3.4. Carrier Dynamics in Si Photonic Wires

For a full description of optical pulse interaction in a Si-wire waveguide, it is essential to include the formation of free carriers by the TPA mechanism described earlier. These carriers can interact with the propagating beam either by adding linear absorption or by causing a wavelength-dependent change in the index and, hence, phase in the system. These effects are quantified according to the following relations [10]:

$$\delta n_{\text{FC}}=-\frac{e^2}{2\varepsilon_0 n\omega^2}\left(\frac{N}{m^*_{ce}}+\frac{N^{0.8}}{m^*_{ch}}\right),$$

$$\alpha_{\text{FC}}=\frac{e^3 N}{\varepsilon_0 cn\omega^2}\left(\frac{1}{\mu_e m^*_{ce}}+\frac{1}{\mu_h m^{*2}_{ch}}\right), \tag{13}$$

where δn_{FC} is the free-carrier-induced change in the refractive index, α_{FC} is the free-carrier absorption (FCA) coefficient, N is the carrier density, $m^*_{ce}=0.26m_0$ and $m^*_{ch}=0.39m_0$ are the effective masses of the electron and the hole, respectively, with m_0 as the mass of the electron, and μ_e (μ_h) is the electron (hole) mobility. Note that in Eqs. (13) it is assumed that the carrier density for electrons and holes is the same.

Note that optical free-carrier generation and decay via recombination gives rise to temporal variation in carrier density in the presence of pulsed light. Thus, the optical power absorption per unit length due to TPA can be written as (see also Subsection 4.1)

$$\left.\frac{\partial P}{\partial z}\right|_{\text{TPA}}=-\frac{3\omega\beta_1^2 P_0^2\Gamma''}{2\varepsilon_0 A_0}|u|^4, \tag{14}$$

where $P(z,t)=P_0|u(z,t)|^2$, P_0 is the input peak optical power, and u is the normalized field amplitude. With this expression for TPA, the rate equation can be cast in the following form:

$$\frac{\partial N}{\partial t} = -\frac{N}{t_c} + \frac{3\beta_1^2 P_0^2 \Gamma''}{4\varepsilon_0 \hbar A_0^2}|u|^4, \tag{15}$$

where the characteristic lifetime of the free carriers, t_c, is assumed to be the same for both electrons and holes. In bulk Si or in large waveguides, i.e., of micrometer-scale transverse dimensions, this characteristic time is a few tens of nanoseconds. In submicrometer Si structures, however, owing to the fast diffusion of free carriers to the edges of the waveguide, this relaxation time is reduced to ~0.5 ns [119].

4. Theory of Nonlinear Optical Pulse Propagation and Dynamics in Si Photonic Wires

For a complete understanding of both the linear and the nonlinear optical properties of SPWs, it is necessary to describe both the dynamics of the optical field upon propagation in these guiding structures and the subtle interactions between the photogenerated free carriers and the propagating optical field. Some aspects of this intricate interplay between optical and free-carrier-induced effects have been alluded to in the preceding section; in this section we present a detailed description of the nonlinear optical pulse propagation and dynamics in SPWs, pointing out important aspects that differentiate this dynamics from that of pulses propagating in optical fibers or other optical waveguides.

Readers familiar with pulse propagation in standard fiber optic waveguides should note at the onset that the materials and propagation equations have important differences from those in wires. First, the crystallinity of Si requires that its nonlinear optical properties be treated as tensors. This requirement makes the use of the nonlinear optical susceptibility a more natural parameter in many cases than the more familiar **scalar** nonlinear parameters used to describe isotropic glass fibers. Second, the tight confinement in Si waveguides causes the cross-section dependence of the group velocity to often be significantly different than that of the bulk medium; this effect makes certain overlap integrals used in the calculation of certain parameters that describe the pulse propagation to be considerably different from those in standard fiber optics. Finally, the wavelength dependence of the optical properties of waveguides is far more pronounced than for the case of fibers; this dependence can make calculation of nonlinear propagation take on a somewhat different character than in standard fibers. Note, of course, that in the case of structured fibers, these issues are similar to those encountered in Si wires but to a much lesser degree.

4.1. Theory of Light Propagation in Si Photonic Wires

To derive the system of equations that governs the dynamics of optical pulses propagating in a Si-wire waveguide, we start from the conjugated form of the Lorentz reciprocity theorem (see, e.g., [120]):

$$\frac{\partial}{\partial z}\int_{A_\infty}\mathbf{F}_c\cdot\hat{\mathbf{e}}_z dA=\int_{A_\infty}\nabla\cdot\mathbf{F}_c dA, \tag{16}$$

where the integral is taken over the entire transverse plane, $\hat{\mathbf{e}}_z$ is the unit vector oriented along the longitudinal axis of the waveguide, and the vector field $\mathbf{F}_c$ is constructed with two arbitrary guided electromagnetic fields $(\mathbf{E}_1,\mathbf{H}_1)$ and $(\mathbf{E}_2,\mathbf{H}_2)$,

$$\mathbf{F}_c=\mathbf{E}_1^*\times\mathbf{H}_2+\mathbf{E}_2\times\mathbf{H}_1^*. \tag{17}$$

Now consider that $(\mathbf{E}_1,\mathbf{H}_1)\equiv(\mathbf{E}_0,\mathbf{H}_0)$ is the electromagnetic field corresponding to a mode of the unperturbed waveguide and $(\mathbf{E}_2,\mathbf{H}_2)\equiv(\mathbf{E},\mathbf{H})$ is the electromagnetic field of the same mode propagating in a waveguide whose optical characteristics (namely, its dielectric constant) are perturbed by the generation of free carriers and the induced nonlinear polarization. Then, Eq. (16) becomes

$$\frac{\partial}{\partial z}\int_{A_\infty}(\mathbf{E}_0^*\times\mathbf{H}+\mathbf{E}\times\mathbf{H}_0^*)\cdot\hat{\mathbf{e}}_z dA=i\omega\int_{A_\infty}\delta\mathbf{P}\cdot\mathbf{E}_0 dA, \tag{18}$$

where $\delta\mathbf{P}=\delta\mathbf{P}_{\mathrm{L}}+\mathbf{P}_{\mathrm{NL}}$. By simply taking the divergence of the vector field $\mathbf{F}_c$ and using Maxwell's equations to simplify the result, one obtains the integrand on the right-hand side of Eq. (18). Note that in deriving this equation it is assumed that the variation of the dielectric constant (index of refraction) is small, and thus the modes of the perturbed and unperturbed waveguides are the same (see [120]). The change in the linear polarization is determined by the variation of the dielectric constant induced by the generation of free carriers, $\delta\mathbf{P}_{\mathrm{L}}=\delta\varepsilon_{\mathrm{L}}\mathbf{E}$, where $\delta\varepsilon_{\mathrm{L}}$ is given by the following relation:

$$\delta\varepsilon_{\mathrm{L}}=i\frac{\varepsilon_0 cn\alpha_{\mathrm{in}}}{\omega}+2\varepsilon_0 n\delta n_{\mathrm{FC}}+i\frac{\varepsilon_0 cn\alpha_{\mathrm{FC}}}{\omega}, \tag{19}$$

where α_{in} is the intrinsic loss coefficient and δn_{FC} and α_{FC} are given by Eqs. (13). For the unperturbed fields, we choose the following:

$$\mathbf{E}_0=\frac{1}{2}\sqrt{\frac{Z_0P_0}{A_0}}\mathbf{e}(\mathbf{r}_\perp,\omega_0)e^{i(\beta_0 z-\omega_0 t)},$$

$$\mathbf{H}_0=\frac{1}{2}\sqrt{\frac{P_0}{Z_0A_0}}\mathbf{h}(\mathbf{r}_\perp,\omega_0)e^{i(\beta_0 z-\omega_0 t)} \tag{20}$$

with $Z_0=\sqrt{\mu_0/\varepsilon_0}$ as the free-space impedance, and the waveguide modes are normalized such that

$$\frac{1}{4A_0}\int_{A_\infty}(\mathbf{e}\times\mathbf{h}^*+\mathbf{e}^*\times\mathbf{h})\cdot\hat{\mathbf{e}}_z dA=1. \tag{21}$$

With this normalization, the electromagnetic field $(\mathbf{E}_0,\mathbf{H}_0)$ carries a total optical power P_0. Furthermore, the fields in the perturbed waveguide are expressed as

$$\mathbf{E} = \frac{1}{2}\sqrt{\frac{Z_0 P_0}{A_0}}u(z,\omega)\mathbf{e}(\mathbf{r}_\perp,\omega)e^{i(\beta z-\omega t)},$$

$$\mathbf{H} = \frac{1}{2}\sqrt{\frac{P_0}{Z_0 A_0}}u(z,\omega)\mathbf{h}(\mathbf{r}_\perp,\omega)e^{i(\beta z-\omega t)}, \tag{22}$$

where $u(z,\omega)$ is the complex mode amplitude normalized such that, in the time domain, its input peak amplitude is equal to 1. With normalization (21), the power carried by the electromagnetic field $(\mathbf{E},\mathbf{H})$ is $P_0|u(z,\omega)|^2$. Inserting Eqs. (19), (20), and (22) into Eq. (18), expanding the propagation constant $\beta(\omega)$ in a Taylor series around the carrier frequency ω_0, and Fourier transforming the resulting equation in the time domain, we arrive at the following partial differential equation for the mode amplitude $u(z,t)$:

$$i\left(\frac{\partial u}{\partial z}+\frac{1}{v_g}\frac{\partial u}{\partial t}\right)-\frac{\beta_2}{2}\frac{\partial^2 u}{\partial t^2}-i\frac{\beta_3}{6}\frac{\partial^3 u}{\partial t^3}=-\frac{ic\kappa}{2nv_g}(\alpha_{\text{in}}+\alpha_{\text{FC}})u-\frac{\omega\kappa}{nv_g}\delta n_{\text{FC}}u$$
$$-\frac{3\omega P_0\Gamma}{4\varepsilon_0 A_0 v_g^2}|u|^2u, \tag{23}$$

where, for simplicity, the subscript was dropped from the carrier frequency ω_0. Here, the effective waveguide susceptibility Γ is defined by Eq. (12), and the parameter κ is given by the overlap integral

$$\kappa = \frac{n^2\int_{A_0}|\mathbf{e}(\mathbf{r}_\perp)|^2dA}{\int_{A_\infty}n^2(\mathbf{r}_\perp)|\mathbf{e}(\mathbf{r}_\perp)|^2dA}. \tag{24}$$

Note that for the nonlinear part of the variation of the polarization, $\delta\mathbf{P}$, we have used expression (5). It is important that, in deriving Eq. (23), we have used the relation $P_0 = v_g W_t$ [120] between the mode power P_0 and the mode energy density per unit length, W_t; with definition (20), the latter is given by

$$W_t = \frac{Z_0 P_0}{2A_0}\int_{A_\infty}\varepsilon_0 n^2(\mathbf{r}_\perp)|\mathbf{e}(\mathbf{r}_\perp)|^2dA. \tag{25}$$

It is important to note that definition (12) applies not only to the electronic nonlinear susceptibility but also to the Raman interaction [92].

Relation (24), which defines the parameter κ, reveals an important effect, namely, that only a fraction of the optical power carried by the mode generates carriers [121,122]. This effect is a direct consequence of the fact that the mode profile only partially overlaps with the Si wire; for example, numerical calculations show that for typical SPWs, $\kappa \sim 0.75-0.95$. The carrier dynamics can be readily determined from Eq. (23). Thus, since the optical power is $P_0|u|^2$, Eq. (23) implies that the power loss per unit propagation length is given by Eq. (14), and thus the corresponding rate of carrier generation due to TPA can be determined by simply dividing this power loss per unit length by the energy required to generate an electron–hole pair, which is equal to $2\hbar\omega$. As a result, the time evolution of the carrier density is given by Eq. (15). The two coupled equations (23) and (15) represent the basic theoretical

model that is used to investigate a series of linear and nonlinear optical effects pertaining to the propagation of optical pulses in SPWs.

4.2. Coupled-Mode Equations for Multifrequency Pulse Propagation

As we just discussed, the pulse dynamics for Si wires are governed by the interplay of dispersion and nonlinear optical effects whose relative strengths are determined by several characteristic lengths, namely, the second-order dispersion and TOD lengths, defined as $L_D = T_0^2/|\beta_2|$ and $L_D' = T_0^3/|\beta_3|$, respectively, and the nonlinear length L_{NL}, whose definition will be given in Subsection 4.5. In addition, the influence of the photogenerated free carriers must also be incorporated into a rigorous theoretical model that describes this pulse dynamics. Thus a comprehensive theoretical model describing pulse propagation in SPWs must include both nonlinear and linear optical effects and the strongly dispersive properties of the Si medium. These nonlinear and linear optical phenomena include SPM, TPA, and FCA [123,124] and free-carrier-induced optical dispersion and are primarily related to the evolution of an optical pulse centered at a fixed frequency. However, in many applications of practical interest, such as light amplification or signal multiplexing–demultiplexing, two or more optical pulses copropagate in the same Si wire, and therefore important nonlinear effects such as XPM, multimode mixing, birefringence effects, or stimulated Raman scattering must be incorporated into the theoretical model.

Coupled-mode theory [92,77] has been developed to account fully for these linear and nonlinear optical effects. Thus, in the case of copropagation of two optical pulses corresponding to the same waveguide mode but having different carrier frequencies, the main changes to the formalism presented in Subsection 4.1 consist in replacing the nonlinear polarization, Eq. (5), by a more general expression, which also includes a XPM term:

$$\begin{aligned}\mathbf{P}_{\mathrm{NL}}(\mathbf{r},\omega) = \frac{3}{4}\varepsilon_0\{&[\boldsymbol{\chi}^{(3)}(\omega_s;\omega_s,-\omega_s,\omega_s)\vdots\mathbf{E}(\mathbf{r},\omega_s)\mathbf{E}^*(\mathbf{r},\omega_s)\mathbf{E}(\mathbf{r},\omega_s)\\ &+2\boldsymbol{\chi}^{(3)}(\omega_s;\omega_s,-\omega_p,\omega_p)\vdots\mathbf{E}(\mathbf{r},\omega_s)\mathbf{E}^*(\mathbf{r},\omega_p)\mathbf{E}(\mathbf{r},\omega_p)]\delta(\omega-\omega_s)\\ &+[\boldsymbol{\chi}^{(3)}(\omega_p;\omega_p,-\omega_p,\omega_p)\vdots\mathbf{E}(\mathbf{r},\omega_p)\mathbf{E}^*(\mathbf{r},\omega_p)\mathbf{E}(\mathbf{r},\omega_p)\\ &+2\boldsymbol{\chi}^{(3)}(\omega_p;\omega_p,-\omega_s,\omega_s)\vdots\mathbf{E}(\mathbf{r},\omega_p)\mathbf{E}^*(\mathbf{r},\omega_s)\mathbf{E}(\mathbf{r},\omega_s)]\delta(\omega-\omega_p)\},\end{aligned} \tag{26}$$

where ω_p and ω_s are the frequencies of the copropagating pulses, i.e., the pump and the signal, respectively. Under these circumstances, the set of corresponding coupled equations describing the slowly varying normalized complex envelopes $u_p(z,t)$ and $u_s(z,t)$ of the copropagating pump and signal (probe) pulses, respectively, can then be written as

$$i\left(\frac{\partial u_p}{\partial z}+\frac{1}{v_{g,p}}\frac{\partial u_p}{\partial t}\right)-\frac{\beta_{2,p}}{2}\frac{\partial^2 u_p}{\partial t^2}-i\frac{\beta_{3,p}}{6}\frac{\partial^3 u_p}{\partial t^3}=-\frac{ic\kappa_p}{2nv_{g,p}}(\alpha_{\mathrm{in}}+\alpha_{\mathrm{FC}}^p)u_p$$

$$-\frac{\omega_p\kappa_p}{nv_{g,p}}\delta n_{\mathrm{FC}}^p u_p-\frac{3\omega_p}{4\varepsilon_0 A_0 v_{g,p}}\left(\frac{P_p\Gamma_p}{v_{g,p}}|u_p|^2+2\frac{P_s\Gamma_{sp}}{v_{g,s}}|u_s|^2\right)u_p,$$

$$i\left(\frac{\partial u_s}{\partial z}+\frac{1}{v_{g,s}}\frac{\partial u_s}{\partial t}\right)-\frac{\beta_{2,s}}{2}\frac{\partial^2 u_s}{\partial t^2}-i\frac{\beta_{3,s}}{6}\frac{\partial^3 u_s}{\partial t^3}=-\frac{ic\kappa_s}{2nv_{g,s}}(\alpha_{\mathrm{in}}+\alpha_{\mathrm{FC}}^s)u_s-\frac{\omega_s\kappa_s}{nv_{g,s}}\delta n_{\mathrm{FC}}^s u_s$$

$$-\frac{3\omega_s}{4\varepsilon_0 A_0 v_{g,s}}\left(\frac{P_s\Gamma_s}{v_{g,s}}|u_s|^2+2\frac{P_p\Gamma_{ps}}{v_{g,p}}|u_p|^2\right)u_s,$$

$$\frac{\partial N}{\partial t}=-\frac{N}{t_c}+\frac{3}{4\varepsilon_0\hbar A_0^2}\left[\frac{P_p^2\Gamma_p''}{v_{g,p}^2}|u_p|^4+\frac{P_s^2\Gamma_s''}{v_{g,s}^2}|u_s|^4+\frac{4(\omega_p\Gamma_{sp}''+\omega_s\Gamma_{ps}'')P_pP_s}{(\omega_p+\omega_s)v_{g,p}v_{g,s}}|u_pu_s|^2\right], \tag{27}$$

where, similarly to Eq. (12), the effective susceptibility Γ_{ps} is defined as

$$\Gamma_{ps}=\frac{A_0\int_{A_0}\mathbf{e}^*(\mathbf{r}_\perp;\omega_s)\boldsymbol{\chi}^{(3)}(\mathbf{r}_\perp;\omega_s;\omega_s,-\omega_p,\omega_p)\vdots\,\mathbf{e}(\mathbf{r}_\perp;\omega_p)\mathbf{e}^*(\mathbf{r}_\perp;\omega_p)\mathbf{e}(\mathbf{r}_\perp;\omega_s)dA}{(\int_{A_\infty}n^2(\mathbf{r}_\perp)|\mathbf{e}(\mathbf{r}_\perp,\omega_p)|^2dA)(\int_{A_\infty}n^2(\mathbf{r}_\perp)|\mathbf{e}(\mathbf{r}_\perp,\omega_s)|^2dA)}, \tag{28}$$

and in the case of Γ_{sp} the indices p and s in Eq. (28) are reversed. Note that this analysis can easily be extended to include the Raman interaction [92] or multimode pulse copropagation by simply adding the corresponding nonlinear polarization, e.g., Eq. (11) in the case of Raman interaction, to the perturbed polarization $\delta\mathbf{P}$.

In general, the overall nonlinear phase shift of copropagating optical pulses has two sources: SPM, which is the change in refractive index induced by the same pulse, and XPM, which is change of the refractive index induced by one pulse and on a second copropagating pulse. If the powers of both pulses are such that dispersion and nonlinear terms in the first two equations in Eqs. (27) have comparable magnitudes, the nonlinearly induced phase shifts can be found only by numerically solving these equations. If, however, the SPM and XPM terms in these equations dominate, one can derive [101] an analytic formula for the nonlinearly induced phase shift of the probe, φ_s. This analytic result is useful in giving insight into the basic pulse propagation effects on pulse phase and frequency shifts.

To derive this analytic equation, the effect of TPA is neglected to yield the nonlinear phase shift $\varphi_s(z,T)$ as

$$\varphi_s(z,T)=z\gamma_sP_s|u_s(0,T)|^2+2\gamma_{ps}P_p\int_0^z|u_p(0,T+z'\Delta)|^2dz'. \tag{29}$$

Here, $T=t-z/v_{g,p}$ is the time in the reference frame of the pump pulse. In addition it is convenient to use the standard nonlinear coefficients

$$\gamma_i=\frac{3\omega_i\Gamma_i}{4\varepsilon_0A_0v_{g,i}^2}, \tag{30}$$

$$\gamma_{ji} = \frac{3\omega_i \Gamma_{ji}}{4\varepsilon_0 A_0 v_{g,j} v_{g,i}}, \tag{31}$$

which describe SPM and XPM interactions, respectively, with i or $j=\{s,p\}$, and $\Delta = 1/v_{g,s} - 1/v_{g,p}$ describes the temporal walk-off. For a weak probe pulse, the first term of Eq. (29) can be neglected, and, assuming that both pump and probe are Gaussian pulses of temporal width T_p, namely, $u_p(0,T) = \exp[-(T-T_d)^2/2T_p^2]$ and $u_s(0,T) = \exp(-T^2/2T_s^2)$, we obtain the XPM-induced phase shift in Eq. (29):

$$\varphi_s(z,\tau) = \frac{\gamma_{ps} P_p z \sqrt{\pi}}{\delta} [\mathrm{erf}(\tau - \tau_d + \delta) - \mathrm{erf}(\tau - \tau_d)], \tag{32}$$

where $\tau = T/T_p$, $\tau_d = T_d/T_p$, and $\delta = z\Delta/T_p$. T_d is defined as the temporal separation between the maximum intensity points of these two pulses prior to their entry into the waveguide. Here this time delay is positive (negative) when the probe leads (trails) the pump. Equation (32) also provides the frequency shift of the probe due to the XPM-driven index change,

$$\delta\omega_s(z,\tau) = -\frac{1}{T_p}\frac{\partial \varphi_s(z,\tau)}{\partial \tau} = -\frac{2\gamma_{ps} P_p z}{T_p \delta}\{\exp[-(\tau - \tau_d + \delta)^2] - \exp[-(\tau - \tau_d)^2]\}. \tag{33}$$

This equation shows clearly that the frequency shift is proportional to the product of the pulse power and the nonlinearity and is reduced by any mismatch in the velocity of the signal and pump pulses, i.e., the GVD. In Subsection 6.4, Eqs. (32) and (33) will be used to explain experimental results regarding XPM.

4.3. Effects of Strong Optical Confinement on Optical Nonlinearity

Optical-pulse propagation in a Si wire responds to same basic nonlinear physics as in optical fibers. However, as mentioned earlier, there are important differences due to the strong dispersion in the waveguides, which is a result of the strong optical confinement in SPWs, and due to the crystalline nature of the Si crystal. Let us examine the effects of dispersion here by examining its effect on the propagation of a single pulse through a Si wire. The pulse dynamics are governed by the coupled nonlinear differential equations (23) and (15) [92,77]. By inspection of the last term of the right-hand side of Eq. (23), one can define the optical nonlinearity of a waveguide to be $\gamma = 3\omega\Gamma/4\varepsilon_0 A_0 v_g^2$. Notice that the effects of waveguide confinement become manifest through this expression; for the case of optical fibers, it reduces to the case of the considerably different but well-known expression, $\gamma = n_2\omega/cA_{\mathrm{eff}}$, where A_{eff} is the effective modal area, defined as a weighted integral over the transverse field profile, used in describing the nonlinear property of optical fibers. This difference arises from the large disparity between the group indices for small- and large-cross-section waveguides. In typical cases, the group index n_g, which is proportional to β_1, may increase as the size of the cross section decreases, as can be seen in Fig. 2 for wavelengths $\lambda < 1.58\ \mu$m. For example, in slow-light guiding structures group indices of order 10^2–10^3 are

common. This increase in n_g leads to a decrease in the group velocity $v_g = 1/\beta_1$, which provides a further enhancement in the effective nonlinearity in addition to the effect of decreased area A_0. Note also that for small-cross-section waveguides with high index contrast γ depends on the group index and not the effective index (mode index).

In the limit of low-index contrast structures such as optical fibers, the general expression (30) for γ reduces to the standard definition of γ. Thus, there exists a significant distinction between high- and low-index-contrast waveguide structures. The latter or standard optical fiber expression for γ neglects the nonlinear anisotropy of Si, the contribution to γ of the longitudinal component of the electric field, and the strong spatial inhomogeneity of the waveguide mode. Note, however, that an effective area can be introduced in the case of Si wires, too, but the definition of A_{eff} is different from that in optical fibers [125]. For the case of a SPW, the large difference between n_g and n makes it important to use the expression for γ given above in describing the nonlinear optical behavior of wave propagation in such waveguides. As Eq. (12) shows, the parameter Γ plays the role of the effective third-order susceptibility of the waveguide, and therefore, by analogy with relation (6), valid for a bulk nonlinear medium, the quantities Γ' and Γ'' can be used to define an effective Kerr nonlinear refractive index of the waveguide, $n_{2,\text{wg}}$, and an effective TPA coefficient, $\beta_{\text{TPA,wg}}$, respectively, according to

$$n_{2,\text{wg}} = \frac{3\Gamma'}{4\varepsilon_0 c n^2}, \tag{34}$$

$$\beta_{\text{TPA,wg}} = \frac{3\omega\Gamma''}{2n^2c^2\varepsilon_0}. \tag{35}$$

As discussed in Subsection 4.4, the value of Γ strongly depends on the dimensions and geometry of the waveguide. Recently, Koos *et al.* showed that large values of nonlinearity could be obtained by optimizing the waveguide geometry [125] of strip and slot waveguides.

4.4. Frequency Dispersion of the Effective Optical Nonlinearity of Si Photonic Wires

As we discussed in Subsection 2.2, the tight optical-field confinement achieved in high-index-contrast SPWs leads to a strong dependence of the linear optical properties of these guiding structures on both the wire geometry as well as the corresponding material parameters; these properties include the waveguide modes and their propagation constants. It is therefore expected that the nonlinear properties of SPWs will also show large frequency dispersion, a property that would play a significant role in the dynamics of ultrashort or broadband optical pulses.

Since the nonlinear properties of SPWs are determined chiefly by the nonlinear coefficient γ, the frequency dispersion of the waveguide nonlinearity is fully characterized by its dependence on frequency, $\gamma(\omega)$. Thus, to quantify this important nonlinear effect, one has to determine the waveguide modes and the corresponding propagation constant β at a frequency ω and then use Eq. (30) to calculate the nonlinear coefficient γ. Now, to incorporate the frequency

dispersion of the material optical nonlinearity in this procedure explicitly, it is only necessary to use the frequency-dependent third-order susceptibility $\boldsymbol{\chi}^{(3)}(\omega)$ in the definition of Γ in Eq. (12) and thus account for the contribution of the material dispersion and, implicitly, for that of the waveguide dispersion, to the frequency dependence $\gamma(\omega)$. As explained in Subsection 3.1, the only independent component of the susceptibility, $\chi^{(3)}_{1111}$, can be determined from the experimentally measured [110] values of the Kerr coefficient, n_2, and the TPA coefficient, β_{TPA}, by using the following relations [see Eq. (6)]:

$$n_2 = \frac{3}{4\varepsilon_0 c n^2}\chi^{(3)\prime}_{\mathrm{eff}},$$

$$\beta_{\mathrm{TPA}} = \frac{3\omega}{2\varepsilon_0 c^2 n^2}\chi^{(3)\prime\prime}_{\mathrm{eff}}. \tag{36}$$

Here, the effective susceptibility $\boldsymbol{\chi}^{(3)}_{\mathrm{eff}}$ is defined by Eq. (7).

As a generic example, Fig. 7 illustrates the frequency dispersion of the nonlinear coefficient $\gamma(\omega)$, determined both for the case in which only the waveguide dispersion is considered and for the more general case when both the material and the waveguide dispersion are accounted for. The calculations

Figure 7

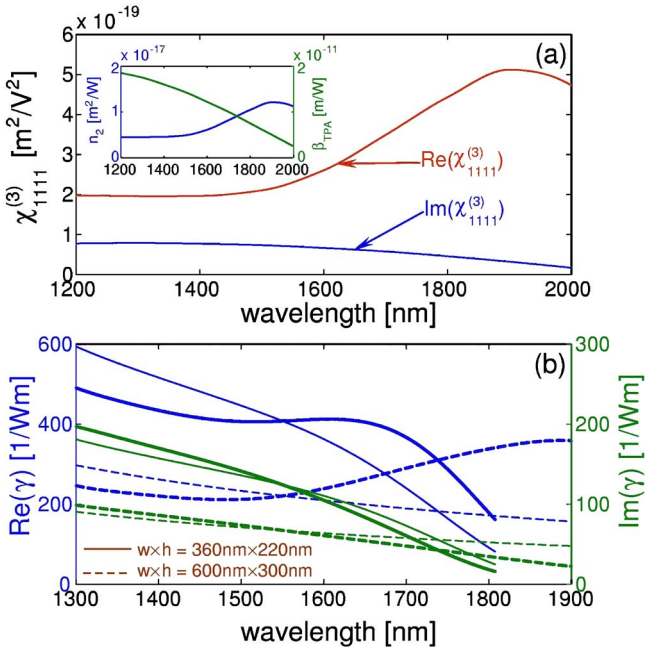

(a) Wavelength dependence of the susceptibility $\chi^{(3)}_{1111}$. (b) Real and imaginary parts of the nonlinear coefficient γ versus wavelength. Inset, interpolated values of experimentally measured bulk parameters n_2 and β_{TPA}. In (b), the thin and thick curves correspond to the case in which only the waveguide dispersion is considered and the case when both the material and the waveguide dispersion are included, respectively.

have been performed for two waveguides, one with dimensions $h \times w = 220$ nm $\times 360$ nm, which has the ZGVD wavelength at 1550 nm and the cutoff wavelength at 1808 nm, and the other waveguide with dimensions $h \times w = 300$ nm $\times 600$ nm. This figure shows that the waveguide nonlinearity depends strongly on wavelength; e.g., in the case of the first waveguide both the real and the imaginary parts of the nonlinear coefficient γ decrease more than three times within a spectral domain of 500 nm, between 1300 and 1800 nm. This decrease of γ at large wavelengths occurs because the mode becomes less confined in the Si core as the wavelength approaches the cutoff wavelength, and therefore a smaller amount of optical power is guided within the region with optical nonlinearity. As is shown in Subsection 4.6, this large variation of γ with frequency leads to a large characteristic optical shock time, an effect that has important implications for the dynamics of ultrashort optical pulses. Also, Fig. 7 shows that not only do the linear properties of SPWs depend strongly on the waveguide dimensions but also that their nonlinear optical properties (namely, the nonlinear coefficient γ) change significantly with the transverse waveguide dimensions.

4.5. Characteristic Lengths in Si Photonic Wires versus Optical Fibers

The above treatments show that, as optical pulses propagate in Si wires, their evolution in both the time and the frequency domains, is governed by the interplay of the linear dispersion and nonlinearity. These effects are characterized by several characteristic lengths, namely, the GVD length L_D, the TOD length L'_D, and the nonlinear length L_{NL}, defined as $L_{\mathrm{NL}} = 4\varepsilon_0 A_0 v_g^2 / 3\omega P_0 \Gamma'$. For picosecond or longer pulses with $P_0 = 0.2$ W or larger, $L_{\mathrm{NL}}/L_D \ll 1$ and $L_{\mathrm{NL}}/L'_D \ll 1$. In this case, the second and the third terms on the left-hand side of Eq. (23) may be ignored, and SPM dominates the pulse evolution inside the waveguide. If, instead, the pulse width is in the femtosecond regime, L_D, L'_D, and L_{NL} are comparable for milliwatt-level powers. A useful parameter is the soliton number, $N_{\mathrm{soliton}} = (L_D/L_{\mathrm{NL}})^{1/2}$, which is a measure of the strength of solitonic effects.

To appreciate the importance of these length scales, Table 1 presents specific values of these characteristic lengths for $T_0 = 200$ fs and 10 ps for a SPW. The short-pulse case is then compared with that of a typical single-mode optical fiber. The values for the characteristic lengths, $L_D \approx 10$ mm and $L'_D \approx 11$ mm, are based on calculations and measurements for the 220 nm $\times$ 450 nm waveguide cross section. The nonlinear length L_{NL} depends on power; e.g., if P_0

Table 1. Comparison of Characteristic Lengths for Ultrashort (200 fs) and Long (10 ps) Pulses and γ Parameter in a SPW (dimensions $h \times w = 220 \times 450$ nm^2) and a Single-Mode Optical Fiber for $\lambda = 1550$ nm

Dispersion and Nonlinear Parameters	SPW $T_p = 200$ fs	SPW $T_p = 10$ ps	Optical Fiber $T_p = 200$ fs
L_D	~1 cm	~25 m	~2 m
L'_D	~1 cm	~2.5 km	~80 m
L_{NL} at $P_0 = 0.2$ W	~8 mm	~8 mm	~2 km
γ (m^{-1} W^{-1})	$\sim 6 \times 10^2$	$\sim 6 \times 10^2$	$\sim 3 \times 10^{-3}$

$=0.2$ W, $L_{NL} \approx 8$ mm. Consequently, near or above $P_0 \approx 0.2$ W, the GVD, TOD, and SPM all become relevant to the overall pulse dynamics. Note that β_3, which yields L_D', is extracted from the data of [73] and is described below.

An examination of Table 1 shows the sharp differences between pulse propagation in optical fibers and in SPWs. First, SPWs have dispersion lengths L_D and L_D' that are 2 orders of magnitude shorter than those for optical fibers. Also, the nonlinear length of a wire waveguide is several orders of magnitude shorter than in optical fibers, for a typical peak power of a few tenths of 1 W. The short nonlinear length is due to the very high nonlinear parameter, γ, which is approximately 10^5 higher in SPWs than in typical standard optical fibers. In addition, dispersion lengths are also pulse-length dependent. Thus the dispersion length for a typical picosecond pulse is several orders of magnitude longer than that for a femtosecond pulse. However, the nonlinear length is the same for both short and long pulses as long as the pulse power is the same. Therefore, with ultrashort pulses, linear and nonlinear optical effects can be simultaneously observed if the dispersion length and nonlinear length are tuned to be comparable to the waveguide length.

Note also that, as might be expected from the strong dispersion dependence of the SPWs, γ strongly depends on the cross-section geometry at these deeply scaled dimensions. For example, for a fixed height of 220 nm, the various values of γ are 680, 566, and 463 $W^{-1}\,m^{-1}$ for waveguide widths of 360, 450, and 520 nm, respectively, using the measurements from [108] and neglecting the longitudinal electric field component; these values are comparable with the ones obtained by Koos *et al.* [125]. We note here that in a few of our previous papers a coding error led to our stating erroneously high values of γ; this was corrected in [37].

4.6. Higher-Order Linear and Nonlinear Optical Effects in Si Photonic Wires: Solitons and Wire Dispersion

As discussed in the previous subsection, when certain conditions are satisfied, the characteristic lengths associated with the linear or nonlinear optical effects in Si wires become comparable with the dispersion length, L_D, or the nonlinear length L_{NL}, and thus they can no longer be neglected. Two such important effects, which are discussed in this subsection, are TOD and pulse self-steepening. Both of these phenomena are important in fiber optics mode propagation, but both have different features in Si wires.

4.6a. Third-Order Dispersion Effects

TOD effects in SPWs have been recently investigated via theoretical [96] and experimental studies [73,80]. Thus, as the data in Table 1 suggest, for optical pulses with a temporal width of a few hundred femtoseconds, the characteristic lengths of the second-order dispersion and the TOD become comparable, $L_D \sim L_D'$, and therefore one expects that the TOD would have a significant influence in determining the evolution of ultrashort pulses upon propagation in SPWs. In particular, and as it is known from the dynamics of ultrashort pulses propagating in optical fibers [126–129], there are two interesting cases of the interaction of TOD and pulse propagation in a SPW. First, if the wavelength of the input pulse corresponds to a ZGVD point, i.e., $\beta_2 = 0$, part of the spectrum of the pulse will lie in the anomalous GVD region ($\beta_2 < 0$), whereas the

remaining pulse spectrum will be in the normal GVD domain ($\beta_2 > 0$). On propagation, the pulse will split into one or more solitons that propagate in the spectral region with anomalous GVD, while the section of the pulse belonging to the normal GVD region will form a dispersive wave. In the second case, the pulse is fully in the anomalous GVD domain. If the power of the pulse is larger than the threshold power necessary to form a soliton, one or more solitons are generated, and as they propagate under the influence of the TOD, they will resonantly emit radiation. The wavelength of this emission will be determined by the point at which the wave vectors of the soliton and the emitted dispersive wave are phase matched. There are important differences, however, between pulse propagation in Si wires and in optical fibers. As one example, photogeneration of free carriers in wires induces optical losses that depend nonlinearly on the peak power of the pulse, thus leading to a more complex and richer pulse dynamics. In addition, in wires, as indicated above, dispersive effects can be much greater in magnitude.

These effects can be illustrated by considering the propagation of ultrashort optical pulses in the presence of photogenerated free carriers, i.e., the system of coupled equations (23) and (15). Thus, consider the propagation of a hyperbolic-secant-shaped (sech-shaped) pulse with $T_0 = 100$ fs and peak power $P_0 = 6.5$ W, in a SPW with dimensions $h \times w = 220$ nm $\times 360$ nm, and assume that the pulse wavelength is $\lambda = 1500$ nm. Since for this wire waveguide the ZGVD wavelength is near 1550 nm, the input pulse lies in a spectral region with anomalous GVD (see Fig. 2). Furthermore, the calculated linear and nonlinear parameters of the waveguide at $\lambda = 1500$ nm are $\beta_2 = -4$ ps^2/m, $\beta_3 = -0.0915$ ps^3/m, and $\gamma = 446.5$ W^{-1} m^{-1}, so that $L_D = 2.5$ mm, $L_D' = 10.9$ mm, $L_{NL} = 0.34$ mm, and the soliton number $N_{soliton} = 2.7$.

Note that in order to separate the effects that are due to TPA and TPA-induced free carriers, three different scenarios are considered here; the pulse evolutions for both the time and the frequency domains of each of these cases are shown in Fig. 8. In the first case, presented in Fig. 8(a), TPA is ignored, and its resulting free-carrier density is set equal to zero; thus only the dynamics of the optical field interacting with the wire dielectric medium is considered. In the second scenario, shown in Fig. 8(b), TPA is also ignored; however, free carriers created via TPA are kept in the simulation, and thus the interactions between the optical field and the free carriers are fully accounted for. In the last scenario, shown in Fig. 8(c), the full-physics simulation is carried out, including the presence of both TPA and free carriers. These three simulations allow a ready comparison of these three cases to be made. As expected, when TPA and the generation of free carriers are neglected, the pulse dynamics are very similar to the pulse evolution on propagation in an optical fiber [126–129], albeit over far shorter distances. Specifically, after a propagation distance of ~ 1 mm, the input pulse splits into two solitons whose velocities are slightly larger than the group velocity of the input pulse. This behavior is in agreement with the predictions of a soliton perturbation theory based on the moment method [130], according to which the temporal position of a soliton changes linearly with the propagation distance, $T_s(z) = (\beta_3 / T_0^3)z$, when the soliton propagates under the influence of the TOD. Hence, for $\beta_3 < 0$, the TOD speeds up the soliton, as illustrated in Fig. 8(a). Moreover, Fig. 8(a) shows that after the splitting of the input pulse the emerging solitons emit radiation in a spectral range situated in the normal GVD spectral region, between 1670 and 1770 nm, which is also in agreement with previous theoretical results. In

Figure 8

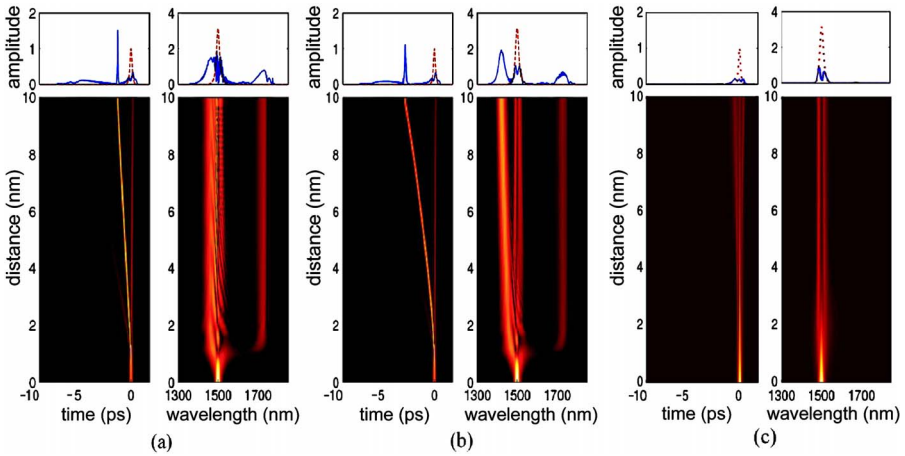

Propagation of a pulse with $T_0=100$ fs, peak power $P_0=6.5$ W, and pulse wavelength $\lambda=1500$ nm in a SPW with dimensions $h\times w=220$ nm $\times 360$ nm, for which the ZGVD wavelength $\lambda_0=1550$ nm, $\beta_2=-4$ ps^2/m, $\beta_3=-0.0915$ ps^3/m, and $\gamma=446.5$ W^{-1} m^{-1}. (a) Influences of the TPA and free carriers are neglected; (b) influence of TPA is ignored while free carriers effects are included; (c) both TPA and free carriers are fully accounted for.

particular, it has been previously shown that solitons propagating under the influence of the TOD emit radiation at a frequency that is shifted from the soliton's frequency by $\delta\omega=3|\beta_2|/\beta_3$, namely, at the frequency at which the wave vectors of the soliton and the dispersive wave are phase matched. Since the soliton with larger peak power propagates at $\lambda\sim 1470$ nm, and factoring in the corresponding shift in β_2, determined by the fact that the emerging solitons propagate at a wavelength that is different from the wavelength of the input pulse, this relation predicts that the wavelength of the emitted radiation is $\lambda\sim 1750$ nm, which is in good agreement with the numerical simulations.

When the effects of the free carriers are incorporated into the simulation (the second scenario), the pulse evolution changes in several important aspects, as shown in Fig. 8(b). Thus, in the temporal domain, the soliton with larger peak power is accelerated, and its temporal position is shifted toward the front of the pulse. In addition, in the spectral domain, this same soliton is shifted toward the blue side of the spectrum. On the other hand, the dynamics of the soliton carrying lower optical power remains essentially unchanged. These characteristics of the pulse evolution can be explained if one considers the nonlinear losses induced by the generation of free carriers via TPA. Thus, Eqs. (23) and (15) show that these optical losses are proportional to $\int_{-\infty}^{t}|u(z,t')|^4dt'$, which means that the optical loss at the front of the pulse is smaller than the loss in its tail. Since the soliton propagates in the anomalous GVD region, the redshifted frequency components move slower than the blueshifted ones. Therefore, the redshifted components are absorbed more fully in comparison with the blueshifted components, and thus the soliton is slowly shifted toward the blue side of the spectrum. In contrast, the soliton with smaller peak power induces a much smaller nonlinear loss, and therefore this effect is much weaker. This soliton probes chiefly the losses induced by the carriers generated by the larger soliton; these losses act merely as a constant loss

term in Eq. (23), and thus they do not affect the soliton dynamics. These results suggest that by tuning the density of the generated free carriers one can control the dynamics of optical solitons and, more generally, the temporal and the spectral characteristics of ultrashort optical pulses.

Finally to obtain a full understanding of pulse evolution in the vicinity of 1500 nm, it is necessary to include TPA, i.e., to solve the problem with the full set of simulation physics. This result is shown in Fig. 8(c). It is interesting that in this case the influence of the free carriers on the pulse dynamics, as was shown in the second scenario, is almost eliminated. This fact can be understood by realizing that the free-carrier effects in Fig. 8(b) require a high carrier density along the pulse propagation distance. This carrier density is determined dominantly by the local pump power along the waveguide axis. However, since in this last scenario the TPA reduces pump power, the carrier density drops dramatically as the pulse propagates along the axis. In addition, as the pulse energy is depleted and its power decreases below the threshold power required for forming a soliton, the pulse no longer propagates in the soliton regime, and therefore soliton effects such as emission of radiation are no longer observed. Note that the effects of TPA, carrier density, and nonlinearity vary as the input power and wavelength of the pump are changed. For example, carrier effects decrease dramatically as the pump wavelength reaches the TPA edge at $\lambda \sim 2214$ nm.

Deeper insight into the characteristics of the pulse evolution is provided by the pulse spectrogram $S(\omega, \tau)$, defined as the Fourier transform of the product between the output pulse and a delayed reference pulse, usually the input pulse. Mathematically, $S(\omega, \tau)$ is defined as

$$S(\omega, \tau) = \left| \int_{-\infty}^{\infty} u(z,t) u_{\mathrm{ref}}(t - \tau) e^{i\omega t} dt \right|. \tag{37}$$

The spectrograms, corresponding to the output pulses shown in Fig. 8, are also presented in Fig. 9. They clearly show the two solitons that are formed from the input pulse, as well as the emitted radiation; the latter appears as a pulse that is broad in both the frequency and the temporal domains. Furthermore, it can be seen that the soliton with larger peak power is shifted by an additional ~ 2 ps when the pulse propagates solely in the presence of the free carriers, whereas the temporal location of the soliton with a smaller peak power remains unchanged. In addition, through the mechanism just described, the former soliton undergoes a wavelength shift of about 50 nm. Moreover, these spectrograms show that in the presence of the free carriers, a smaller amount of radiation is emitted, an effect that is explained by the fact that as it propagates, the soliton shifts in the frequency domain and thus moves out of phase with the emitted radiation. Finally, with the TPA included, the effects induced by the presence of free carriers are washed out, and thus the soliton splitting in both the time and the frequency domains is very small. In a semiconductor wire it is in principle possible to introduce free carriers by nonoptical means such as carrier injection; in that case, intrinsic TPA could be avoided.

4.6b. Self-Steepening

Self-steepening represents one of the main factors that induce the reshaping of a short pulse as it propagates in a nonlinear optical medium. Its origin

Figure 9

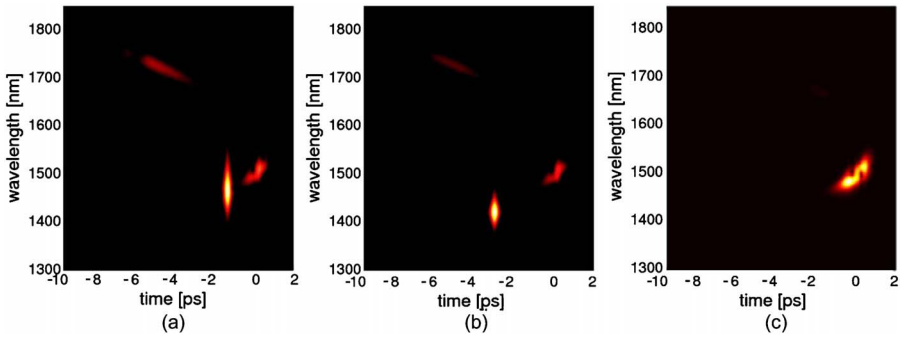

Spectrogram of a pulse with $T_0=100$ fs, peak power $P_0=6.5$ W, and pulse wavelength $\lambda=1500$ nm after it propagated a distance $z=10$ mm in a SPW with dimensions $h\times w=220$ nm $\times 360$ nm. The ZGVD wavelength $\lambda_0=1550$ nm, $\beta_2=-4$ ps^2/m, $\beta_3=-0.0915$ ps^3/m, and $\gamma=446.5$ W^{-1} m^{-1}. (a) Influences of the TPA and free carriers are neglected; (b) influence of TPA is ignored while the effects of the free carriers are included; (c) both TPA and free carriers are accounted for.

stems from the nonlinear dependence on the pulse peak power of the pulse group velocity [131,132]. Specifically, if the index of refraction of a nonlinear medium depends on the optical power, different temporal regions of a pulse probe a different index of refraction, and therefore the shift in the group velocity of the frequency components contained in the pulse depends on the local pulse power. As a result, the pulse is distorted as it propagates in the nonlinear medium, an effect that is stronger for spectrally broader pulses. This effect has been extensively investigated in the context of ultrashort pulse propagation in optical fibers [133,134], as it can be one of the main sources of signal degradation in optical communication systems.

These same self-steepening effects occur in SPWs. They can be investigated by modifying the equation describing the propagation of the optical field, Eq. (23), so as to incorporate the frequency dependence of the nonlinear coefficient of the waveguide. The modified model, written in a reference system moving with the pulse group velocity v_g, can be expressed as [135]

$$i\frac{\partial u}{\partial z}+\sum_{n\geq 2}\frac{i^n\beta_n}{n!}\frac{\partial^n u}{\partial t^n}=-i\frac{c\kappa}{2nv_g}(\alpha_{\mathrm{in}}+\alpha_{\mathrm{FC}})u-\frac{\omega_0\kappa}{nv_g}\delta n_{\mathrm{FC}}u \\ -\frac{3\omega_0 P_0\Gamma}{4\varepsilon_0 A_0 v_g^2}\left[1+i\left(\frac{1}{\omega_0}+\left.\frac{\partial\ln[g(\omega)]}{\partial\omega}\right|_{\omega=\omega_0}\right)\frac{\partial}{\partial t}\right]|u|^2u, \tag{38}$$

where ω_0 is the carrier frequency and $g(\omega)=\Gamma/v_g^2$. The strength of the self-steepening phenomena is determined by the characteristic shock time τ_s, defined as $\tau_s=\partial\{\ln[g(\omega)]\}/\partial\omega|_{\omega=\omega_0}=\tau_0+\tau_{wm}$, where $\tau_0=1/\omega_0$ is related to the frequency-dependent response of the nonlinearity in a bulk crystal and $\tau_{wm}=\tau_r+i\tau_i$ quantifies the waveguide contribution including that due to $\chi^{(3)}(\omega)$. For optical fibers τ_{wm} can be neglected; however, in the case of PCF, τ_{wm} can be as large as 1 fs [136]. It is important that the linear frequency dispersion is

accurately described in Eq. (38) to **all-orders** in the Taylor expansion of $\beta(\omega)$. This rigorous description of the waveguide frequency dispersion is easily implemented in the numerical algorithm by simply replacing in the Fourier domain the sum $\Sigma_{n\geq 2}(i^n\beta_n/n!)\partial_t^n$ with $\beta(\omega)-\beta(\omega_0)-\beta_1(\omega)(\omega-\omega_0)$, with the propagation constant $\beta=\beta(\omega)$ being found numerically.

To quantify the magnitude of self-steepening effects in SPWs one should determine the characteristic shock time τ_s by calculating the frequency dispersion of $\ln[\gamma(\omega)]$. As a generic example, we consider one of the waveguides in Subsection 4.4, with dimensions $h\times w=220$ nm $\times 360$ nm, determine the dependence $\gamma(\omega)$ through the procedure discussed in this section, and then calculate τ_s by numerical differentiation; the results of this approach are summarized in Fig. 10. The most notable conclusion illustrated by this figure is that for SPW the shock time can be as large as 25 fs, that is, more than an order of magnitude larger than that in PCFs. It is especially large in the vicinity of the cutoff wavelength, primarily because close to this wavelength the waveguide mode becomes less confined in the Si core. In addition, unlike the case of optical fibers or PCFs, τ_s has a significant imaginary part, which stems from the frequency dispersion of the TPA of Si.

We use the simulation to illustrate the influence of self-steepening effects on the propagation of ultrashort optical pulses in SPWs. To make the example more straightforward we minimize any effects of TPA by considering a pump in the wavelength vicinity of 2.2 μm, the TPA edge of Si. We examine the evolution of a sech-shaped pulse, a typical pulse shape in nonlinear propagation problems. The use of the 2.0 μm wavelength region requires a waveguide with cross section $h\times w=300$ nm $\times 450$ nm; this cross section is chosen to cause the wire waveguide to have anomalous dispersion, along with a large shock time for this long-wavelength range. For the simulation, we chose the following parameters: $\lambda=1950$ nm, $T_0=100$ fs, and peak power $P_0=6$ W. For these pulse parameters, $\mathrm{Re}(\gamma)=426.5$ W^{-1} m^{-1}, $L_D=2.1$ mm, and thus $L_{\mathrm{NL}}=0.39$ mm, $\beta_2=-4.69$ ps^2/m, and the soliton number $N_{\mathrm{soliton}}=2.32$. The results, which are obtained by numerically integrating the system of equations (15) and (38), are presented in Fig. 11. Several of the features illustrated in

Figure 10

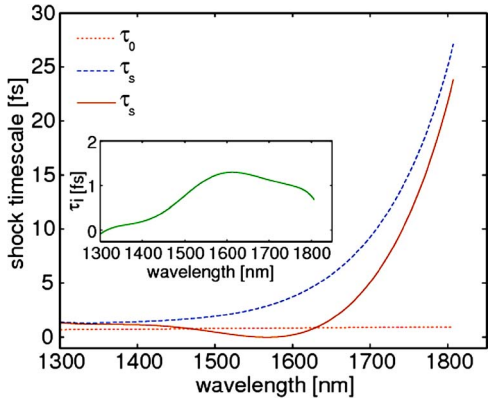

Real part of the parameter τ_s, calculated in two cases: dashed curve, the frequency dependence of $\chi^{(3)}$ is neglected; solid curve, the frequency dependence of $\chi^{(3)}$ is fully accounted for. Inset, imaginary part of τ_s versus λ.

Figure 11

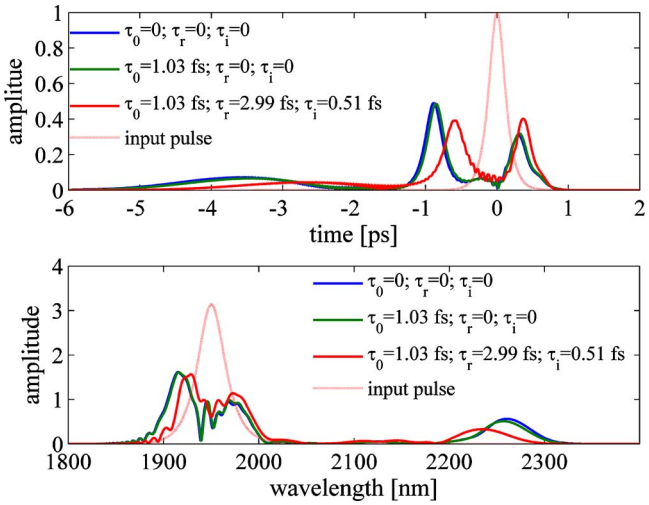

Temporal and spectral profiles of a pulse that propagates a distance $z=10$ mm in a SPW with dimensions $h\times w=300$ nm $\times 450$ nm.

this figure are also observed when only the effects of TOD were considered, that is, when the shock time was set to $\tau_s=0$. In the case of zero shock time, the pulse splits into two solitons, along with a subsequent emission of radiation. Moreover, the pulse dynamics changes only slightly if the shock time is chosen to be that corresponding to the bulk Si, $\tau_s=\tau_0$. However, the evolution of the input pulse is markedly changed when we include the contribution of the waveguide dispersion to τ_s; namely, in this case, the shift of the pulse, in both the temporal and the spectral domain, is reduced, which can be attributed to the imaginary part of τ_s. Thus, when τ_i is nonzero, Eq. (38) contains a term proportional to $u\partial|u|^2/\partial t$, a term that describes the intrapulse Raman scattering in optical fibers. As a result, this term has an effect similar to that of this fiber intrapulse Raman scattering, namely, it leads to a shift of the soliton spectrum toward longer wavelengths of the spectrum, and thus it cancels the blueshift induced by the free carriers. Note that this form of dynamics is unique to SPWs, since for optical fibers $\tau_i=0$, and no free carriers are generated. Note also that the response time for the TPA is much faster than for the Raman response ($\sim$3 ps), and therefore the Raman effect is not included in our simulations of propagation of femtosecond optical pulses.

These predictions are also corroborated by the pulse spectrogram $S(\omega,\tau)$ shown in Fig. 12. Thus, it can be seen that for $\tau_s=0$ and $\tau_s=\tau_0$ the pulse spectrograms are very similar to that corresponding to the case when only TOD was considered, which shows that for values of τ_s in this range the self-steepening effects are rather small. However, the pulse dynamics is strongly modified when the contribution of τ_{wm} is added to τ_s. In particular, and in agreement with the results presented in Fig. 11, in this case the time shift of the larger soliton is reduced to a subpicosecond value. In addition, a smaller amount of radiation is emitted by the generated solitons. Since the Raman effects for ultrashort pulses propagating in SPWs are negligible, these theoretical results show that, unlike the case of optical fibers or PCFs, self-steepening is the dominant higher-order nonlinear effect.

Figure 12

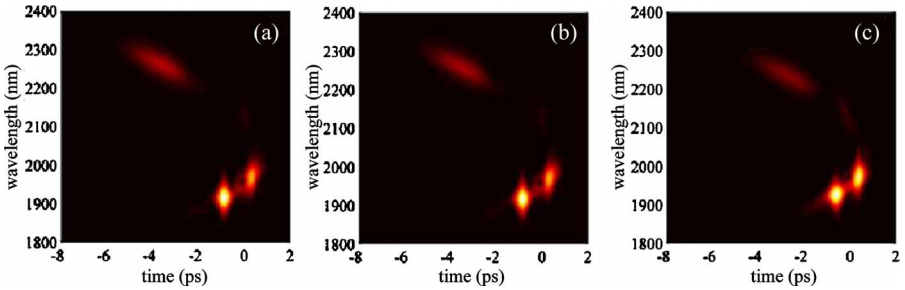

Pulse spectrograms calculated for the three cases shown in Fig. 9. (a) $\tau_0=0$ and $\tau_{wm}=0$ ($\tau_r=0$ and $\tau_i=0$); (b) $\tau_0=1.03$ fs and $\tau_{wm}=0$ ($\tau_r=0$ and $\tau_i=0$); (c) $\tau_0=1.03$ fs, $\tau_r=2.99$ fs, and $\tau_i=0.51$ fs. In all cases the propagation distance is $z=10$ mm.

5. Experimental Observations of Raman Amplification

One of the earliest nonlinear optical devices that emerged based on advances in confined Si-waveguide technology is the Raman laser. The interest in such a device or more specifically its closely related system, the Raman amplifier, is that it would allow for on-chip amplification rather than relying on a difficult-to-achieve set of ultralow-loss optical components in an on-chip photonics system. In this section, only Raman amplification in Si SPWs will be reviewed because of its importance for on-chip optical amplification.

5.1. Raman Amplification

The large Raman gain coefficient of Si ($\sim 10^4$ larger than that of silica) can, in principle, be used to achieve practical levels of gain with a diode-laser pump. In this connection, Claps *et al.* demonstrated spontaneous Raman emission [40], Raman amplification [42], and CARS [58]. In these studies, the authors used a rib waveguide structure that yielded a modal area of 5.4 μm^2, from which a signal amplification of 0.25 dB was observed with 1.6 W of coupled pump power [42]. These advances have continued in a series of impressive devices, which have dealt with a host of issues in Raman amplification, including undesired carrier photogeneration and on-chip resonator design.

A major issue in pulse Raman amplification is temporal beam walk off. Thus, because SPWs show large GVD, copropagating optical pulses separated by the Raman frequency ω_R can experience large temporal walk-off and therefore a small interaction length. As a result, the process of Raman amplification can be ineffective. There are several approaches that can overcome this problem. First, the waveguide is designed such that the pump and the Stokes signal correspond to different modes, which are designed such that, at the corresponding frequencies, the two pulses have the same group velocity [50]. Alternatively, taking advantage of the tunability of the frequency dispersion in SPWs, one can design such waveguides such that they possess a pair of

wavelengths situated on either side of a ZGVD point and, again separated by the Raman frequency ω_R, such they have the same group velocity [137].

Because the Raman effect is a nonlinear optical process, tighter optical confinement can lead to an increase in the efficiency of the process, which suggests that Si wires would make an effective gain medium. An example of a TE-polarized Raman amplifier using SPW made use of a pumping setup similar to Fig. 1. In the experiments using this device, the SPW was pumped with a continuous wave (CW) source at 1435 nm and injected with a counterpropagating signal beam centered at 1550 nm with a bandwidth of 40 nm. The SPW had a propagation loss of $\sim 3.6 \pm 0.1$ dB/cm at 1550 nm [84] with input and output coupling losses of $\sim 1.5-2$ dB/coupler. In this case the input pump power was 20.5 mW with an on–off gain of 0.4 dB. The power dependence of the gain exhibited a gain maximum at $\lambda = 1550.7$ nm, which corresponded to the predicted $\Delta\nu = 15.6$ THz (521 cm^{-1}) Raman shift in Si [40]. The measured on–off gain versus input pump power, i.e., that entering the waveguide, is shown in Fig. 13. The maximum gain was $G \sim 0.7$ dB (15%) for a pump power of $P_R \sim 29$ mW and for a waveguide length of $L = 4.2$ mm. The Raman amplifier figure of merit (FOM), which is defined as FOM $= G/(P_R L) = 57.47$ dB/cm/W, was substantial compared with early pulsed-format devices. Furthermore, this increase in the FOM showed that the gain scales approximately inversely with modal area. The data in Fig. 13 are approximately linear with a slope of 0.029 dB/mW.

The data gathered in this measurement can be compared with the results of a simple numerical solution of the stimulated Raman differential rate equations [101], *viz.*

$$\frac{dP_p(z)}{dz} = -\frac{\nu_p}{\nu_R} g_R P_p(z) P_R(z) - \alpha P_p(z) - \frac{\beta_{\text{TPA}}}{A_{\text{eff}}} P_p^2(z),$$

Figure 13

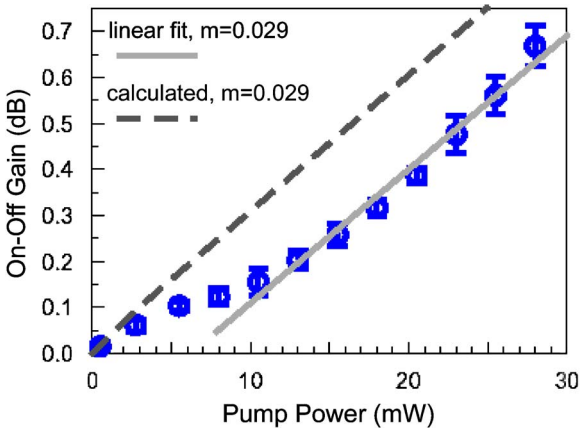

On–off gain versus input pump power. The maximum gain is 0.7 dB (17%) with a pump power of ~ 29 mW. A linear fit with a slope of 0.029 dB/mW corresponds to an SRS coefficient $g_R \sim 29$ cm/GW. From [43].

$$\frac{dP_R(z)}{dz} = \alpha P_R(z) - \frac{g_R - \beta_{\mathrm{TPA}}}{A_{\mathrm{eff}}} P_p(z) P_R(z), \tag{39}$$

where P_P and P_R are the pump and signal powers, respectively, ν_P and ν_R are the pump and signal frequencies, α=3.6 dB/cm is the propagation loss of the waveguide, β_{TPA}=0.44 cm/GW is the assumed TPA coefficient [42], A_{eff} =0.059 μm^2 is the effective modal area, and g_R=29 cm/GW is the stimulated Raman scattering coefficient. The solution to these equations takes into account the effective pump power that is due to the finite pump bandwidth, i.e., $P_{\mathrm{eff}}=P_p/(1+\Delta\nu_p/\Delta\nu_R)$, where $\Delta\nu_P$=160 GHz and $\Delta\nu_R$=105 GHz [42,113]. The effect of pump depletion, i.e., the coupling term in the first equation in Eqs. (39), was also accounted for in the calculation and was negligible in this case [43]. The calculated data, shown as a dashed line in Fig. 13, have a slope that matched the experimental data to within ±10%. The on–off gain and SRS coefficient found in this experiment agree well with the results of [42]. In this case the use of a deeply scaled down waveguide cross section of an SPW meant not only that the power is enhanced because of modal confinement but also that the transit time of the carriers is reduced compared with that in larger waveguides. In the experiment of [43], the effective recombination lifetime was found to have an upper bound of 0.77 ns.

5.2. Removal of Photogenerated Carriers

One of the major issues in Raman amplification as well as in many of the nonlinear optical devices discussed below is the generation of carriers by TPA, as these carriers can generate active absorption in the waveguide. This process becomes a particular problem as one shifts the pump wavelength to shorter wavelengths from, say, ~1700 nm. Free carriers can be eliminated either by recombination, as mentioned above, or by carrier sweep out through application of a transverse voltage.

The most obvious approach to reducing FCA is to use a pulsed Raman source, having a pulse repetition rate much less than that of the recombination time. In fact, many of the initial Raman amplification and Raman laser sources used this straightforward approach [40,42,44–48,51,52,54,123], which while of limited applicability for a practical high-data rate device, is useful to study the physics issues in a Raman amplifier or laser, including nonlinear loss mechanisms and carrier-lifetime effects. A second approach uses various approaches to decrease the recombination in the waveguide region. An excellent example is the use of He implantation to shorten lifetime [138]. In one experiment using this approach, He implantation with a 10^{12} cm^{-2} dose was made for a relatively large Si waveguide of cross section of 4.1 μm × 2.8 μm. Use of the He implantation formed recombination centers in the Si to reduce the free-carrier density and thus its power loss. As a result, the nonlinearity, as judged by SPM measurements, was increased. Recombination of carriers can also be enhanced by reducing the cross section of the gain region, since that allows more rapid recombination at the walls [124]. This approach is applicable to amplification in Si wires, which have the smallest possible waveguide cross section. In fact, this approach led to the first CW Raman devices, including that used in the CW amplifier example given above; it also plays an important role in reducing FCA in high-repetition-rate ultrafast lasers as long as the repetition rate is less than the recombination time. [47].

Carrier sweep out is the second approach for reducing carrier absorption; this topic has been the subject of numerous studies and has led to several ingenious device designs. For example, work in [139] showed that optical loss, due to FCA that was induced by TPA, may be significantly reduced by reverse biasing a p-i-n diode formed on the side regions on a rib waveguide. This biasing enabled the researchers to obtain higher CW Raman gain than when carriers were not removed, i.e., with no applied voltage, from the SOI waveguide, which was a 4.8 cm long waveguide with an effective core area of 1.6 μm^2. With carrier sweep out, the amplifier had a net CW Raman gain of >3 dB with an internal pump power of 700 mW.

A third approach has recently been proposed in mitigating the FCA effect by making use of a cladding-pumped geometry [140]. This configuration reduces the overlap of the pump beam with the Si core, thus weakening the effect of FCA. Consequently, the length of the amplifier may be made much longer, resulting in a higher total gain not possible in a direct core-pumped CW Raman amplifier. For example, numerical calculations assuming pump and Stokes wavelengths of 1220 and 1303 nm, respectively, show that total gains as high as 18 and 34 dB may be achieved with pump powers of 300 mW and 1 W, respectively, for Si-wire dimensions of $h \times w = 270\ \text{nm} \times 350\ \text{nm}$.

6. Observations of Optical Nonlinearities in Si Wires

The optical properties of Si wires are such that it is relatively easy to drive the wires into a strongly nonlinear regime with modest input power. As an example, at pump peak powers of ~ 1 W, corresponding to $\gamma P_0 \approx 22.5\ \text{cm}^{-1}$ in a 220 nm $\times$ 450 nm cross-section waveguide, intensities of $\sim 1\text{GW/cm}^2$ can be attained inside the waveguide. These intensities, in conjunction the extremely large $\chi^{(3)}$ of Si, are sufficient to readily observe all of the key nonlinear phenomena in optical fiber. In this section, the experimental observation of each of the principal nonlinear optical effects are discussed, including optical limiting, SPM and XPM, soliton generation, and MI.

6.1. Optical Limiting

Optical transmission limiting, or simply "optical limiting," is a readily observable nonlinear response in tightly confined SPWs. For ultrashort (femtosecond) pulses, the origin of the phenomena is dominantly TPA, although depending on the pulse length other effects such as free-carrier generation or SPM can influence the effect to a greater or lesser degree. An example of typical data is shown in Fig. 14. In this figure, two examples [72,73] are chosen to illustrate limiting in different but important temporal regimes. Specifically, the graph shows results corresponding to a train of 1.8 ps and 200 fs pulses, injected into waveguides of nearly identical cross sections, i.e., 220 nm $\times$ 450 nm, so as to have the same time-averaged carrier lifetime. The waveguide response is different for these two pulse regimes; Fig. 14(a) shows picosecond-pulse pumping, a regime where GVD is minimal, so that the SPM is the main optical effect that affects the pulse propagation, and Fig. 14(b) shows ultrashort ($\sim$200 fs)-pulse pumping, where GVD becomes significant enough such that, in conjunction with the SPM, it severely distorts the temporal

Figure 14

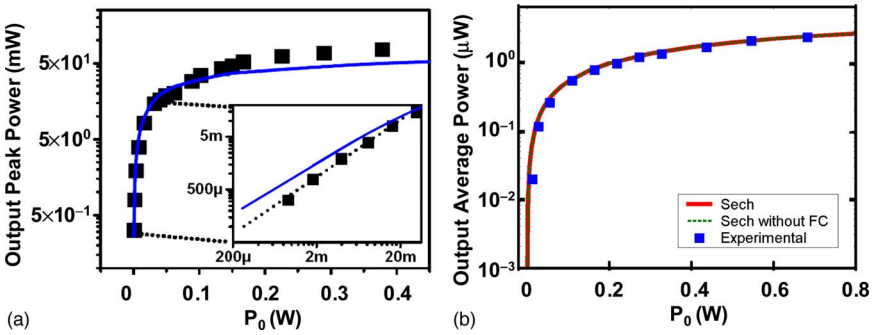

Dependence of output power on coupled input power for (a) 1.8 ps (from [72]) and (b) 200 fs pulses (from [73]). Experiment, squares; simulations, curves.

and spectral pulse profile as is shown in the next subsection. The maximum coupled-input peak powers for both cases are a few watts. However, for the case in Fig. 14(b), the simulations showed that the TOD effects are also sufficiently strong to significantly distort the output-pulse spectrum; thus in this case a better measure for the optical power carried by the pulse train is the average power. Consequently, Fig. 14(a) displays the output peak power versus the input peak power, while Fig. 14(b) displays average power versus input peak power.

For both cases, the output power scales linearly with the input power for input peak powers below ~50 mW and saturates above this input power. Although the powers required for achieving the onset of saturation are similar, the saturation mechanism for each case is different. For the case of the longer pulses, saturation occurs due to absorption from free carriers generated by TPA, while for the short pulses, saturation is due predominantly to direct optical loss through the TPA process itself. The onset of saturation in both cases is predicted accurately by the numerical solution of Eqs. (23) and (15), which is shown by the curves in each panel. In particular, this simulation predicts optical peak powers in the range ~50–100 mW, near the onset of saturation. The free-carrier-induced loss for the 1.8 ps case is approximately eight times that of the 200 fs case. In other words, owing to the difference in pulse duration for the two cases, the relative pulse energy is approximately 10:1 for the long pulse as compared with the short pulse; thus the longer pulse yields more carriers than the shorter pulse by an order of magnitude, as seen from Eq. (23), and therefore the corresponding free-carrier-induced losses are also larger.

The mechanism for the saturation behavior in each of the two cases was investigated in detail by numerically solving Eqs. (23) and (15). The solid curves in Fig. 14 denote the theoretical predictions for both cases. The calculation in this case takes into account the total dispersion and other linear effects, including FCA. For the case of the short-pulse pumping, the TPA process dominates and causes optical limiting at high peak powers. In contrast, for this low power, the photogenerated free-carrier-density is only $N \sim 3 \times 10^{15}$ cm^{-3}, which is comparable with the unexcited carrier density. Hence, the effect of losses from these TPA-generated carriers for the short-pulse pumping case is negligible. In fact, in this case, the numerical simulations were

done both in the presence and the absence of FCA, and, as expected, no difference was observed between these two cases as shown in Fig. 14(b). Our numerical calculations also showed that choosing sech- or Gaussian-shaped pulses leads to approximately the same results, as long as the FWHM is kept the same. For the case of picosecond pumping, shown in Fig. 14(a), near the saturation threshold power value of, say, ~60 mW, the optical power leads to a free-carrier density of $N \sim 2 \times 10^{17}$ cm^{-3}, which is about 2 orders of magnitude greater than the carrier density in the unexcited waveguide (p doped, $N \sim 1 \times 10^{15}$ cm^{-3}). Finally, note that the interpulse carrier accumulation from multiple pulses in either of the examples is negligible in our experiments, since the temporal separation between adjacent pulses is significantly longer than the carrier lifetime.

6.2. Self-Phase Modulation and Third-Order Dispersion

In addition to optical limiting behavior, optical pulses propagating in a SPW show increasing spectral modulation, as the pump power is increased. The origin of this process, which is well known in fiber optics, is shown clearly by Eq. (29) above (with the XPM term set to zero); the nonlinear response of the SPW causes the phase to shift in time during the pulse propagation, thus inducing a frequency shift. This effect is seen clearly in more exact numerical simulations, which show that as the input power is increased, the pulse spectrum broadens and then develops a multiple-peak structure. This behavior, which is a signature of the SPM, is the result of the phase interference between the pulse frequency components with a time-dependent SPM-induced frequency chirp. These simulations also clearly illustrate that the Si-wire SPM can be strongly influenced by the optical properties of the medium, including TPA, TPA-induced free carriers, and, for <1 ps pulses, TOD.

For typical pulsed-laser telecommunication sources, the short carrier lifetime in SPW does not allow interpulse carrier accumulation. However, the laser repetition rate can play an important role if the lifetime of the carriers is longer or comparable to the interpulse temporal separation, since in this case carrier accumulation may become a source of phase shift (as well as loss). Accumulation is particularly important in large-cross-section waveguides, i.e., $A_0 > 1$ μm^2, and if no applied voltage is present to sweep out photogenerated carriers.

Figure 15 illustrates the clear spectral broadening of picosecond and femtosecond pulses upon propagation in SPWs with approximately the same waveguide dimensions. In addition to broadening, the spectra in Fig. 15(b) exhibit strong spectral modulation and more pronounced asymmetry of the pulse profile than do the spectra in Fig 15(a). Both of these properties increase with input power. Spectral asymmetry, in general, may result from FCA, TOD, or the initial input-pulse asymmetry. In optical fibers, SPM-induced spectral broadening of picosecond pulses is normally symmetric around the center frequency [101]. Similarly, only minimal asymmetry is observed for propagation of such pulses in SPWs [72]. This situation is different for much larger Si waveguides, in which carrier lifetimes are longer and the resulting absorption by photogenerated FCA can cause spectral asymmetry [68]. However, as discussed above for the case of optical limiting experiments, while free-carrier generation can be a significant for picosecond or longer pulses, it is greatly reduced for femtosecond pulses because of the low pulse energy typically used.

Figure 15

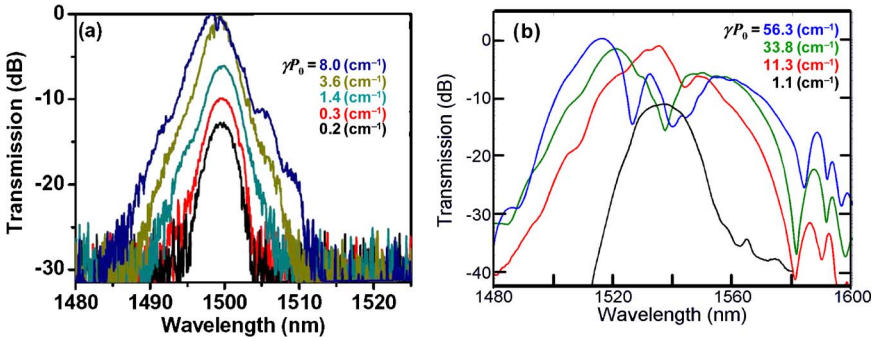

Self-phase modulation observed experimentally using picosecond and femtosecond pulses. (a) 1.8 ps pulses (figure from [72]) (b) 200 fs pulses (data from [73]).

In fact, in the case of the ~200 fs data in Fig. 15(b), simulations using the coupled-mode equations have shown clearly that TOD is the dominant effect leading to the spectral asymmetry seen in this figure.

The changes in the spectral features in Fig. 15(b) are to first order a result of the spectral modulation induced by SPM. The high nonlinearity of Si and its tight confinement in Si wires means that this modulation can be seen in SPWs with lower input power and many orders of magnitude shorter distance than in standard optical fibers. Of course, as mentioned above, effects such TPA and its resulting free-carrier generation further modify the otherwise pure SPM response of the Si wire—as does the influence of TOD in shorter pulses. Clearly, also, the spectral shape of the output pulse presents additional features, as compared with the input spectra. These changes can be accurately simulated with the coupled-wave equations. For example, Fig. 16 shows the experimental and simulation results obtained by using a sech pulse shape for

Figure 16

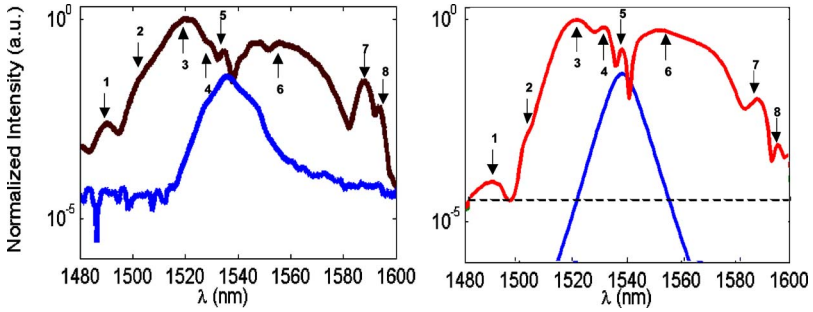

Comparison of simulation with experimental measurements of pulses propagating in a SPW waveguide with $\gamma P_0 = 56.3$ cm^{-1}. Left, measured spectra (brown). Right, simulation using sech input pulse (red). Blue curves on both panels correspond to $\gamma P_0 = 1.1$ cm^{-1} (with sech input pulse for simulation). Dashed line, OSA noise floor. The numbers illustrate features of the output spectrum common to experiment and simulation. From [73].

the 200 fs pulse; the numbers 1–8 indicate a series of smaller features or peaks. The agreement between data and simulations is excellent if a sech pulse shape is used. Simulation of the same data set using Gaussian-shaped input pulses gives less spectral features, but a more realistic imbalance between the left and right peaks.

6.3. Soliton Generation

In a nonlinear optical medium the generation of solitons is possible. These solitary optical waves are stationary states of propagation and are formed by an optical increase in the nonlinear index by a high-intensity propagating wave. Soliton formation requires that the guided-wave medium exhibit anomalous dispersion. They are potentially important as a communication format and are, in any case, a component essential to the full understanding of the nonlinear optics of a medium. Several experiments and optical simulation have shown that soliton radiation and its effects can be readily seen in SPWs. For example, the work of Hsieh *et al.* [73] matched the observation of soliton effects in SPWs with the results from numerical simulations. Recently, in a related measurement, Zhang *et al.* also observed related effects regarding soliton propagation in larger Si rib waveguides having dimensions of 400 nm $\times$ 860 nm and an etching depth of 300 nm [141]. In addition, in a recent theoretical study, the role of fission of higher-order solitons in Si waveguides in driving supercontinuum radiation [142] was discussed. More recently, Ding *et al.* reported measurements and simulations of soliton propagation from SPWs having three to four dispersion lengths [143].

As in optical fibers, radiation from solitons may be generated during the propagation of soliton pulses through the influence of higher-order perturbative effects, particularly TOD [126–129]. However, in the case of Si wires the effective nonlinear coefficient is $\sim 10^5$ larger than that in fibers, and thus soliton effects are seen in wires only millimeters in length. This radiation may be seen as a feature in the output spectrum of a propagating pulse in a SPW, exhibiting anomalous dispersion. For example, in addition to the features attributable to SPM in Fig. 16, an additional spectral feature is observed, which may be attributable to soliton radiation. The evolution of the spectra with power is shown in Fig. 17, which displays both experimental and numerical simulation results. This figure shows that as the input power increases, a spectral feature develops near 1590 nm for $\gamma P_0 = 45$ cm^{-1} (brown curve); notice that the peak is significantly shifted from the main SPM features. The soliton number for the conditions in Fig. 16 is $N_{\text{soliton}} = 6.6$, and thus pulse propagation is clearly in the soliton regime. Finally and characteristically, the location of this peak remains constant over a large range of powers, a behavior not seen in SPM features.

The location of this peak can also be used to determine the waveguide TOD coefficient—a technique similar to that first used to measure β_3 of optical fibers in the vicinity of the zero group-delay dispersion point [144]. In particular, by using the position of this spectral peak we can infer the value of β_3 by using the relation $\beta_3 = 3|\beta_2|T_0/\omega_r$, where ω_r is the normalized angular frequency **separation** between the center frequency and the soliton feature [126–129] (see also Subsection 4.6). Note that this relation does not account for the dependence of ω_r on dispersion coefficients beyond the third order, as well as any power dependence of the propagation constant; however these effects

Figure 17

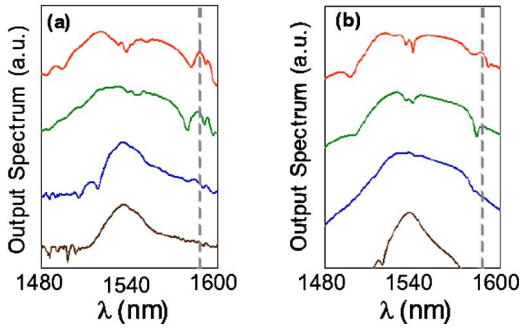

Change in output spectra due to SPM for different excitation levels $\gamma P_0 = 1.1$, 11.3, 33.8, 45.0 cm^{-1} (bottom to top) spectra for both (a) theory and (b) experiment. Note also the evolution of soliton radiation (dashed line) at 1590 nm.

are small and are commonly neglected. In addition, while this relation uses the pulse width T_0 in the expression for β_3, a more rigorous approach can be used in the case of multiple soliton generation. Thus, in this case, instead of T_0 one uses the temporal width of the corresponding emitted soliton. The central point, however, is that this approach can be used to probe waveguide properties such as TOD.

6.4. Cross-Phase Modulation

SPM alters the phase of an optical pulse as it propagates through the wire; it is therefore crucial to consider this effect when the optical peak power is large enough that the pulse propagation is in the nonlinear regime. In addition, in the cases where a second pulse is present, it is important to include the alteration of the phase of a pulse at one wavelength by a second, copropagating pulse, at a different wavelength, i.e., XPM. XPM is described by the general coupled-mode theory presented in the set of equations (27). Unlike in optical fibers, in Si wires the XPM process can be altered by the strong dispersion in a SPW and by the fact that TPA is present. These points will be discussed below.

Figure 18 illustrates the effect of XPM of a weak probe pulse by a pump pulse; these two pulses have different wavelengths and copropagate in the same waveguide [77]. The pump power corresponds to $\gamma_{ps} P_p = 10.4$ cm^{-1}, for several values of the pump–probe delay time. The pump and the probe or signal have center wavelengths at $\lambda_p = 1527$ nm and $\lambda_s = 1590$ nm, respectively. The pulse width and bandwidth of the resulting pulses are approximately 200 fs and 15 nm, respectively. The figure shows the dependence of the strength of XPM on the temporal overlap between the two pulses. These results illustrate clearly spectral variations in the probe spectrum, which can be induced by XPM. It was shown in [77] that as the nonlinearity-pump-power product increases, a larger number of oscillations are induced in the waveform, a result due to the increasing index change at higher pump powers. Similarly, as the pump overlap increases, the modulation of the signal by the pump as increases as shown in Fig. 18.

Figure 18

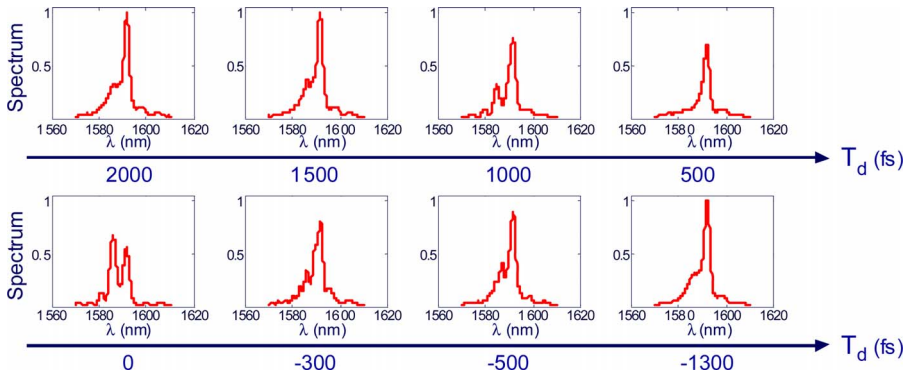

Demonstration of XPM in SPWs. Dependence of probe spectrum on pump power and pump–probe delay.

One approach to examining the physics of XPM is to examine the shift in wavelength of a signal pulse as the delay between pump and probe pulse, prior to injection into a waveguide, is varied. Since this delay controls the temporal profile of the refractive index change induced by the copropagating pump pulse, it maps out the wavelength change in the carrier frequency or wavelength [145] with power or index change. This shift can be described conveniently by the centroid wavelength of the spectrum, $\lambda_c = \int P(\lambda)\lambda\, d\lambda / \int P(\lambda)\, d\lambda$. The quantity λ_c shifts as the temporal delay between the pump and the probe pulses is varied. Figure 19 illustrates the shift in λ_c, that is, the nonlinear frequency shift of the centroid or mean wavelength, induced by changes in the pump–probe delay. This frequency shift was given above in Eq. (33) for the case of Gaussian pulses, $\delta\omega_s \propto -\{\exp[-(\tau-\tau_d+\delta)^2]-\exp[-(\tau-\tau_d)^2]\}$, where, again, τ, τ_d, and δ, are normalized time, normalized time delay, and temporal walk-off, respectively. For the waveguide length and pulse widths used in our experiments, the normalized temporal walk-off is $\delta = L\Delta / T_p = 4.78$ [77]. At

Figure 19

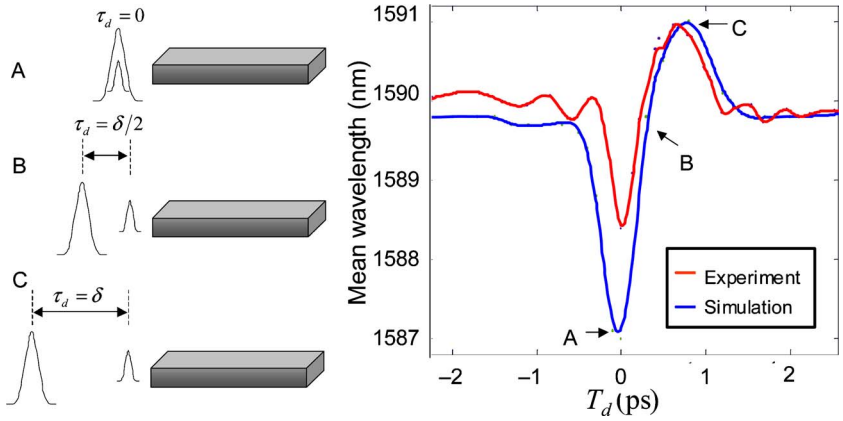

Experimental (red) and numerical simulation (blue) of the shift in center frequency due to XPM with the time delay of the pump and probe pulse. The center wavelength of the probe is ~1590 nm.

large absolute values of τ_d, no wavelength shift is observed because the two pulses do not overlap in the waveguide. On the other hand, if either $\tau_d=0$ or $\tau_d=\delta$, XPM interaction induces a large nonlinear wavelength shift, which for the data in Fig. 19 is >1 nm but is negative for $\tau_d=0$ and positive for $\tau_d=\delta$. However, in the vicinity of $\tau_d=\delta/2$, no shift is observed, since two shifts for the front and the rear of the waveguide effectively cancel each other. The asymmetry in the nonlinear shift of the probe centroid wavelength is explained by the presence of a small linear loss in the waveguide. Thus in the case in which $\tau_d=0$ the pump–probe interaction takes place mostly near the input facet of the waveguide, whereas when $\tau_d=\delta$ the pump interacts with the probe mostly near the output of the SPW, i.e., after the pump has lost part of its optical power because of intrinsic and TPA losses. In addition, the pulse width is also changed asymmetrically. Specifically, the peak near $\tau_d=0$ is narrower than the one near $\tau_d=\delta$, a behavior that is attributable to the slight temporal broadening of both the pump and the probe pulses because of frequency dispersion. Figure 19 also shows a fit to experimental results obtained by using the coupled-mode theory. The model accurately predicts the variation of shift with delay, as well as other more detailed features of the shift. For example, although the temporal broadening of the signal pulse with delay is small, the numerical simulation shown in Fig. 19 shows a small difference in the width of the two lobes.

Finally, because of the large effective nonlinear coefficient for Si and the high confinement of SPW, the absolute value for the frequency shift can be large—even with a relatively modest pump. For example, Dekker *et al.* demonstrated XPM-induced wavelength shifts of as much as >10 nm, which are comparable with the spectral width of the input probe pulses [76]. These results suggest that a XPM-induced frequency shift could be employed for an ultrafast all-optical switch, which can be used to switch off pulses as short as a few hundred femtoseconds.

With regard to optical switching, the nonlinear switching properties of devices may be described in terms of the FOM, where $\mathrm{FOM}=n_2/\beta_{\mathrm{TPA}}\lambda$, which is used to quantify the nonlinear phase shift achieved over an effective absorption-limited length [146]. The FOM value is relatively independent of the dimensions of the waveguide; however, the operational value of the FOM is device specific; i.e., it depends on the switching mechanism. Thus the required nonlinear phase shift varies from π to 4π, corresponding to FOM values of 0.5–2. For bulk Si, FOM=0.37, which suggests that Si wires may not be ideal for certain forms of nonlinear optical switching components. For the Si wires, n_2 and β_{TPA} are strongly enhanced by the waveguide confinement properties. But because the enhancement to n_2 and β_{TPA} are comparable, the FOM does not change significantly from the bulk values. However, the extremely low pulse energy required for Si-wire devices is itself interesting and may justify utilizing the low FOM value of Si despite its associated performance penalty. Further, since in the case of XPM-based switches, the required FOM is decreased to half of the value corresponding to the SPM case, these switches may be even more attractive [77]. As a final point, because of the pronounced wavelength dependence of both n_2 and β_{TPA}, the FOM for SPW devices will increase substantially with wavelength until at $\sim$2200 nm the FOM is $\sim$4.4 [39].

The use of XPM [74] for switching has been demonstrated in waveguides of $\sim 2\,\mu$m in cross section, thus larger than typical Si wires. This work used a

Mach–Zehnder interferometric device with the two wavelengths separated by ~25 nm. In this experiment, switching was governed at picosecond and shorter times by Kerr nonlinearities and at longer times by index change due to TPA-induced free-carrier loss. The Kerr nonlinearity was important for powers up to the 40 W pulse peak power. However, as the peak power level increased, free-carrier effects became important. Such effects included distortion in the switching transient. Switching speeds due to free carriers were limited by the $\sim 1-10\ \mu$s recombination times, which are greater than a typical picosecond switch pulse. These carriers accumulate from pulse to pulse, when the recombination time is longer than the interpulse time scale. Despite the importance of free-carrier generation, it was found that it was possible to attain a Kerr phase shift of 180° at power levels lower than those, for which substantial free carrier generation occurs.

6.5. Parametric Processes: Frequency Mixing

A final class of basic nonlinear processes to review is that of parametric mixing. This process is an important optical functionality, since it includes basic operations such as frequency upconversion and downconversion and wideband amplification. It is also a process that for efficient operation requires phase matching, which can be achieved via control of the waveguide dispersive properties, and a strong Kerr nonlinearity. As a model example for this discussion, consider wavelength conversion by means of techniques such as FWM. This process is related to several other important third-order nonlinear optical processes such as CARS, parametric amplification, electric-field-induced second-harmonic generation, and third-harmonic generation.

FWM using Si photonics has been demonstrated and explored by many groups. For example, Fukuda *et al.* showed the possibility of FWM in Si waveguides for frequency conversion [61]. In this experiment, conventional FWM was used wherein two input beams at frequencies ω_1 and ω_2 interact in the Si waveguide to generate new output frequencies at $2\omega_1-\omega_2$ and $2\omega_2-\omega_1$. In this experiment there was little effort to engineer dispersion, and thus mixing was limited in tunable spectral bandwidth and in efficiency.

More complex FWM schemes can be used, which are less demanding in the control over Si-wire dispersion, that is, for a case in which the waveguide cross sections are fixed by considerations other than for the FWM process. Thus a more general FWM process is shown in Fig. 5(e) (first two panels), in which three beams of different wavelengths, for example, two pump laser beams ($p1$ and $p2$) and a signal laser beam (s), interact in a $\boldsymbol{\chi}^{(3)}$ medium to produce an output (o) idler beam. For the same pump and signal wavelengths, two wavelength-mixing processes are possible as seen in Fig. 5(e); hence two output idler beams are generated. The advantage of this more general scheme over the conventional FWM process is that the more general scheme allows for operation of the pump (control) laser wavelengths over a wider spectral bandwidth while keeping the phase mismatch minimal for efficient conversion. This scheme can be an important consideration in a strongly dispersive medium, such as a Si waveguide.

In addition, in certain FWM schemes, resonances may play a role in enhancing the nonlinear optical susceptibility, as in the case of CARS. Further, in this

case the relevant third-order susceptibility, $\chi^{(3)}$, is that for Raman interaction. Figure 5(c) illustrates the energy diagram for the CARS process wherein the photon energy difference between the pump and signal matches the phonon (Raman) energy. In such a process, two photons derived from the same pump laser (p) interact with the (Stokes) signal photon in the medium to produce an output photon whose angular frequency is given by $\omega_{\mathrm{CARS}}=2\omega_p-\omega_s$. By comparison with the electronic $\chi^{(3)}$ processes just described, CARS is more useful for larger waveguide experiments because of the stronger dispersion in SPWs. In addition, the electronic susceptibility $\chi^{(3)}$ is much weaker than the Raman susceptibility, $\chi_R^{(3)}$ by $\sim 1/44$ [27] owing to the presence of the resonant terms in the expression for the Raman susceptibility. In fact, FWM using CARS was one of the earlier wavelength conversion techniques demonstrated. In the initial demonstration of CARS, wavelength conversion was achieved in a 5.4 $\mu\mathrm{m}^2$ cross-section Si waveguide [58]. Wavelength conversion was achieved from $\omega_s=1542$ nm to $\omega_{\mathrm{CARS}}=1329$ nm by using a pump laser at $\omega_p=1427$ nm with a -50 dB efficiency corresponding to a phase mismatch of $|\Delta\beta|=27\ \mathrm{cm}^{-1}$.

In the case of a SPW, the applicability of CARS has some limitations despite the attraction of the tighter optical confinement afforded by such a small, tightly confined waveguide. However, in fact, waveguide dispersion dominates the modal dispersion, thus making it difficult to achieve efficient phase-matched conversion. For example, a typical SPW has a phase mismatch of $|\Delta\beta|\approx 600\ \mathrm{cm}^{-1}$ for the CARS process! In addition, for a fixed signal wavelength, λ_s, the CARS process is not tunable, since the resonance condition requires that $\omega_p-\omega_s=\omega_R$. Finally, despite the fact that the nonresonant electronic susceptibility $\chi^{(3)}$ is smaller than the Raman susceptibility at resonance, the decreased cross-sectional area of the waveguide compensates for the weaker electronic $\chi^{(3)}$.

Frequency mixing has been demonstrated in SPW waveguides by means of the above nonresonant, nondegenerate FWM scheme by using low-power, CW diode-laser sources, corresponding to the first two panels of Fig. 5(e) [60]. Relatively efficient mixing was observed despite the large phase mismatch imposed by strong waveguide dispersion. The experimental results, including conversion efficiency, agree well with theoretical calculations based on coupled-mode theory. Frequency tuning of the idler from $\sim$20 GHz to $>$100 GHz was demonstrated [60].

The physics of this process is shown clearly by this coupled-wave treatment. The energy conservation and phase-matching conditions of this conversion scheme are

$$\omega_{o\pm}=\omega_s\pm(\omega_{p1}-\omega_{p2}),$$

$$\Delta\beta=\Delta\beta_{o\pm}-[\beta_s\pm(\beta_{p1}-\beta_{p2})], \tag{40}$$

where $p1$, $p2$, s, and o correspond to the two pumps, signal, and output fields, respectively, and $\beta_i=n_{\mathrm{eff}}(\omega_i)\omega_i/c$, where n_{eff} is the effective refractive index. For the (+) configuration in Eq. (40), the propagation properties and the interchange of energy between these four fields within the waveguide are described by four nonlinear, coupled-mode differential equations [101]:

$$\frac{dE_{p1}}{dz}+\frac{1}{2}\alpha_{p1}E_{p1}=i\gamma_{p1}(|E_{p1}|^2+2|E_{p2}|^2+2|E_s|^2+2|E_o|^2)E_{p1}$$
$$+2i\gamma_{p1}E_s^*E_{p2}E_o\exp(i\Delta\beta z),$$

$$\frac{dE_{p2}}{dz}+\frac{1}{2}\alpha_{p2}E_{p2}=i\gamma_{p2}(|E_{p2}|^2+2|E_{p1}|^2+2|E_s|^2+2|E_o|^2)E_{p2}$$
$$+2i\gamma_{p2}E_{p1}E_sE_o^*\exp(-i\Delta\beta z),$$

$$\frac{dE_s}{dz}+\frac{1}{2}\alpha_sE_s=i\gamma_s(|E_s|^2+2|E_{p2}|^2+2|E_{p1}|^2+2|E_o|^2)E_s$$
$$+2i\gamma_sE_{p1}^*E_{p2}E_o\exp(i\Delta\beta z),$$

$$\frac{dE_o}{dz}+\frac{1}{2}\alpha_oE_o=i\gamma_o(|E_o|^2+2|E_{p1}|^2+2|E_s|^2+2|E_{p2}|^2)E_o+2i\gamma_oE_{p1}E_sE_{p2}^*$$
$$\times\exp(-i\Delta\beta z), \tag{41}$$

where α_i and γ_i are the propagation loss and the nonlinear coefficient, respectively, corresponding to wavelength λ_i. The parameter $n_2=4.5\times10^{-18}$ m^2/W [108], and $A_{\text{eff}}=0.06$ μm^2 is the effective modal area [41]. Since the nonlinear coefficient $\gamma_i\propto(A_{\text{eff}})^{-1}$, the FWM conversion efficiency should be enhanced as the cross-sectional area is decreased. The first, second to fourth, and fifth terms on the right-hand side of Eqs. (41) are due to SPM, XPM, and FWM interactions, respectively. The effects of TPA and TPA-induced FCA are neglected because of the low powers used in this experiment. For the case of the (+) configuration of Eqs. (40), the idler wavelength (λ_{o+}) and the corresponding phase mismatch, $\Delta\beta$, are shown in Fig. 20(a). Solving Eqs.

Figure 20

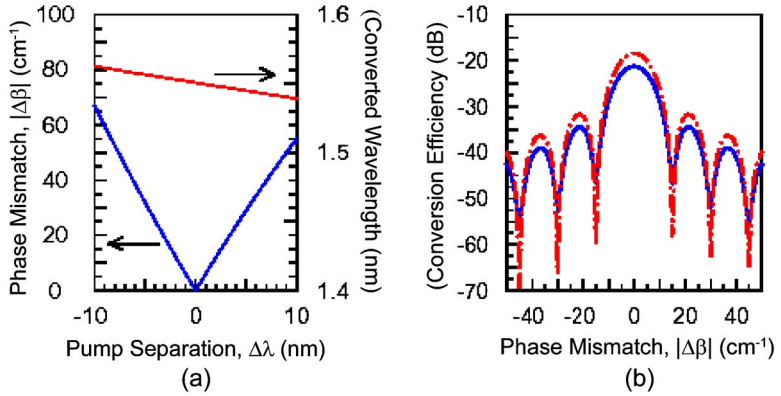

(a) Converted wavelength and phase mismatch versus pump–wavelength separation. (b) Conversion efficiency versus phase mismatch for $\Delta\lambda=0.148$ nm at two possible propagation losses of $\alpha=3.5$ dB/cm (solid curve) and 0.1 dB/cm (dashed-dotted curve). From [60].

(41) gives the conversion efficiency shown in Fig. 20(b). As an example, for pump wavelengths of $\lambda_{p1}=1435$ nm and $\lambda_{p2}=\lambda_{p1}+\Delta\lambda$, where $\Delta\lambda=0.148$ nm, a signal wavelength of $\lambda_s=1550.5$ nm, and the output wavelength of $\lambda_{o+}=1550.3$ nm, the phase mismatch is $|\Delta\beta|=0.6$ cm^{-1} and the conversion efficiency is −20 dB. The corresponding analysis for the (−) configuration yields similar results.

In addition, ultrabroadband parametric generation and wavelength conversion [66] have been examined for the case in which the pump beam is close to the zero dispersion wavelength of a SOI waveguide. Under strong long-pulse-width pumping, free-carrier effects were shown to affect the process; but with short pulses, i.e., <1 ns, FWM with a pulsed pump, the strong Kerr effect allowed efficient parametric amplification and wavelength conversion.

6.6. Tunability of Four-Wave Mixing

As is shown in Fig. 20 above, the efficiency of the FWM is set by the degree of phase matching among the interacting waves. We now consider the case of the FWM nonlinear optical interaction in Fig. 5(e) (third panel). To first order, the phase-matching condition involves ensuring that the wave vectors of the four interacting wave sum to zero, that is $\Delta k_{\mathrm{L}}\sim 0$, where $\Delta k_{\mathrm{L}}=2k_p-k_s-k_i$ is the linear phase mismatch and k_p, k_s, and k_i are the propagation wave vectors of the pump, signal, and idler beams, respectively. However, if any nonlinear changes in these wave vectors induced by SPM and XPM are included, the phase-matching condition must be modified to account for this variation. Thus for the case of a single degenerate pump, the phase mismatch Δk for a detuning $\Delta\omega$ between pump and signal is then

$$\Delta k_{\mathrm{NL}}=2\gamma P_p-\Delta k_{\mathrm{L}} \tag{42}$$

where γ is the effective nonlinearity, n_2 is the nonlinear refractive index, λ is the wavelength of light, A_{eff} is the mode area, and P_p is the pump power. This expression may be further corrected by including higher-order dispersion in the expression for the linear phase matching. Only even phase-matching terms must be included, since odd orders cancel out because of symmetry. Thus the first term that must be included is that of fourth-order dispersion; in this case, the linear phase mismatch is approximately

$$\Delta k_{\mathrm{L}}=-\beta_2(\Delta\omega)^2-\frac{1}{12}\beta_4(\Delta\omega)^4, \tag{43}$$

where the GVD coefficient β_2 and the fourth-order dispersion coefficient β_4 are calculated at the pump wavelength.

There are various definitions of conversion efficiency in use; one convenient definition equates the efficiency to the ratio of the idler output to the signal input, assuming conditions are such that there is essentially no TPA. Then the idler conversion efficiency $\eta_i=P_{\mathrm{out},i}/P_{\mathrm{in},s}$ is given by [147]

$$\eta_i=\left[\frac{\gamma P_p}{g}\sinh(gL)\right]^2, \tag{44}$$

where

$$g = \sqrt{\gamma P_p \Delta k_L - (\Delta k_L/2)^2} \tag{45}$$

is the parametric gain, $P_{out,i}$ is the idler output power, $P_{in,s}$ is the signal input power, and L is the interaction length. Since the maximum efficiency $\eta_{max,i}$ occurs when $\Delta k = 0$,

$$\eta_{max,i} = \sinh^2(\gamma P_p L). \tag{46}$$

Defining the conversion bandwidth as that when $|\Delta kL| < \pi$ [101] and assuming the small-gain limit $2\gamma P_p L \ll \pi$, the conversion bandwidth BW_{FWM} is then

$$BW_{FWM} \approx \sqrt{\frac{4\pi}{\beta_2 L}}. \tag{47}$$

Notice that this bandwidth depends solely on the waveguide dispersion. In addition, since for Si wires, γ is 5–6 orders of magnitude larger than for conventional single-mode fibers, much shorter conversion lengths are possible for comparable levels of efficiency [90,92,125]. These short lengths translate into higher conversion bandwidths for comparable values of β_2 for Si wires. For example, interaction lengths for significant conversion of 1 cm are possible even at modest input powers [100].

Using this FWM approach along with Si-wire waveguides, net on–off gain has been demonstrated over a 28 nm bandwidth [64]. Thus, Si wires with a 300 nm × 550 nm cross section, designed to have anomalous dispersion over a broad range of frequencies, were used to demonstrate wavelength conversion at ~1510 to 1590 nm, with a peak conversion efficiency of +5.2 dB. As expected, nonlinear TPA was found to be the major loss mechanism. A folded 17 mm waveguide was implemented to offset the nonlinear absorption, since this geometry allowed operating at lower pump power for a given level of gain. This 17 mm device had a 4.9 dB total on–off gain and 1.8 dB net gain.

An excellent example of using the dispersion engineering that is possible in Si wires is contained in [100], which examines in detail the effect of waveguide dispersion on the bandwidth of FWM and shows that very broad-bandwidth frequency conversion is possible with FWM. For example, by selecting a waveguide with low GVD, a demonstration was made of a conversion bandwidth of ~150 nm at a conversion efficiency of −9.6 dB, as well as tuning throughout the C band with a somewhat lower conversion bandwidth. Further it was also shown that for pumping close to the ZGVD point, the phase-matching bandwidth was set by fourth-order dispersion [148,149], and in that case, by careful phase matching in the presence of this higher-order dispersion, the signal could be wavelength shifted from 1477 to 1672 nm with an efficiency of −12 dB.

6.7. Free-Carrier Control

As in other nonlinear optical processes in Si-wires, TPA carrier generation can limit the efficiency and operating powers for FWM. However, by incorporating a p-i-n junction in a SOI waveguide, efficient FWM and, hence, wavelength conversion, have been demonstrated [150]. In this case, carriers were swept out by the junction electric field in the junction-insulating region after reverse biasing. The experiments used a Si-rib waveguide to achieve a wavelength

conversion efficiency of −8.5 dB in an 8 cm long waveguide at pump intensity 40 MW/cm^2. With this high wavelength conversion efficiency, high-speed optical data transfer between C-band channels was demonstrated. In particular, a 10 Gb/s pseudo-random-bit-sequence data rate was converted to a second wavelength channel with minimal waveform distortion and with an open eye diagram; in a subsequent study, it was demonstrated that the data transfer rate can be increased to 40 Gb/s [63]. The waveguides in this experiment were not designed for phase matching; however, they could be folded for longer interaction length because of their low bend loss and carrier sweep out, thus lowering the waveguide optical loss. Folding also, of course, allows greatly reducing the on-chip footprint. Experiments have been done for other devices types to demonstrate the efficacy of carrier sweep out; see, for example, the discussion of this approach in Subsection 5.2..

6.8. Modulation Instability

MI represents the unstable evolution (exponential growth) of a CW copropagating in a nonlinear medium, an effect that is caused by the nonlinear interaction between the propagating waves. In the context of nonlinear optics, MI has been studied extensively, particularly in regard to propagation of optical beams in optical fibers [151–156]. Since as a result of the MI certain spectral components grow exponentially, this nonlinear process can be viewed as providing gain at these particular frequencies, and therefore can have important applications. Note that in the case of a single beam, it is necessary for the medium to possess anomalous dispersion in order to have MI gain.

As in FWM, MI enables SPWs to provide tunable optical gain at one or more frequencies. Recently, Panoiu *et al.* investigated theoretically this all-optical modulation approach as a means to achieve strong optical gain in a millimeter-long SPW [137]. Specifically, their work demonstrated that two optical CW beams that copropagate in a SPW could generate a strong MI within a propagation distance of just a few millimeters. The gain of this process depends on the power of the optical waves; thus it can be optically tuned, and it reaches its maximum value when both waves experience anomalous GVD. Finally, note that, as a result of the MI, the optical waves develop deep subpicosecond modulation. This phenomenon can thus be used as the basis for an on-chip source of ultrashort optical pulses.

Two cases can be used to illustrate the optical physics for MI: case A, in which one wave propagates in the normal GVD region, and the other experiences anomalous GVD; and case B, in which both waves propagate in the anomalous GVD region. The SPW for each case has dimensions $h \times w = 220$ nm $\times 360$ nm, for which the ZGVD point is $\lambda_0 = 1550$ nm (this wavelength corresponds to a second ZGVD point not shown in Fig. 3).

For both case A and case B, the dynamics of the two optical waves propagating in the SPW are governed by system (27). The stability of these two optical waves is studied first by finding the steady-state (CW) solutions, i.e., z-independent solutions of this system of equations, and then by analyzing the linear dynamics of small perturbations of these solutions [101,151–156]. Thus, simple calculations show that, if we neglect the linear and nonlinear losses, the MI gain spectrum defined by $G(\Omega) = 2\,\mathrm{Im}[\Lambda(\Omega)]$ is determined by the equation

$$[(\Lambda - \Omega/v_{g,p})^2 - \rho_p][(\Lambda - \Omega/v_{g,s})^2 - \rho_s] = \eta\Omega^4, \quad (48)$$

where Ω and Λ are the frequency and the wave vector of the modulation, respectively, $\eta = 4\gamma_{ps}\gamma_{sp}\beta_{2p}\beta_{2s}P_pP_s$, $\rho_{p,s} = \beta_{2p,s}\Omega^2(\gamma_{p,s}P_{p,s} + \beta_{2p,s}\Omega^2/4)$, and the subscripts (p,s) refer to the pump and the signal waves, respectively.

Now consider the MI gain in each of the two cases introduced above. In case A, the pump beam propagates in the normal GVD region, $\lambda_p = 1625.3$ nm, whereas in case B it experiences anomalous GVD at $\lambda_p = 1400$ nm. In both cases the signal beam propagates in the anomalous GVD region, at $\lambda_s = 1450$ nm. In case A, the two wavelengths are selected so that the waves have the same group velocity, and thus there is no temporal walk-off, whereas in case B the walk-off parameter is $\Delta = |1/v_{g,p} - 1/v_{g,s}| = 86.3$ ps/m. Use of Eq. (48) enables the dependence of the gain spectra versus the pump power P_p (at a signal power $P_s = 200$ mW in case A and $P_s = 40$ mW in case B) to be determined. The results, presented in Fig. 21, show that in both cases the copropagating waves experience strong MI, with a bandwidth of the gain spectrum of 10 THz. For comparison, the Raman gain bandwidth of Si is much smaller, at approximately 0.1 THz [43]. As discussed in Subsection 6.6, a potentially comparable gain bandwidth is expected in broadband FWM when the guide has anomalous dispersion; in fact, gain bandwidths of a few terahertz have been demonstrated experimentally for FWM [64].

Although the powers P_p, P_s are smaller in case B, a larger MI gain is observed in this same case, namely, when both waves experience anomalous GVD. In addition, in both cases the MI gain is 10^2–10^3 times larger than the MI gain achievable in optical fibers, for similar values of the optical powers. This property arises from the fact that the γ parameters, which determine the strength of the MI gain, are much larger for SPWs as compared with those of optical fibers. In addition, the frequency corresponding to the maximum MI gain can be tuned by changing the power of the interacting waves.

7. Applications of Nonlinearities in Si Nanowires

Many applications of optical nonlinearities in Si nanowires have recently been demonstrated. In this review, we illustrate these applications with a few selected examples, which are representative of the range of possibilities for this ultracompact guided-wave medium.

Figure 21

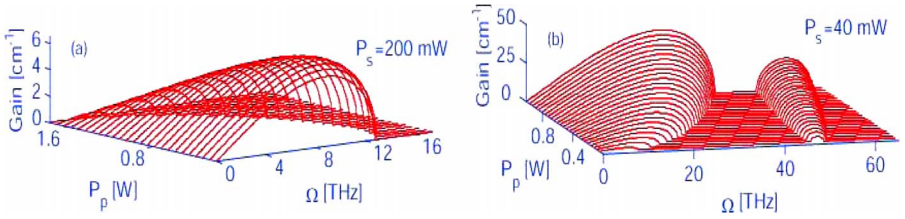

Calculated MI gain spectra for the two case of (a) normal and (b) anomalous dispersion described in the text.

7.1. Continuum Generation

Supercontinuum generation is a device functionality that has important applications in many areas of photonic integrated circuits [104], particularly WDM applications. In this application, for example, it is often beneficial to use a single broadband laser source, selected by filtering specific wavelength channels, and then modulate these channels, instead of using a separate laser to obtain each wavelength. In addition, continuum generation can be important for applications in sensing such as optical coherence tomography [157].

Previous studies have suggested that it is possible to achieve supercontinuum generation at low optical power and over short propagation distances provided that the guiding medium exhibits a strong nonlinear response and tunable dispersion properties. In the case of PCFs, the combination of control over the geometry of the core profile and lattice parameters and the large index difference between the silica core and air cladding provide dispersion tunability and a higher nonlinear response than is available in conventional fiber. In a typical PCF-based supercontinuum source, the effective mode area of the PCF is $\sim 1\ \mu m^2$, with a typical PCF length of the order of several meters [158]. Silica nanowires allow further dimensional reduction and the achievement of even higher effective optical nonlinearity [159].

A promising approach for an integrated continuum source is the use of Si waveguides and to an even greater extent SPWs [80], which offer greater confinement and hence high in-guide intensities even with modest input powers; e.g., 1 W of peak power yields 1 GW/cm^2 in the guide. This effect makes it reasonable to observe particularly efficient supercontinuum generation in these deeply scaled optical devices. Moreover, this efficiency can be greatly enhanced [104] if the wavelength of the input pulse is in the anomalous dispersion regime, near a ZGVD point; both of these dispersive properties are easily met in SPWs.

As a result of interest in potential applications, several groups have explored making continuum sources in Si wires or near-wire devices. For example, Yin *et al.* theoretically investigated the possibility of continuum generation in Si wires [142]. In a second example, a clear experimental demonstration of a tunable continuum source with a power-dependent broad spectrum was recently reported [80]. In this experiment spectral broadening of more than 350 nm, i.e., a 3/10 octave span, was observed upon propagation of ultrashort 1.3 μm wavelength optical pulses in a 4.7 mm long SPW waveguide. The waveguides were single-mode SPWs having a cross section of $A_0 = h \times w = 220$ nm $\times 520$ nw. The experiment also measured the wavelength dependence of the spectral features and related it to the waveguide dispersion and input power, and demonstrated tuning of the central wavelength of the continuum source.

Figure 22(a) shows the dependence of the output spectrum, from this experiment, as a function of the in-coupled peak pump power at a pump center wavelength of $\lambda = 1310$ nm. At the lowest observable pump power of $P_0 \sim 10$ mW, the spectral width was ~ 80 nm. As the pump power increased, the spectral width increased until at the highest power, 1 W, the spectral width had increased to more than 350 nm, as measured by the noise level of the detection system. This observation was a significant degree of spectral broadening, i.e., 3/10 of an octave, particularly since the pump pulse had propagated only $\sim 1/2$ cm in the wire waveguide; this broadening can be compared to the fact that in standard continuum sources a pulse with an optical

Figure 22

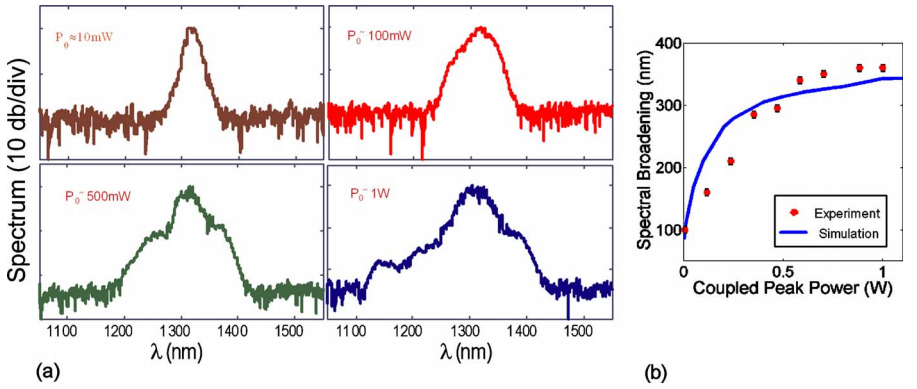

(a) Continuum generation in a 220 nm × 520 nm Si wire showing the pump-power dependence of the output spectra. At $P_0 \approx 1$ W the spectral broadening is 350 nm. (b) Spectral width as a function of coupled peak power. From [80].

intensity of 1 GW/cm^2 needs to propagate several meters in PCFs to achieve a comparable level of spectral broadening.

In Si with excitation at $\lambda < 1700$ nm, TPA plays an important role in determining the upper power limit for spectral broadening. In an approximate sense, TPA clamps the maximum propagating power in an optical waveguide, and thus it should inhibit spectral broadening above a certain level. This effect is seen in Fig. 22(b), which plots spectral width versus input power. Despite this clamping effect, the figure shows that significant broadening can be achieved prior to reaching power limiting due to TPA. Using coupled-wave simulation, which takes into account all nonlinear and dispersion effects including FCA, and using a sech-pulse input, the spectral broadening, defined by the 30 dB bandwidth, can be computed as a function of coupled peak power; this variation is shown by the blue line in Fig. 22(b). This plot shows a close match with the experimental values.

A measurement of the wavelength dependence of the output-pulse spectrum from ~1310 to 1570 nm provided insight into how the wavelength response of the waveguide affected continuum generation. For example, in this experiment, the output spectra showed that the broadening increased as the central wavelength λ_0 of the input pulse approached the ZGVD point of the wire. This behavior was attributed to the fact that near the ZGVD point, the linear dispersion was small and thus temporal pulse broadening was reduced; consequently, strong nonlinear interaction was maintained over a long propagation distance. It addition, it was found that the spectral features suggested the presence of TOD-induced spectral separation of solitons contained in the input pulse and the soliton-emitted radiation [142]. Finally, optical losses in the waveguide increased toward the short-wavelength range of the experiments and thus played a role in limiting the short-wavelength limit of the continuum radiation.

The origin of continuum or supercontinuum radiation in guided-wave structures has been a subject of much fundamental interest. Generally speaking, the strong spectral broadening seen in the process of generation of white

light (supercontinuum radiation) is attributable to the onset of (cascaded) nonlinear effects. The particular details of the evolution from the input-pulse to the output-pulse spectrum are strongly dependent on the specific pulse parameters, such as pulse width, pulse peak power, pulse chirp, and carrier frequency, as well as the linear and nonlinear optical properties of the corresponding optical medium [104]. In addition, higher-order-soliton fission [126,128,129,160,161] can be dominant in the initial stages of supercontinuum radiation generation. In fact, it is apparent that soliton effects, as recently observed in Si wires [73] and previously known to be important in fiber optics [101], can also serve as the source of significant spectral broadening. Clearly, dispersive effects are important in continuum generation. To increase the efficiency of the supercontinuum-generation process, input pulses may be launched near the ZGVD point so that the optical dispersion is small and thus minimizes temporal pulse broadening, which reduces the strength of the nonlinear effects. In the presence of dispersion, the sign of the GVD coefficient β_2 determines which phenomena are important for continuum generation. In the first case, when the pulse propagates in the **normal** dispersion regime, i.e., for $\beta_2 > 0$, the main nonlinear processes that contribute to the supercontinuum radiation are FWM, intrapulse Raman scattering, and, to a smaller extent, SPM and MI. However, in this normal dispersion regime, FWM processes have small efficiency at wavelengths far from the pump input [162] owing to the poor phase-matching characteristics and become even less efficient as the peak power increases. In addition, if femtosecond pulses are used, as was the case in the experiment just described, the Raman interaction in Si would be weak, as the characteristic Raman response time in Si is in the range of a few picoseconds. As a result, spectral broadening of pulses propagating in the normal dispersion regime is expected to be small. By contrast, for pulses propagating in the **anomalous** dispersion regime, $\beta_2 < 0$, both FWM and MI can be strongly phase matched, and thus both nonlinear optical processes become efficient in generating new optical frequencies.

7.2. Spectral Manipulation of Pulses Using Si Photonic Wires

One of the simplest applications of optical fibers is the use of their dispersive properties to vary the spectral and temporal content of guided-wave pulses. The classic application is the wide use of dispersion-shifted fiber to correct for pulse broadening in a fiber link [101]. This same approach has been used in self-mode-locked ring lasers [163]. More elaborate schemes can be used and in fact have recently attracted much interest because of the dispersion engineering possible in microstructured fiber [89].

Pulse temporal manipulation can also be accomplished with SPW, except in this case integration of the fiber is nearly impossible. Pulse compression functionality can be achieved in millimeter-long devices implemented in this SOI platform. Thus, recently, Chen *et al.* demonstrated theoretically for femtosecond pulses that dispersion engineering in conjunction with SPM and TOD can be used to achieve pulse compression [96]. In addition, Tien *et al.* experimentally demonstrated pulse compression in Si waveguides; although in this case the dispersion from photogenerated carriers was used to provide the necessary waveguide dispersive profile [164].

XPM can also provide an active optically controlled pulse-compression process. In this approach, a strong pump modifies the phase experienced by the

probe or signal beam and thus generates additional bandwidth that can support shorter pulses. Compression requires that the SPW exhibit anomalous dispersion at the probe wavelength. In addition, the pump–probe interaction length must be equal to or larger than the waveguide length. The first requirement implies that the group velocity of the two pulses is sufficiently close that the probe pulse interacts with the pump over the full length of the waveguide. In the process, the probe bandwidth is increased via XPM interaction with the pump and then is compressed temporally as the probe propagates in the anomalous GVD waveguide. These effects can be numerically simulated by using the coupled-mode model discussed above. In the example shown in Fig. 23, the waveguide is dispersion engineered such that the probe and the pump pulses have the same group velocity but have negative and positive GVDs, respectively. The figure shows that SPW enables compression in a relative short waveguide; that is, for a propagation length of just 0.8 mm the probe pulse yields compression by a factor of ~5.

7.3. Signal Regeneration Using Four-Wave Mixing

FWM has several immediate applications in data communications. These applications include amplification as mentioned above, as well as other more specific functions. The first of these is signal regeneration and reshaping [165]. This functionality requires that a nonlinear relation exist between input and converted data. Thus regeneration and reshaping has been successfully demonstrated by using semiconductor amplifiers and FWM in conventional and microstructured optical fiber [166–168]. However, as discussed above in this review, a nonlinear relation should of course also apply for the case of nonlinear optical processes in a SPW. In fact, nonlinear signal-timing improvement was demonstrated previously by using a simple Si photodetector based on TPA [169]. The attractive feature about using SPWs is the extremely large n_2 within this medium, and thus it is a very basic demonstration of fiber-on-a-chip functionality. Use of FWM as the means for accomplishing regeneration also means that ultrabroadband signals can be amplified by using a dispersion-engineered SPW.

Figure 23

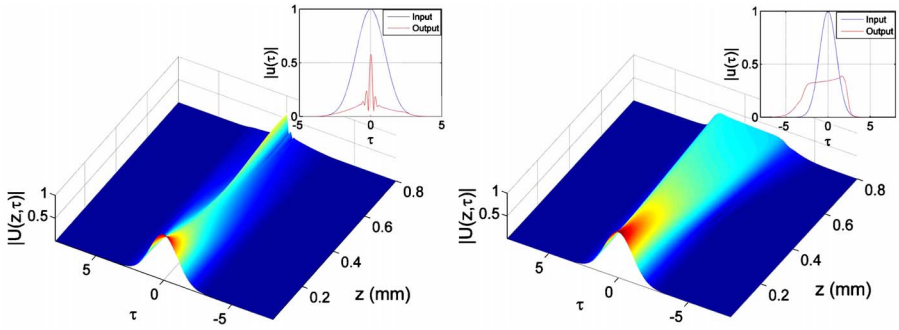

Simulation of pulse compression as a result of XPM in a $h \times w = 220$ nm $\times 360$ nm Si wire. Signal (left) and pump (right) field envelopes versus time and propagation distance. The temporal width is 200 fs for both the pump and the signal pulses. Here $\gamma_{ps} P_p \sim 100$ cm^{-1} for the pump, with a center frequency of 1625 nm. For the signal $P_s \ll P_p$, and its center frequency is 1451 nm. Insets, initial and final pulse envelopes. From [37].

There are several basic approaches to regeneration based on FWM, which involve interchanging the signal, pump, and idler between a CW source or clock and the input and converted data; these configurations are shown in Table 2. Note that certain of these configurations do not result in the required nonlinear transformation between signal and converted data and thus are not of interest. As an example, the most useful configuration for improving timing jitter is the last shown in the table, in which the "pump" is the clock, and the input data is the "signal." This approach was analyzed and experiments performed on a 1.8 cm length of a 300 nm × 500 nm cross-section SPW [165]. With this wire, the authors found a >2.2 reduction in the timing jitter of a gigabit per second, return-to-zero data stream using the last configuration. In addition, improvements in the extinction ratio and pulse reshaping were demonstrated by using the second and third configurations mentioned in Table 2. In the case of error recovery, a 4.3 dB improvement was measured in the same SPW and at the same data rate as just described. In this case, the input peak power levels were <100 mW to prevent saturation. Finally, in the case of reshaping, compensation for the pulse broadening incurred by propagation in a conventional fiber link by the SPW was demonstrated.

7.4. On-Chip Data Communication

The quality and compact dimensions of Si-wire photonic integrated circuits provide the technology for making on-chip and chip-to-chip SPW interconnection networks possible [170,171]. Optical transmission and WDM can allow high modulation rates and wavelength parallelism. This capability for reaching large bandwidth suggests that high-performance computing systems can now use integrated optics. However, designing such a network requires that the performance of such interconnects must be well known. Experiments have shown that low-loss Si-wire-waveguide technology has the linear and nonlinear optical performance for on-chip networks to carry ultrahigh-bandwidth WDM data streams. For example, one set of experiments has demonstrated low-error transmission of a 1.28 Tb/s stream through a 5 cm long wire waveguide, with the aggregate data rate, composed of 32 wavelengths, each modulated at 40 Gbits/s [172].

Table 2. Use of Four Wavelength Configurations Based on FWM Wavelength-Conversion Signal-Regeneration Schemes in a SPW for Three Wavelengths $\lambda_1, \lambda_2, \lambda_3$ Where $\lambda_1 < \lambda_2 < \lambda_3$[a]

Configuration	Pulse Reshaping	ER Improvement	Timing Jitter Reduction
A. Input data, CW source, converted data	✗	✗	✗
B. CW source, input data, converted data)	✓	✓	✗
C. Clock, input data, converted data	✓	✓	✓
D. Input data, clock, converted data	✓	✗	✓

[a]Schemes C and D are demonstrated by Salem *et al.* in [165]. Overall, scheme C is most effective; however, scheme D yields greater jitter reduction than scheme C. Table after that in [165].

The instrumentation for the bit error ratio (BER) measurements used 24 CW communications lasers with 100 GHz channel spacing and outputs combined by a 32-channel multiplexer. The detected signal was then evaluated at 10 Gbits/s with a communications signal analyzer and a BER tester. The signals were transmitted through a SPW, with dimensions $h \times w = 220$ nm $\times 520$ nm. The 5 cm wire required on-chip path length folding using 24 90° bends, each with a bending radius of 6.5 μm, to achieve the needed small footprint. Measurements of the output signals showed that in the 5 cm long dense WDM 10 Gbits/s per wavelength link, the wire exhibited only a 3.3 dB power penalty at a BER of 10^{-9}, or more generally, that a Si-wire can serve as a suitable on-chip data conduit.

7.5. Broadband Wavelength Conversion of High-Data-Rate Signals

Nonlinear optical conversion has many applications in telecommunications, and, as a result, a Si wavelength converter is a particularly useful device. To demonstrate the utility of Si-wire wavelength converters, systems measurements have been made of the data streams undergoing conversion. In one experiment [100], a 10 Gbit/s non-return-to-zero data train was converted across the C band from 1535 to 1566 nm with minimal degradation of the signal quality. This demonstration was accomplished by using the lowest-order TM mode of a 300 nm $\times$ 500 nm waveguide. The C-band tuning range was dictated by the Er-doped fiber amplifier bandwidth and not the FWM conversion bandwidth. Eye diagrams of the input signal (1535 nm) and the converted output (1566 nm) were measured by using a $2^{31}-1$ pseudo-random bit sequence and an input signal of −20 dBm. The time dependence of the optical losses such as FCA or thermal effects was sufficiently small that it caused only minimal degradation of the signal quality of the converted output, as was also observed in other experiments [63,65,150].

7.6. Raman Pulse Delay

Generation of tunable all-optical pulse delays is an important functionality for several types of photonic integrated circuit, including creating tunable on-chip optical dispersion. This approach has generally relied on the use of optical resonances that are available in optical cavities or photonic crystal structures, which have a very narrow wavelength response. Further, tuning of these structures is generally accomplished by relatively slow-response phenomena such as thermal changes in indices of refraction, and thus they have only a small temporal bandwidth.

Another approach uses the gain and line shape from stimulated Raman scattering in a Si wire to form an intensity-dependent delay structure, which can be tuned instantaneously [173]. This approach relies on the fact that the Raman-gain curve is related to the refractive index via the Kramers–Krönig relation. Further, the group index, which determines the speed of a signal pulse within a guided-wave structure, is related to the refractive index through the relation

$$n_g(\omega) = n(\omega) + \omega \frac{dn}{d\omega}. \tag{49}$$

The total Raman amplification experienced by a signal beam, that is, the ratio of the output signal power P_{out} to the input signal power P_{in}, is related to the gain parameter, G, via $P_{out}/P_{in}=e^{G}$. This Raman contribution to the gain causes a refractive index change as a function of wavelength. For example, at the Raman peak, the total delay ΔT_D of the signal pulse in passing through the material due to the presence of the pump field can be shown to be [173]

$$\Delta T_D = \frac{G}{\Gamma_R}, \tag{50}$$

where $G=g_R I_p L$ is the Raman gain parameter, I_p is the pump intensity, and L is the length of the interaction region. Because G depends linearly on the pump intensity, the delay can then also be tuned by varying the pump power.

With this approach, tunable optical pulse delays have been achieved by the gain available via stimulated Raman scattering [173] in an 8 mm long Si wire as shown in Fig. 24. In the case of the Raman line shape, the delay can be generated at any wavelength below the bandgap of Si and is widely tunable simply by changing the wavelength of the pump. In addition, the Si Raman linewidth has a bandwidth that can support a typical (~picosecond) telecommunication pulse. Group index changes of <0.15 may be used to generate <3 ps pulse delays. This method allows the delay of each pulse within a pulse train to be separately controlled for bandwidths of ≤ 100 GHz; a single waveguide can also be used to produce delays at different wavelength channels across the telecommunications spectrum. Last, the short interaction length and pump-power-dependent delay allows this scheme to have a fast reconfiguration time of ~ 70 GHz.

8. Conclusion

This review has discussed previous and current work on linear and nonlinear optical effects in Si photonic wires (SPWs), a field that is now growing rapidly because of the many compelling, new guided-wave optical phenomena and the many important emerging applications in nonlinear integrated Si photonics. In particular, many recent experimental and theoretical studies have demonstrated the intertwining of dispersion and optical nonlinearities with

Figure 24

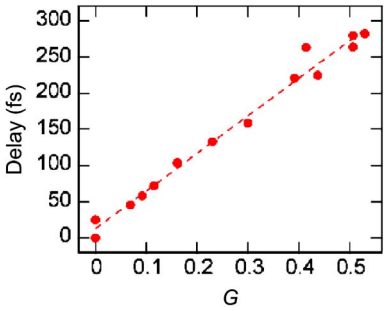

Data taken for SRS-induced delays. Measured delay versus the measured Raman gain parameter. From Okawachi *et al.* [173].

particular emphasis on self- and cross-phase modulation from picosecond to femtosecond pulses in Si wires. The theoretical component of this work is particularly important, since several physical properties of Si wires, such as the large index contrast, crystallinity, and tight optical confinement—which give rise to the potential for dispersion engineering and enhanced nonlinear optical effects—make the physics of propagation in Si wires distinct from those in optical fibers. As a consequence of engineering of this dispersion, photonic wires can be designed to operate as nonlinear devices and parametric mixers with gain over a wide range of group-velocity dispersion values at telecommunications wavelengths. More generally, by operating Si wires in a regime where the waveguide, characteristic dispersion, and nonlinear lengths are comparable with one another, it is possible to probe the complex interplay among dispersion and nonlinearity at low peak powers of the order of a few hundreds of milliwatts and with waveguide lengths of a few millimeters. In addition, the extremely small Si-wire cross-sectional dimension provides further scaling down of the length × power product required for nonlinear optical functionalities from that in standard integrated optics waveguides. This scale down arises from both the reduced area and the reduced group velocity of the optical waves. The low threshold powers for phase-changing effects and parametric functionality in SPWs make them potential candidates for various functional nonlinear optical devices in an integrated platform.

Appendix A: Acronym Glossary

BER = Bit-error ratio
BERT = Bit-error ratio tester
BOX = Buried oxide
CARS = Coherent anti-Stokes Raman scattering
CMOS = Complementary metal-oxide semiconductor
CSA = Communications signal analyzer
CW = Continuous wave
EDFA = Erbium-doped fiber amplifier
FC = Free carrier
FCA = Free-carrier absorption
FOM = Figure of merit
FWHM = Full width at half-maximum
FWM = Four-wave mixing
GVD = Group-velocity dispersion
HPCS = High-performance computing systems
MI = Modulation instability
NRZ = Non-return to zero
PCF = Photonic crystal fibers
PIC = Photonic integrated circuits
RZ = Return to zero
SMF = Single-mode fiber
SOI = Silicon on insulator
SPW = Silicon photonic wire
SRS = Stimulated Raman scattering
TE = Transverse electric

TM = Transverse magnetic
TOD = Third-order dispersion
TPA = Two-photon absorption
WDM = Wavelength division multiplexing
XPM = Cross-phase modulation
ZGVD = Zero group-velocity dispersion

Appendix B: Symbol Glossary

$\hat{\mathbf{a}}, \hat{\mathbf{b}}, \hat{\mathbf{c}}, \hat{\mathbf{d}}$ = Unit vectors
A, B = Sellmeier parameters
A_0 = Waveguide cross section
A_{eff} = Effective modal area
$\hat{\boldsymbol{\alpha}}$ = Polarizability tensor
$\alpha_{ij,\sigma}$ = Matrix elements of polarizability tensor
$\alpha, \alpha_{\text{in}}$ = Absorption coefficient
α_{FC} = Free-carrier absorption coefficient
BW_{FWM} = Conversion bandwidth speed of light
β = Mode propagation constant
β_1 = First-order dispersion coefficient
β_2 = Second-order dispersion coefficient
β_3 = Third-order dispersion coefficient
β_{TPA} = Two-photon absorption coefficient
$\beta_{\text{TPA},wg}$ = Effective two-photon absorption coefficient
$\boldsymbol{\chi}^{(3)}, \chi^{(3)}_{ijkl}$ = Third-order optical susceptibility
$\chi^{(n)}$ = n^{th}-order optical susceptibility
$\boldsymbol{\chi}^{R}$ = Raman susceptibility
D = Group-velocity dispersion coefficient
$\mathbf{D}$ = Electric displacement
δ = Normalized temporal walk-off
δn_{FC} = Free-carrier-induced change in the refractive index,
$\delta \mathbf{P}_{\text{L}}$ = Variation in the linear polarization
$\delta \varepsilon_{\text{L}}$ = Variation in the dielectric constant
$\delta \omega_s$ = Frequency shift
$\delta \omega$ = Relative soliton radiation shift
$\Delta \beta$ = Phase mismatch
Δk_{total} = Phase mismatch
ΔT_D = Total delay of signal pulse
$\Delta \omega$ = Raman linewidth
$\Delta \nu$ = Raman frequency shift
$\mathbf{E}$ = Electric field
$\mathbf{e}(\mathbf{r}_\perp, \omega)$ = Electric field of waveguide modes
E_{ig} = Indirect bandgap energy
ε = Dielectric constant
$\varepsilon(\mathbf{r}_\perp)$ = Transverse profile of the dielectric constant,
ε_0 = Vacuum permittivity
η_i = Idler conversion efficiency

$\eta_{max,i}$ = FWM maximum efficiency
g = Parametric gain
g_R = Stimulated Raman scattering coefficient
G = Gain parameter
$G(\Omega)$ = Modulation instability gain spectrum
γ_{ij} = Cross-phase modulation nonlinearity coefficient
γ_p = Pump nonlinearity coefficient
γ_s = Signal nonlinearity coefficient
Γ, Γ_i = Effective nonlinear optical waveguide susceptibility
Γ_{ij} = Effective cross-phase modulation waveguide susceptibility
Γ_R = Raman gain linewidth
h = Waveguide height width
$\mathbf{h}(\mathbf{r}_\perp, \omega)$ = Magnetic field of waveguide modes
$\mathbf{H}$ = Magnetic field
$\hbar$ = Reduced Planck's constant
k_p, k_s, k_i = Propagation constants of the pump, signal, and idler
κ = Modal overlap integral coefficient
L = Interaction length
L_D = Second-order dispersion length
$L_{D'}$ = Third-order dispersion length
L_{NL} = Nonlinear length
λ = Wavelength
λ_p = Pump wavelength
λ_s = Signal wavelength
λ_c = Average or mean wavelength
λ_{o+} = Four-wave mixing idler wavelength
Λ = Wave vector of the modulation instability process
m^*_{ce} = Electron effective mass
m^*_{ch} = Hole effective mass
m_0 = Electron mass
μ_e = Electron mobility
μ_h = Hole mobility
n = Index of refraction of Si
$n(\mathbf{r}_\perp)$ = Transverse profile of the refractive index
n_2 = Nonlinear refractive index, Kerr coefficient
$n_{2,\mathrm{wg}}$ = Waveguide effective nonlinear Kerr coefficient
n_{cladding} = Refractive index of cladding
n_{eff} = Effective index
n_g = Group index
N = Carrier density
N_{soliton} = Soliton number
ν_P = Pump frequency

ν_R = Raman signal frequency
ω = Photon angular frequency
$\omega_{0\pm}$ = Four-wave mixing idler output frequencies
ω_{CARS} = Coherent anti-Stokes Raman scattering signal frequency
ω_p = Pump angular frequency
ω_R = Raman frequency
ω_r = Normalized angular frequency separation
ω_s, = Stokes angular frequency or signal angular frequency
ω_σ = Raman mode frequency
$\varphi_s(z,T)$ = Nonlinear phase shift
$\mathbf{P}$ = Electric polarization
$P(z,t)$ = Position- and time-dependent waveguide power
P_0 = Input peak optical power
P_p = Input peak pump power
P_s = Input peak signal power
P_{eff} = Effective pump power
$P_{\mathrm{in},s}$ = Signal input power
$P_{\mathrm{out},i}$ = Idler output power
P_R = Raman signal power
$\mathbf{P}_{\mathrm{L}}$ = Linear polarization
$\mathbf{P}_{\mathrm{NL}}$ = Nonlinear polarization
$S(\omega,\tau)$ = Pulse spectrogram
t = Cladding thickness
T = Time in the reference frame of the pump pulse
t_c = Carrier lifetime
T_d = Temporal delay between two pulses
T_p, T_0 = Pulse width
τ_0 = Shock time due to bulk nonlinearity response
τ_d = Normalized time delay
τ_i = Imaginary part of τ_{wm}
τ_r = Real part of τ_{wm}
τ_s = Shock time
τ_{wm} = Shock time due to waveguide contribution
τ = Response time of Raman interaction
τ = Normalized time
$u(z,t)$ = Normalized field amplitude
$u_p(z,t)$ = Pump normalized field amplitude
$u_s(z,t)$ = Signal normalized field amplitude
v_g = Group velocity
$v_{g,s}$ = Signal group velocity
$v_{g,p}$ = Pump group velocity
w = Waveguide width
Z_0 = Impedance of the free space

Acknowledgments

This research was supported by the Air Force Office of Scientific Research (USAFOSR) Small Business Technology Transfer Program, contract FA9550-05-C-1954, and by AFOSR grant FA9550-05-1-0428. The IBM part of this work was supported by Office of Naval Research (ONR) /Defense Advanced Research Agency (DARPA) grant N00014-07-C-0105 ONR/DARPA.

References

1. L. O. Hocker, D. R. Sokoloff, V. Daneu, A. Szoke, and A. Javan, "Frequency mixing in infrared and far-infrared using a metal-to-metal point contact diode," Appl. Phys. Lett. **12**, 401–402 (1968).
2. R. M. Roth, N.-C. Panoiu, M. M. Adams, R. M. Osgood, Jr., C. C. Neacsu, and M. B. Raschke, "Resonant-plasmon field enhancement from asymmetrically illuminated conical metallic-probe tips," Opt. Express **14**, 2921–2931 (2006).
3. M. M. Fejer, G. A. Magel, D. H. Jundt, and R. L. Byer, "Quasi-phase-matched second harmonic generation: tuning and tolerances," IEEE J. Quantum Electron. **28**, 2631–2654 (1992).
4. X. Li, K. Terabe, H. Hatano, and K. Kitamura, "Nano-domain engineering in $LiNbO_3$ by focused ion beam," Jpn. J. Appl. Phys. Part 1 **44**, L1550–L1552 (2005).
5. A. Nahata, R. A. Linke, T. Ishi, and K. Ohashi, ″Enhanced nonlinear optical conversion from a periodically nanostructured metal film,″ Opt. Lett. **28**, 423–425 (2003).
6. M. Airola, Y. Liu, and S. J. Blair, "Second-harmonic generation from an array of sub-wavelength metal apertures," J. Opt. A **7**, S118–S123 (2005).
7. W. Fan, S. Zhang, N.-C. Panoiu, A. Abdenour, S. Krishna, R. M. Osgood, Jr., K. J. Malloy, and S. R. J. Brueck, "Second harmonic generation from a nanopatterned isotropic nonlinear material," Nano Lett. **6**, 1027–1030 (2006).
8. W. Fan, S. Zhang, K. J. Malloy, R. J. Brueck, N.-C. Panoiu, and R. M. Osgood, Jr., "Second harmonic generation from patterned GaAs inside a subwavelength metallic hole array," Opt. Express **14**, 9570–9575 (2006).
9. R. A. Soref and J. P. Lorenzo, "Single-crystal silicon: a new material for 1.3 and 1.6 μm integrated-optical components," Electron. Lett. **21**, 953–954 (1985).
10. R. A. Soref and B. R. Bennett, "Electro-optical effects in silicon," IEEE J. Quantum Electron. **QE-23**, 123–129 (1987).
11. A. Liu, R. Jones, L. Liao, D. Samara-Rubio, D. Rubin, O. Cohen, R. Nicolaescu, and M. Paniccia, "A high-speed silicon optical modulator based on a metal-oxide-semiconductor capacitor," Nature **427**, 615–618 (2004).
12. Q. Xu, B. Shmidt, S. Pradhan, and M. Lipson, "Micrometre-scale silicon electro-optic modulator," Nature **435**, 325–327 (2005).
13. V. R. Almeida, C. A. Barrios, R. Panepucci, and M. Lipson, "All-optical control of light on a silicon chip," Nature **431**, 1081–1084 (2004).

14. C. A. Barrios, V. R. de Almeida, and M. Lipson, "Low-power-consumption short-length and high-modulation-depth silicon electrooptic modulator," J. Lightwave Technol. **21**, 1089–1098 (2003).
15. G. Cocorullo, M. Iodice, I. Rendina, and P. M. Sarro, "Silicon thermooptic micromodulator with 700-kHz–3-dB bandwidth," IEEE Photon. Technol. Lett. **7**, 363–365 (1995).
16. R. L. Espinola, M.-C. Tsai, J. T. Yardley, and R. M. Osgood, Jr., "Fast and low-power thermooptic switch on thin silicon-on-insulator," IEEE Photon. Technol. Lett. **15**, 1366–1368 (2003).
17. M. Harjanne, M. Kapulainen, T. Aalto, and P. Heimala, "Sub-μs switching time in silicon-on-insulator Mach–Zehnder thermooptic switch," IEEE Photon. Technol. Lett. **16**, 2039–2041 (2004).
18. M. W. Geis, S. J. Spector, R. C. Williamson, and T. M. Lyszczarz, "Submicrosecond, submilliwatt, silicon-on-insulator thermooptic switch," IEEE Photon. Technol. Lett. **16**, 2514–2516 (2004).
19. Y. A. Vlasov, M. O'Boyle, H. F. Hamann, and S. J. McNab, "Active control of slow light on a chip with photonic crystal waveguides," Nature **438**, 65–69 (2005).
20. W. Bogaerts, R. Baets, P. Dumon, V. Wiaux, S. Beckx, D. Taillaert, B. Luyssaert, J. van Campenhout, P. Bienstman, and D. van Thourhout, "Nanophotonic waveguides in silicon-on-insulator fabricated with CMOS technology," J. Lightwave Technol. **23**, 401–412 (2005).
21. R. A. Soref, "Silicon-based optoelectronics," Proc. IEEE **81**, 1687–1706 (1993).
22. B. P. Pal, "Guided-wave optics on silicon: physics, technology and status," in *Progress in Optics, Volume XXXII*, E.Wolf, ed. (Elsevier, 1993), pp. 3–59.
23. G. T. Reed and A. P. Knights, *Silicon Photonics: an Introduction* (Wiley, 2004).
24. L. Pavesi and D. J. Lockwood, *Silicon Photonics* (Springer-Verlag, 2004).
25. M. Paniccia, M. Morse, and M. Salib, "Integrated photonics," Top. Appl. Phys. **94**, 51–88 (2004).
26. L. C. Kimerling, L. Dal Negro, S. Saini, Y. Yi, D. Ahn, S. Akiyama, D. Cannon, J. Liu, J. G. Sandland, D. Sparacin, J. Michel, K. Wada, and M. R. Watts, "Monolithic silicon microphotonics," Top. Appl. Phys. **94**, 89–120 (2004).
27. B. Jalali, R. Claps, D. Dimitropoulos, and V. Raghunathan, "Light generation, amplification, and wavelength conversion via stimulated Raman scattering in silicon microstructures," Top. Appl. Phys. **94**, 199–238 (2004).
28. R. J. Bozeat, S. Day, F. Hopper, F. P. Payne, S. W. Roberts, and M. Asghari, "Silicon based waveguides," Top. Appl. Phys. **94**, 269–294 (2004).
29. S. Janz, "Silicon-based waveguide technology for wavelength division multiplexing," Top. Appl. Phys. **94**, 323–360 (2004).
30. A. Irace, G. Breglio, M. Iodice, and A. Cutolo, "Light modulation with silicon devices," Top. Appl. Phys. **94**, 361–391 (2004).
31. M. Lipson, "Guiding, modulating, and emitting light on silicon—challenges and opportunities," J. Lightwave Technol. **23**, 4222–4238 (2005).
32. L. Pavesi and G. Guillot, *Optical Interconnects—the Silicon Approach* (Springer-Verlag, 2006).

33. B. Jalali and S. Fathpour, "Silicon photonics," J. Lightwave Technol. **24**, 4600–4615 (2006).
34. R. A. Soref, "The past, present, and future of silicon photonics," IEEE J. Sel. Top. Quantum Electron. **12**, 1678–1687 (2006).
35. P. Dumon, G. Priem, L. R. Nunes, W. Bogaerts, D. van Thourhout, P. Bienstman, T. K. Liang, M. Tsuchiya, P. Jaenen, S. Beckx, J. Wouters, and R. Baets, "Linear and nonlinear nanophotonic devices based on silicon-on-insulator wire waveguides," Jpn. J. Appl. Phys. Part 1 **45**, 6589–6602 (2006).
36. R. Dekker, N. Usechak, M. Först, and A. Driessen, "Ultrafast nonlinear all-optical processes in silicon-on-insulator waveguides," J. Phys. D **40**, R249–R271 (2007).
37. J. I. Dadap, N. C. Panoiu, X. Chen, I. Hsieh, X. Liu, C. Chou, E. Dulkeith, S. J. McNab, F. Xia, W. M. J. Green, L. Sekaric, Y. A. Vlasov, and R. M. Osgood, Jr., "Nonlinear-optical phase modification in dispersion-engineered Si photonic wires," Opt. Express **16**, 1280–1299 (2008).
38. M. A. Foster, A. C. Turner, M. Lipson, and A. L. Gaeta, "Nonlinear optics in photonic nanowires," Opt. Express **16**, 1300–1320 (2008).
39. Q. Lin, O. J. Painter, and G. P. Agrawal, "Nonlinear optical phenomena in silicon waveguides: modeling and applications," Opt. Express **15**, 16604–16644 (2007).
40. R. Claps, D. Dimitropoulos, Y. Han, and B. Jalali, "Observation of Raman emission in silicon waveguides at 1.54 μm," Opt. Express **10**, 1305–1313 (2002).
41. J. I. Dadap, R. L. Espinola, R. M. Osgood, Jr., S. J. McNab, and Y. A. Vlasov, "Spontaneous Raman scattering in ultrasmall silicon waveguides," Opt. Lett. **29**, 2755–2757 (2004).
42. R. Claps, D. Dimitropoulos, V. Raghunathan, Y. Han, and B. Jalali, "Observation of stimulated Raman amplification in silicon waveguides," Opt. Express **11**, 1731–1739 (2003).
43. R. Espinola, J. I. Dadap, R. M. Osgood, S. J. McNab, and Y. A. Vlasov, "Raman amplification in ultrasmall silicon-on-insulator wire waveguides," Opt. Express **12**, 3713–3718 (2004).
44. T. K. Liang and H. K. Tsang, "Efficient Raman amplification in silicon-on-insulator waveguides," Appl. Phys. Lett. **85**, 3343–3345 (2004).
45. A. Liu, H. Rong, M. Paniccia, O. Cohen, and D. Hak, "Net optical gain in a low loss silicon-on-insulator waveguide by stimulated Raman scattering," Opt. Express **12**, 4261–4268 (2004).
46. Ö. Boyraz and B. Jalali, "Demonstration of 11 dB fiber-to-fiber gain in a silicon Raman amplifier," IEICE Electron. Express **1**, 429–434 (2004).
47. Q. Xu, V. R. Almeida, and M. Lipson, "Demonstration of high Raman gain in a submicrometer-size silicon-on-insulator waveguide," Opt. Lett. **30**, 35–37 (2005).
48. R. Claps, V. Raghunathan, Ö. Boyraz, P. Koonath, D. Dimitropoulos, and B. Jalali, "Raman amplification and lasing in SiGe waveguides," Opt. Express **13**, 2459–2466 (2005).
49. S. G. Cloutier, P. A. Kossyrev, and J. Xu, "Optical gain and stimulated emission in periodic nanopatterned crystalline silicon," Nat. Mater. **4**, 887–891 (2005).
50. J. F. McMillan, X. Yang, N. C. Panoiu, R. M. Osgood, and C. W. Wong,

"Enhanced stimulated Raman scattering in slow-light photonic crystal waveguides," Opt. Lett. **31**, 1235–1237 (2006).
51. Ö. Boyraz and B. Jalali, "Demonstration of a silicon Raman laser," Opt. Express **12**, 5269–5273 (2004).
52. H. Rong, A. Liu, R. Jones, O. Cohen, D. Hak, R. Nicolaescu, A. Fang, and M. Paniccia, "An all-silicon Raman laser," Nature **433**, 292–294 (2005).
53. H. Rong, R. Jones, A. Liu, O. Cohen, D. Hak, A. Fang, and M. Paniccia, "A continuous-wave Raman silicon laser," Nature **433**, 725–728 (2005).
54. Ö. Boyraz and B. Jalali, "Demonstration of a directly modulated silicon Raman laser," Opt. Express **13**, 796–800 (2005).
55. H. Rong, Y.-H. Kuo, S. Xu, A. Liu, R. Jones, M. Paniccia, O. Cohen, and O. Raday, "Monolithic integrated Raman silicon laser," Opt. Express **14**, 6705–6712 (2006).
56. A. Polman, B. Min, J. Kalkman, T. J. Kippenberg, and K. J. Vahala, "Ultra-low threshold erbium-implanted toroidal microlaser on silicon," Appl. Phys. Lett. **84**, 1037–1039 (2004).
57. A. W. Fang, H. Park, O. Cohen, R. Jones, M. J. Paniccia, and J. E. Bowers, "Electrically pumped hybrid AlGaInAs–silicon evanescent laser," Opt. Express **14**, 9203–9210 (2006).
58. R. Claps, V. Raghunathan, D. Dimitropoulos, and B. Jalali, "Anti-Stokes Raman conversion in silicon waveguides," Opt. Express **11**, 2862–2872 (2003).
59. V. Raghunathan, R. Claps, D. Dimitropoulos, and B. Jalali, "Parametric Raman wavelength conversion in scaled silicon waveguides," J. Lightwave Technol. **23**, 2094–2102 (2005).
60. R. Espinola, J. Dadap, R. Osgood, Jr., S. McNab, and Y. Vlasov, "C-band wavelength conversion in silicon photonic wire waveguides," Opt. Express **13**, 4341–4349 (2005).
61. H. Fukuda, K. Yamada, T. Shoji, M. Takahashi, T. Tsuchizawa, T. Watanabe, J.-i. Takahashi, and S.-i. Itabashi, "Four-wave mixing in silicon wire waveguides," Opt. Express **13**, 4629–4637 (2005).
62. Q. Xu, V. R. Almeida, and M. Lipson, "Micrometer-scale all-optical wavelength converter on silicon," Opt. Lett. **30**, 2733–2735 (2005).
63. Y.-H. Kuo, H. Rong, V. Sih, S. Xu, M. Paniccia, and O. Cohen, "Demonstration of wavelength conversion at 40 Gb/s data rate in silicon waveguides," Opt. Express **14**, 11721–11726 (2006).
64. M. A. Foster, A. C. Turner, J. E. Sharping, B. S. Schmidt, M. Lipson, and A. L. Gaeta, "Broadband optical parametric gain on a silicon photonic chip," Nature **441**, 960–963 (2006).
65. K. Yamada, H. Fukuda, T. Tsuchizawa, T. Watanabe, T. Shoji, and S. Itabashi, "All-optical efficient wavelength conversion using silicon photonic wire waveguide," IEEE Photon. Technol. Lett. **18**, 1046–1048 (2006).
66. Q. Lin, J. Zhang, P. M. Fauchet, and G. P. Agrawal, "Ultrabroadband parametric generation and wavelength conversion in silicon waveguides," Opt. Express **14**, 4786–4799 (2006).
67. H. K. Tsang, C. S. Wong, T. K. Lang, I. E. Day, S. W. Roberts, A. Harpin, J. Drake, and M. Asghari, "Optical dispersion, two-photon absorption and self-phase modulation in silicon waveguides at 1.5 μm wavelength," Appl. Phys. Lett. **80**, 416–418 (2002).
68. G. W. Rieger, K. S. Virk, and J. F. Young, "Nonlinear propagation of

ultrafast 1.5 μm pulses in high-index-contrast silicon-on-insulator waveguides," Appl. Phys. Lett. **84**, 900–902 (2004).
69. Ö. Boyraz, T. Indukuri, and B. Jalali, "Self-phase modulation-induced spectral broadening in silicon waveguides," Opt. Express **12**, 829–834 (2004).
70. A. Cowan, G. Rieger, and J. Young, "Nonlinear transmission of 1.5 μm pulses through single-mode silicon-on-insulator waveguide structures," Opt. Express **12**, 1611–1621 (2004).
71. H. Yamada, M. Shirane, T. Chu, H. Yokoyama, S. Ishida, and Y. Arakawa, "Nonlinear-optic silicon-nanowire waveguides," Jpn. J. Appl. Phys., Part 1 **44**, 6541–6545 (2005).
72. E. Dulkeith, Y. A. Vlasov, X. Chen, N. C. Panoiu, and R. M. Osgood, Jr., "Self-phase-modulation in submicron silicon-on-insulator photonic wires," Opt. Express **14**, 5524–5534 (2006).
73. I.-W. Hsieh, X. Chen, J. I. Dadap, N. C. Panoiu, R. M. Osgood, S. J. McNab, and Y. A. Vlasov, "Ultrafast-pulse self-phase modulation and third-order dispersion in Si photonic wire-waveguides," Opt. Express **14**, 12380–12387 (2006).
74. Ö. Boyraz, P. Koonath, V. Raghunathan, and B. Jalali, "All optical switching and continuum generation in silicon waveguides," Opt. Express **12**, 4094–4102 (2004).
75. T. Liang, L. Nunes, T. Sakamoto, K. Sasagawa, T. Kawanishi, M. Tsuchiya, G. Priem, D. Van Thourhout, P. Dumon, R. Baets, and H. Tsang, "Ultrafast all-optical switching by cross-absorption modulation in silicon wire waveguides," Opt. Express **13**, 7298–7303 (2005).
76. R. Dekker, A. Driessen, T. Wahlbrink, C. Moormann, J. Niehusmann, and M. Först, "Ultrafast Kerr-induced all-optical wavelength conversion in silicon waveguides using 1.55 μm femtosecond pulses," Opt. Express **14**, 8336–8346 (2006).
77. I.-W. Hsieh, X. Chen, J. I. Dadap, N. C. Panoiu, R. M. Osgood, Jr., S. J. McNab, and Y. A. Vlasov, "Cross-phase modulation-induced spectral and temporal effects on co-propagating femtosecond pulses in silicon photonic wires," Opt. Express **15**, 1135–1146 (2007).
78. C. Manolatou and M. Lipson, "All-optical silicon modulators based on carrier injection by two-photon absorption," J. Lightwave Technol. **24**, 1433–1439 (2006).
79. T. K. Liang, L. R. Nunes, M. Tsuchiya, K. S. Abedin, T. Miyazaki, D. Van Thourhout, W. Bogaerts, P. Dumon, R. Baets, and H. K. Tsang, "High speed logic gate using two-photon absorption in silicon waveguides," Opt. Commun. **265**, 171–174 (2006).
80. I.-W. Hsieh, X. Chen, X. Liu, J. I. Dadap, N. C. Panoiu, C.-Y. Chou, F. Xia, W. M. Green, Y. A. Vlasov, and R. M. Osgood, "Supercontinuum generation in silicon photonic wires," Opt. Express **15**, 15242–15249 (2007).
81. R. W. Boyd, *Nonlinear Optics*, 2nd ed. (Academic, 2002).
82. R. Ahmad, F. Pizzuto, G. S. Camarda, R. L. Espinola, H. Rao, and R. M. Osgood, Jr., "Ultra-compact corner-mirrors and T-branches in silicon-on-insulator." IEEE Photon. Technol. Lett. **14**, 65–67 (2002).
83. S. McNab, N. Moll, and Y. A. Vlasov, "Ultra-low loss photonic integrated circuit with membrane-type photonic crystal waveguides," Opt. Express **11**, 2927–2939 (2003).
84. Y. Vlasov and S. McNab, "Losses in single-mode silicon-on-insulator

strip waveguides and bends," Opt. Express **12**, 1622–1631 (2004).
85. T. Shoji, T. Tsuchizawa, T. Watanabe, K. Yamada, and H. Morita, "Low loss mode size converter from 0.3 μm square Si wire waveguides to singlemode fibres," Electron. Lett. **38**, 1669–1670 (2002).
86. V. R. Almeida, R. R. Panepucci, and M. Lipson, "Nanotaper for compact mode conversion," Opt. Lett. **28**, 1302–1304 (2003).
87. F. Xia, L. Sekaric, and Y. A. Vlasov, "Ultracompact optical buffers on a silicon chip," Nat. Photonics **1**, 65–71 (2007).
88. C. G. Poulton, C. Koos, M. Fujii, A. Pfrang, T. Schimmel, J. Leuthold, and W. Freude, "Radiation modes and roughness loss in high index-contrast waveguides," IEEE J. Sel. Top. Quantum Electron. **12**, 1306–1321 (2006).
89. W. H. Reeves, D. V. Skryabin, F. Biancalana, J. C. Knight, P. S. J. Russell, F. G. Omenetto, A. Efimov, and A. J. Taylor, "Transformation and control of ultra-short pulses in dispersion-engineered photonic crystal fibers," Nature **424**, 511–515 (2003).
90. M. Foster, K. Moll, and A. Gaeta, "Optimal waveguide dimensions for nonlinear interactions," Opt. Express **12**, 2880–2887 (2004).
91. S. Ramachandran, "Dispersion-tailored few-mode fibers: a versatile platform for in-fiber photonic devices," J. Lightwave Technol. **23**, 3426–3443 (2005).
92. X. Chen, N. C. Panoiu, and R. M. Osgood, "Theory of Raman-mediated pulsed amplification in silicon-wire waveguides," IEEE J. Quantum Electron. **42**, 160–170 (2006).
93. E. Dulkeith, F. Xia, L. Schares, W. M. J. Green, and Y. A. Vlasov, "Group index and group velocity dispersion in silicon-on-insulator photonic wires," Opt. Express **14**, 3853–3863 (2006).
94. A. C. Turner, C. Manolatou, B. S. Schmidt, M. Lipson, M. A. Foster, J. E. Sharping, and A. L. Gaeta, "Tailored anomalous group-velocity dispersion in silicon channel waveguides," Opt. Express **14**, 4357–4362 (2006).
95. L. Yin, Q. Lin, and G. P. Agrawal, "Dispersion tailoring and soliton propagation in silicon waveguides," Opt. Lett. **31**, 1295–1297 (2006).
96. X. Chen, N. Panoiu, I. Hsieh, J. I. Dadap, and R. M. Osgood, Jr., "Third-order dispersion and ultrafast pulse propagation in silicon wire waveguides," IEEE Photon. Technol. Lett. **18**, 2617–2619 (2006).
97. X. Liu, W. M. J. Green, X. Chen, I-W. Hsieh, J. I. Dadap, Y. A. Vlasov, and R. M. Osgood, Jr., "Conformal dielectric overlayers for engineering dispersion and effective nonlinearity of silicon nanophotonic wires," Opt. Lett. **33**, 2889–2891 (2008).
98. W. M. J. Green, X. Liu, X. Chen, S. Assefa, R. M. Osgood, Jr., and Y. A. Vlasov, "Dispersion engineering of silicon nanophotonic wires using a thin film cladding," in *Conference on Lasers and Electro-Optics/Quantum Electronics and Laser Science Conference and Photonic Applications Systems Technologies*, OSA Technical Digest (CD) (Optical Society of America, 2008), paper CTuDD5.
99. E. D. Palik, *Handbook of Optical Constants of Solids* (Academic, 1998).
100. M. A. Foster, A. C. Turner, R. Salem, M. Lipson, and A. L. Gaeta, "Broad-band continuous-wave parametric wavelength conversion in silicon nanowaveguides," Opt. Express **15**, 12949–12958 (2007).
101. G. P. Agrawal, *Nonlinear Fiber Optics* (Academic, 2006).
102. I. P. Kaminow and T. L. Koch, *Optical Fiber Telecommunications IIIA*

(Academic, 1997).
103. J. Lou, L. Tong, and Z. Ye, "Dispersion shifts in optical nanowires with thin dielectric coatings," Opt. Express **14**, 6993–6998 (2006).
104. J. M. Dudley, G. Genty, and S. Coen, "Supercontinuum generation in photonic crystal fiber," Rev. Mod. Phys. **78**, 1135–1184 (2006).
105. J. M. Dudley, G. Genty, and B. J. Eggleton, "Harnessing and control of optical rogue waves in supercontinuum generation," Opt. Express **16**, 3644–3651 (2008).
106. K. K. Tsia, S. Fathpour, and B. Jalali, "Electrical control of parametric processes in silicon waveguides," Opt. Express **16**, 9838–9843 (2008).
107. J. Zhang, Q. Lin, G. Piredda, R. W. Boyd, G. P. Agrawal, and P. M. Fauchet, "Anisotropic nonlinear response of silicon in the near-infrared region," Appl. Phys. Lett. **91**, 071113 (2007).
108. M. Dinu, F. Quochi, and H. Garcia, "Third-order nonlinearities in silicon at telecom wavelengths," Appl. Phys. Lett. **82**, 2954 (2003).
109. M. Dinu, "Dispersion of phonon-assisted nonresonant third-order nonlinearities," IEEE J. Quantum Electron. **39**, 1498–1503 (2003).
110. A. D. Bristow, N. Rotenberg, and H. M. van Driel, "Two-photon absorption and Kerr coefficients of silicon for 850–2200 nm," Appl. Phys. Lett. **90**, 191104 (2007).
111. Q. Lin, J. Zhang, G. Piredda, R. W. Boyd, P. M. Fauchet, and G. P. Agrawal, "Dispersion of silicon nonlinearities in the near infrared region," Appl. Phys. Lett. **91**, 021111 (2007).
112. H. Garcia and R. Kalyanaraman, "Phonon-assisted two-photon absorption in the presence of a dc-field: the nonlinear Franz–Keldysh effect in indirect gap semiconductors," J. Phys. B **39**, 2737–2746 (2006).
113. P. A. Temple and C. E. Hathaway, "Multiphonon Raman spectrum of silicon," Phys. Rev. B **7**, 3685–3697 (1973).
114. Y. R. Shen and N. Bloembergen, "Theory of stimulated Brillouin and Raman scattering," Phys. Rev. **137**, A1787–A1805 (1965).
115. M. D. Levenson and N. Bloembergen, "Dispersion of the nonlinear susceptibility tensor in centrosymmetric media," Phys. Rev. B **10**, 4447–4464 (1974).
116. M. Cardona, "Resonance phenomena," in *Light Scattering in Solids II*, Vol. 50 of Topics in Applied Physics, M. Cardona and G. Guntherodt, eds. (Springer, 1982), Chap. 2.
117. H. Vogt, "Coherent and hyper-Raman techniques," in *Light Scattering in Solids II*, Vol. 50 of Topics in Applied Physics, M. Cardona and G. Guntherodt, eds. (Springer, 1982), Chap. 4.
118. R. Loudon, "The Raman effect in crystals," Adv. Phys. **50**, 813–864 (2001).
119. P. E. Barclay, K. Srinivasan, and O. Painter, "Nonlinear response of silicon photonic crystal microresonators excited via an integrated waveguide and fiber taper," Opt. Express **13**, 801–820 (2005).
120. A. W. Snyder and J. D. Love, *Optical Waveguide Theory* (Chapman & Hall, 1983).
121. M. J. Adams, S. Ritchie, and M. J. Robertson, "Optimum overlap of electric and optical fields in semiconductor waveguide devices," Appl. Phys. Lett. **48**, 820–822 (1986).
122. S. R. Giguere, L. Friedman, R. A. Soref, and J. P. Lorenzo, "Simulation studies of silicon electro-optic waveguide devices," J. Appl. Phys. **68**, 4964–4970 (1990).

123. T. K. Liang and H. K. Tsang, "Role of free carriers from two-photon absorption in Raman amplification in silicon-on-insulator waveguides," Appl. Phys. Lett. **84**, 2745–2747 (2004).
124. R. Claps, V. Raghunathan, D. Dimitropoulos, and B. Jalali, "Influence of nonlinear absorption on Raman amplification in Silicon waveguides," Opt. Express **12**, 2774–2780 (2004).
125. C. Koos, L. Jacome, C. Poulton, J. Leuthold, and W. Freude, "Nonlinear silicon-on-insulator waveguides for all optical signal processing," Opt. Express **15**, 5976–5990 (2007).
126. P. K. A. Wai, C. R. Menyuk, Y. C. Lee, and H. H. Chen, "Nonlinear pulse propagation in the neighborhood of the zero-dispersion wavelength of monomode optical fibers," Opt. Lett. **11**, 464–466 (1986).
127. P. K. A. Wai, C. R. Menyuk, Y. C. Lee, and H. H. Chen, "Soliton at the zero-group-dispersion wavelength of a single mode fiber," Opt. Lett. **12**, 628–630 (1987).
128. P. K. A. Wai, H. H. Chen, and Y. C. Lee, "Radiations by solitons at the zero group-dispersion wavelength of single-mode optical fibers," Phys. Rev. A **41**, 426–439 (1990).
129. N. Akhmediev and M. Karlsson, "Cherenkov radiation emitted by solitons in optical fibers," Phys. Rev. A **51**, 2602–2607 (1995).
130. J. Santhanam and G. P. Agrawal, "Raman-induced spectral shifts in optical fibers: general theory based on the moment method," Opt. Commun. **222**, 413–420 (2003).
131. L. A. Ostrovskii, "Propagation of wave packets and space-time self-focusing in a nonlinear medium," Sov. Phys. JETP **24**, 797 (1967).
132. D. Grischkowsky, E. Courtens, and J. A. Armstrong, "Observation of self-steepening of optical pulses with possible shock formation," Phys. Rev. Lett. **31**, 422–425 (1973).
133. N. Tzoar and M. Jain, "Self-phase modulation in long-geometry optical-waveguides," Phys. Rev. A **23**, 1266–1270 (1981).
134. E. A. Golovchenko, E. M. Dianov, A. M. Prokhorov, and V. N. Serkin, "Decay of optical solitons," JETP Lett. **42**, 87–91 (1985).
135. N. C. Panoiu, X. Liu, and R. M. Osgood, "Self-steepening of ultrashort pulses in Si photonic nanowires" to be submitted to Opt. Lett.
136. B. Kibler, J. M. Dudley, and S. Coen, "Supercontinuum generation and nonlinear pulse propagation in photonic crystal fiber: influence of the frequency-dependent effective mode area," Appl. Phys. B **81**, 337–342 (2005).
137. N. C. Panoiu, X. Chen, and R. M. Osgood, Jr., "Modulation instability in silicon photonic nanowires," Opt. Lett. **31**, 3609–3611 (2006).
138. Y. Liu and H. K. Tsang, "Nonlinear absorption and Raman gain in helium-ion-implanted silicon waveguides," Opt. Lett. **31**, 1714–1716 (2006).
139. R. Jones, H. Rong, A. Liu, A. Fang, M. Paniccia, D. Hak, and O. Cohen, "Net continuous wave optical gain in a low loss silicon-on-insulator waveguide by stimulated Raman scattering," Opt. Express **13**, 519–525 (2005).
140. M. Krause, H. Renner, S. Fathpour, B. Jalali, and E. Brinkmeyer, "Gain enhancement in cladding-pumped silicon raman amplifiers," IEEE J. Quantum Electron. **44**, 692–704 (2008).
141. J. Zhang, Q. Lin, G. Piredda, R. W. Boyd, G. P. Agrawal, and P. M.

Fauchet, "Optical solitons in a silicon waveguide," Opt. Express **15**, 7682–7688 (2007).
142. L. Yin and G. P. Agrawal, "Soliton fission and supercontinuum generation in silicon waveguides," Opt. Lett. **32**, 391–393 (2007).
143. L. Ding, C. Benton, A. V. Gorbach, L. Ding, W. J. Wadsworth, J. C. Knight, D. V. Skryabin, M. Gnan, M. Sorrel, and R. M. De La Rue, "Solitons and spectral broadening in long silicon-on-insulator photonic wires," Opt. Express **16**, 3310–3319 (2008).
144. P. F. Curley, C. Spielmann, T. Brabec, F. Krausz, E. Wintner, and A. J. Schmidt, "Operation of a femtosecond Ti:sapphire solitary laser in the vicinity of zero group-delay dispersion," Opt. Lett. **18**, 54–56 (1993).
145. P. L. Baldeck, R. R. Alfano, and G. P. Agrawal, "Induced-frequency shift of copropagating ultrafast optical pulses," Appl. Phys. Lett. **52**, 1939–1941 (1988).
146. K. W. DeLong, K. B. Rochford, and G. I. Stegeman, "Effect of two-photon absorption on all-optical guided wave devices," Appl. Phys. Lett. **55**, 1823–1825 (1989).
147. J. Hansryd, A. Andrekson, M. Westlund, J. Li, and P. Hedekvist, "Fiber-based optical parametric amplifiers and their applications," IEEE J. Sel. Top. Quantum Electron. **8**, 506–520 (2002).
148. J. D. Harvey, R. Leonhardt, S. Coen, G. K. L. Wong, J. C. Knight, W. J. Wadsworth, and P. St. J. Russell, "Scalar modulation instability in the normal dispersion regime by use of a photonic crystal fiber," Opt. Lett. **28**, 2225–2227 (2003).
149. T. V. Andersen, K. M. Hilligsoe, C. K. Nielsen, J. Thogersen, K. P. Hansen, S. R. Keidling, and J. J. Larsen, "Continuous-wave wavelength conversion in a photonic crystal fiber with two zero-dispersion wavelengths," Opt. Express **12**, 4113–4122 (2004).
150. H. Rong, Y.-H. Kuo, A. Liu, M. Paniccia, and O. Cohen, "High efficiency wavelength conversion of 10 Gb/s data in silicon waveguides," Opt. Express **14**, 1182–1188 (2006).
151. G. P. Agrawal, "Modulation instability induced by cross-phase modulation," Phys. Rev. Lett. **59**, 880–883 (1987).
152. J. E. Rothenberg, "Modulational instability for normal dispersion," Phys. Rev. A **42**, 682–685 (1990).
153. W. Huang and J. Hong, "A coupled-mode analysis of modulation instability in optical fibers," J. Lightwave Technol. **10**, 156–162 (1992).
154. M. Yu, C. J. Mckinstrie, and G. P. Agrawal, "Instability due to cross-phase modulation in the normal-dispersion regime," Phys. Rev. E **48**, 2178–2186 (1993).
155. D. Schadt and B. Jaskorzynska, "Generation of short pulses from CW light by influence of crossphase modulation (CPM) in optical fibres," Electron. Lett. **23**, 1090–1091 (1987).
156. A. S. Gouveia-Neto, M. E. Faldon, A. S. B. Sombra, P. G. J. Wigley, and J. R. Taylor, "Subpicosecond-pulse generation through cross-phase-modulation-induced modulational instability in optical fibers," Opt. Lett. **13**, 901–903 (1988).
157. W. Drexler, "Ultrahigh-resolution optical coherence tomography," J. Biomed. Opt. **9**, 47–74 (2004).
158. A. V. Husakou and J. Herrmann, "Supercontinuum generation of higher-order solitons by fission in photonic crystal fibers," Phys. Rev. Lett. **87**, 203901–203904 (2001).

159. M. A. Foster, J. M. Dudley, B. Kibler, Q. Cao, D. Lee, R. Trebino, and A. L. Gaeta, "Nonlinear pulse propagation and supercontinuum generation in photonic nanowires: experiment and simulation," Appl. Phys. B **81**, 363–367 (2005).
160. Y. S. Kivshar and B. A. Malomed, "Dynamics of solitons in nearly integrable systems," Rev. Mod. Phys. **61**, 763–916 (1989).
161. Y. Kodama and A. Hasegawa, "Nonlinear pulse propagation in a monomode dielectric guide," IEEE J. Quantum Electron. **23**, 510–524 (1987).
162. A. Demircan and U. Bandelow, "Analysis of the interplay between soliton fission and modulation instability in supercontinuum generation," Appl. Phys. B **86**, 31–39 (2007).
163. H. A. Haus, "Short pulse lasers," in *Compact Sources of Ultrashort Pulses*, I. N. Duling III, ed. (Cambridge U. Press, 1995).
164. E.-K. Tien, N. S. Yuksek, F. Qian, and Ö. Boyraz, "Pulse compression and modelocking by using TPA in silicon waveguides," Opt. Express **15**, 6500–6506 (2007).
165. R. Salem, M. A. Foster, A. C. Turner, D. F. Geraghty, M. Lipson, and A. L. Gaeta, "Signal regeneration using low-power four-wave mixing on silicon chip," Nat. Photonics **2**, 35–38 (2008).
166. M. Rochette, L. Fu, V. Ta'eed, D. J. Moss, and B. J. Eggleton, "2R optical regeneration: an all-optical solution for BER improvement," IEEE J. Sel. Top. Quantum Electron. **12**, 736–744 (2006).
167. H. Simos, A. Bogris, and D. Syvridis, "Investigation of a 2R all-optical regenerator based on four-wave mixing in a semiconductor optical amplifier," IEEE Photon. Technol. Lett. **22**, 595–597 (2004).
168. J. Suzuki, T. Tanemura, K. Taira, Y. Ozeki, and K. Kikuchi, "All-optical regenerator using wavelength shift induced by cross-phase modulation in highly nonlinear dispersion-shifted fiber," IEEE Photon. Technol. Lett. **17**, 423–425 (2005).
169. R. Salem, G. E. Tudury, T. U. Horton, G. M. Carter, and T. E. Murphy, "Polarization-insensitive optical clock recovery at 80 Gb/s using a silicon photodiode" IEEE Photon. Technol. Lett. **17**, 1968–1970 (2005).
170. D. A. B. Miller, "Rationale and challenges for optical interconnects to electronic chips," Proc. IEEE **88**, 728–749 (2000).
171. A. Shacham, K. Bergman, and L. P. Carloni, "On the design of a photonic network-on-chip," in *Proceedings of the IEEE International Symposium on Networks-on-Chip (NOCS '07)* (IEEE, 2007), paper 2.1.
172. B. G. Lee, X. G. Chen, A. Biberman, X. P. Liu, I. W. Hsieh, C. Y. Chou, J. I. Dadap, F. N. Xia, W. M. J. Green, L. Sekaric, Y. A. Vlasov, R. M. Osgood, and K. Bergman, "Ultrahigh-bandwidth silicon photonic nanowire waveguides for on-chip networks" IEEE Photon. Technol. Lett. **20**, 398–400 (2008).
173. Y. Okawachi, M. Foster, J. Sharping, A. Gaeta, Q. Xu, and M. Lipson, "All-optical slow-light on a photonic chip," Opt. Express **14**, 2317–2322 (2006).